

# A MOLECULAR SYNCHROTRON

CYNTHIA ELLEN HEINER

---

**A molecular synchrotron**

Cynthia E. Heiner

Thesis Radboud Universiteit Nijmegen - Illustrated

With references - With summary in Dutch and English

ISBN/EAN: 9789071382826

Subject headings: Synchrotrons / Molecular Beams / Cold Molecules /  
Electric Fields / Phase-space Dynamics

Front Cover: Illustration of the split-hexapole molecular synchrotron, along with a measurement showing a packet of ND<sub>3</sub> molecules completing 40 round trips in the synchrotron.

Back cover: The phase-space distribution, shown at eight different times, of an ensemble of ND<sub>3</sub> molecules passing through the Stark decelerator.

# A MOLECULAR SYNCHROTRON

EEN WETENSCHAPPELIJKE PROEVE OP HET GEBIED VAN  
DE NATUURWETENSCHAPPEN, WISKUNDE EN INFORMATICA

## PROEFSCHRIFT

TER VERKRIJGING VAN DE GRAAD VAN DOCTOR  
AAN DE RADBOUD UNIVERSITEIT NIJMEGEN  
OP GEZAG VAN DE RECTOR MAGNIFICUS  
PROF. MR. S.C.J.J. KORTMANN  
VOLGENS BESLUIT VAN HET COLLEGE VAN DECANEN  
IN HET OPENBAAR TE VERDEDIGEN  
OP DONDERDAG 22 JANUARI 2009  
OM 15.30 UUR PRECIES

DOOR

CYNTHIA ELLEN HEINER

GEBOREN OP 26 MEI 1980  
TE NEW YORK, VERENIGDE STATEN VAN AMERIKA

PROMOTOR : PROF. DR. G. J. M. MEIJER  
COPROMOTOR : DR. H. L. BETHLEM  
VRIJE UNIVERSITEIT, AMSTERDAM

MANUSCRIPTCOMMISSIE : PROF. DR. D. H. PARKER

PROF. T. P. SOFTLEY  
UNIVERSITY OF OXFORD, OXFORD

DR. S. Y. T. VAN DE MEERAKKER  
FRITZ-HABER-INSTITUT DER  
MAX-PLANCK-GESELLSCHAFT, BERLIN

*The work described in this thesis has been performed at the  
Fritz-Haber-Institut der Max-Planck-Gesellschaft in Berlin, Germany.*

# A MOLECULAR SYNCHROTRON

AN ACADEMIC ESSAY IN  
SCIENCE

## DOCTORAL THESIS

TO OBTAIN THE DEGREE OF DOCTOR  
FROM RADBOUD UNIVERSITY NIJMEGEN  
ON THE AUTHORITY OF THE RECTOR MAGNIFICUS  
PROF. DR. S.C.J.J. KORTMANN  
ACCORDING TO THE DECISION OF THE COUNCIL OF DEANS  
TO BE DEFENDED IN PUBLIC  
ON THURSDAY, 22 JANUARY 2009  
AT 15.30 HOURS

BY

CYNTHIA ELLEN HEINER

BORN ON 26 MAY 1980  
IN NEW YORK, UNITED STATES OF AMERICA

SUPERVISOR : PROF. DR. G. J. M. MEIJER  
CO-SUPERVISOR : DR. H. L. BETHLEM  
VRIJE UNIVERSITEIT, AMSTERDAM

MANUSCRIPT COMMITTEE : PROF. DR. D. H. PARKER

PROF. T. P. SOFTLEY  
UNIVERSITY OF OXFORD, OXFORD

DR. S. Y. T. VAN DE MEERAKKER  
FRITZ-HABER-INSTITUT DER  
MAX-PLANCK-GESELLSCHAFT, BERLIN

*The work described in this thesis has been performed at the  
Fritz-Haber-Institut der Max-Planck-Gesellschaft in Berlin, Germany.*



Figure 1: *The Fritz-Haber-Institut der Max-Planck-Gesellschaft, where the experiments in this thesis were conducted, is part of what used to be the Kaiser-Wilhelm-Institut für Physikalische Chemie und Elektrochemie. Here a photograph from 1913 showing the various institute buildings in Berlin-Dahlem. All of the buildings are still in use today; the small white building in the middle-right part of the photograph is the home of the Molecular Physics department.*





# Contents

<b>1</b>	<b>General introduction</b>	<b>1</b>
1.1	Motivation behind a molecular synchrotron . . . . .	2
1.1.1	Collision studies . . . . .	2
1.2	Outline of this thesis . . . . .	5
<b>2</b>	<b>History and Background</b>	<b>7</b>
2.1	Acceleration of charged particles . . . . .	8
2.1.1	Cyclotrons . . . . .	8
2.1.2	Phase stability in particle acceleration . . . . .	10
2.1.3	Synchrotrons . . . . .	12
2.1.4	Collision experiments using accelerated particle beams .	14
2.2	Manipulation of charged particles vs. neutral polar molecules .	15
2.2.1	Methods for manipulating charged particles with electric fields . . . . .	15
2.2.2	Matrix method . . . . .	18
2.2.3	Particle motion in a synchrotron . . . . .	20
2.2.4	Phase-space . . . . .	23
2.2.5	Methods for manipulating polar molecules with electric fields . . . . .	27
2.3	Properties of deuterated ammonia, ND <sub>3</sub> . . . . .	28
2.3.1	Focusing of ND <sub>3</sub> molecules using an electrostatic hexapole	31
<b>3</b>	<b>Molecular beams with a tunable velocity</b>	<b>35</b>
3.1	Introduction . . . . .	35
3.2	Manipulation of molecular motion . . . . .	36
3.2.1	Cooling in a supersonic expansion . . . . .	36
3.2.2	Stark deceleration of polar molecules . . . . .	39
3.2.3	Longitudinal bunching . . . . .	43
3.2.4	Transverse focusing . . . . .	47
3.3	Experimental setup . . . . .	47
3.4	Experimental results and discussion . . . . .	50
3.4.1	The beamline: Stark decelerator . . . . .	50

3.4.2	The beamline: focusing elements . . . . .	53
3.4.3	A versatile molecular beam . . . . .	57
3.5	Conclusions and outlook . . . . .	61
<b>4</b>	<b>Transverse stability in a sectional storage ring</b>	<b>63</b>
4.1	Introduction . . . . .	63
4.2	Principles of confining neutral molecules in a two-piece hexapole ring . . . . .	63
4.3	Experimental set-up . . . . .	69
4.4	Experimental results and discussion . . . . .	70
4.5	Conclusions and outlook . . . . .	74
<b>5</b>	<b>A synchrotron for neutral molecules</b>	<b>75</b>
5.1	Introduction . . . . .	75
5.2	Design of a two-piece synchrotron for neutral molecules . . . . .	76
5.2.1	Bunching neutral molecules in a synchrotron . . . . .	78
5.3	Experimental set-up . . . . .	83
5.4	Experimental results and discussion . . . . .	85
5.4.1	Bunching molecules in the synchrotron . . . . .	85
5.4.2	Characterizing the longitudinal potential well . . . . .	88
5.4.3	Phase-space matching . . . . .	93
5.4.4	Bunching two packets of molecules in the synchrotron . . . . .	95
5.5	Conclusions and outlook . . . . .	98
<b>6</b>	<b>Motional resonances in a molecular synchrotron</b>	<b>99</b>
6.1	Introduction . . . . .	99
6.2	Experimental set-up . . . . .	99
6.3	Transverse motion in a synchrotron . . . . .	100
6.3.1	Trajectory stability . . . . .	100
6.3.2	Betatron tune . . . . .	102
6.4	Experimental results and discussion . . . . .	103
6.4.1	Measurements in the synchrotron at various velocities . . . . .	103
6.4.2	The corrector . . . . .	105
6.4.3	Measurements in the synchrotron at various voltages . . . . .	107
6.4.4	Operating the synchrotron at a constant tune . . . . .	108
6.5	Conclusions and outlook . . . . .	110
<b>7</b>	<b>Outlook</b>	<b>111</b>
7.1	Introduction . . . . .	111
7.2	Design questions . . . . .	111
7.3	Current status . . . . .	117
7.4	Conclusion . . . . .	119
	<b>Bibliography</b>	<b>121</b>

<b>8 Samenvatting</b>	<b>129</b>
<b>9 Summary</b>	<b>131</b>
9.1 How does one control neutral molecules? . . . . .	134
9.2 A synchrotron for neutral molecules . . . . .	136
9.3 In my thesis . . . . .	138
<b>Acknowledgments</b>	<b>141</b>
<b>Curriculum Vitae</b>	<b>145</b>
<b>Publications</b>	<b>146</b>



# Chapter 1

## General introduction

Mankind has long been captivated by the perfection of a circle. This steadfast fascination has permeated itself into all facets of life be it art, mathematics, religion, or science. Viewing its symmetry either with awe or curiosity, the circle has become the object of ceaseless scrutiny for scholars and laymen alike, and it lies at the heart of this thesis. Here a ring is viewed as an arena for events to occur predictably and repeatedly, for example, the regular passing of one position at a well-defined time or the periodic application of a force. Particularly the projected benefits from the latter idea fuelled the development of circular accelerators or synchrotrons since the early 20<sup>th</sup> century, in which acceleration forces were applied to particles upon each revolution. Modern-day technology has produced synchrotrons that can accelerate particles to energies over one billion electronvolts (TeV). Pushing to higher energies allows physicists to study the minuscule world deep within atoms to the far-flung edges of the Universe. Likewise, pushing to lower energy limits in a synchrotron analogue would open a new territory for potential discoveries, and new energy frontiers lead to new and exciting breakthroughs in physics.

This thesis presents the demonstration of a synchrotron for neutral polar molecules. By exploiting the interaction of polar molecules with an electric field, molecules are first decelerated and subsequently injected into the synchrotron, which is a ring-shaped device consisting of two semi-circular electrostatic hexapole focusers. In the synchrotron, the molecules are confined in tight packets for storage times on the order of a second by adjusting the voltage configurations applied to the hexapole electrodes. The operation parameters, trapping properties, and velocity (energy) tunability of a molecular synchrotron are examined. A molecular synchrotron can be used for several different applications, the most promising of which is cold collision studies. The research described in this thesis heralds a step forward in approaching the goal of achieving a low-energy molecular physics experiment that is the ultimate replica of a high-energy nuclear physics experiment.

## 1.1 Motivation behind a molecular synchrotron

In its simplest form, a ring is a trap in which the particles - rather than having a minimum potential energy at a single location in space - have a minimum potential energy on a circle. Storage rings like these have been demonstrated for neutrons [1], atoms [2], and molecules [3]; in these rings, no forces are applied to the particles along the longitudinal direction and the stored particles are free to fill the ring. A synchrotron differs from a simple ring structure in that it provides a restoring ‘bunching’ force to allow for confinement in three dimensions. Schemes for synchrotrons for neutral molecules have been proposed by Nishimura et al. [4] and Cromptvoets et al. [5]. Nishimura et al. proposed a racetrack type lattice consisting of 20 separate elements for steering, focusing, and bunching the molecules. Cromptvoets et al. proposed a ring consisting of two bent hexapoles separated by a small gap. In this scheme, the fields necessary for steering, focusing, and bunching the molecules are created by changing the voltages applied to the hexapoles. The demonstration of such a molecular synchrotron is the topic of this thesis.

Molecular synchrotrons can, in principle, be used to perform all the experiments that are performed in traps for molecules. For instance, the increased interaction time is useful for lifetime measurements and precision tests of fundamental physics constants. The advantage of a synchrotron is its independent control over the ring segments. This allows for the optimization of segments for particular tasks. The capability to store multiple packets of molecules in the ring makes it possible to study molecules over extended times without making concessions to the repetition frequency at which the experiment runs, e.g., packets can be stored for seconds while injection and detection take place at a 10 Hz rate. Our main motivation for performing research into a molecular synchrotron is for studying cold collisions.

### 1.1.1 Collision studies

Traditionally, collisions have been studied using molecular beams. In these experiments, intense jets of molecules are propelled with a well-defined velocity towards either a stationary target or are made to collide with other particle beams in an interaction region. To improve resolution, beams are nowadays prepared in a (supersonic) gas expansion in which the final beam, extracted from the core, contains fast molecules moving in a near collision-free environment and concentrated to only a few internal quantum states. The velocity of the molecules is determined by the mass of the carrier (‘seed’) gas and by the temperature and pressure of the source [6], which is typically about 2000 m/s for He and 330 m/s for Xe. The translational and rotational temperatures of these beams are on the order of Kelvins, with vibrational temperatures being slightly higher, at tens of Kelvins.

Improved quantum state selection has been obtained by passing beams

through electrostatic hexapoles [7], among others [6]. Electrostatic hexapoles focus molecules in a specific quantum state while de-focusing molecules in all other quantum states. The combination of these pure beams with sophisticated laser-based detection methods allows for the performance of complete state-to-state resolved collisions studies. The orientation of the colliding molecules can be controlled by applying an electric field in the interaction region, thus providing information into the stereodynamics of collisions [8]. For instance, the differences of the collision cross-section between OH and various noble gases have been studied by preparing the OH with either the O-end or the H-end first [9].

The improved control over the internal motion of the molecules has left the forward velocity of the beam as the least well-defined parameter. Since the 1980's, crossed beam set-ups have been built where the crossing angle of the intersecting beams can be varied. This provides a way to sensitively vary the collision energy while maintaining molecular densities high enough for scattering (about  $10^{13}$  molecules/cm<sup>3</sup>), making it possible to measure threshold behavior of rotational energy transfer [10], [11], [12], and to tune the collision energy over the reaction barrier for reactive scattering [13], [14]. Volumes of invaluable knowledge into molecular collisions at relatively high energies, i.e. between 50-500 meV (200-5000 cm<sup>-1</sup>), have been obtained in this way. However, since the angle of the intersecting beams cannot be varied to arbitrarily small values, experiments in the interesting low-energy regime between 0-50 meV (0-200 cm<sup>-1</sup>) have remained largely elusive.

Unusual events can occur between colliding molecules in the low temperature regime – where the kinetic energy of the molecules is comparable to the rotational energy level splittings in the collision complex – that may result in a "new" molecular species or complex that would otherwise be impossible to form or observe. For instance, let us assume the situation where after two molecules collide they begin to rotate due to their translational energies being transferred, via the anisotropy of the potential energy surface, into rotational energy. This exchange may leave the molecules with insufficient translational energy to overcome the Van der Waals attraction, which effectively binds the molecules transiently together. These long lived excitations of the collision complex appear as sharp resonances in graphs of the cross section as a function of the collision energy. The position and width of these resonances provide an extremely sensitive probe of the interaction potential energy surfaces [15], [16], [17]. This type of resonance is ubiquitous in cold molecule-molecule collisions due to the manifold of internal molecular states that can lead to an equally large number of resonant states [15], [16], [17]. An interesting consequence of the low temperature regime is also that the collision energy becomes comparable to energy shifts due to external electric or magnetic fields. This provides a mechanism of external control over chemical reactions [18].

To measure low-energy collisions, molecules must first be cooled; note that laser cooling – so famously applied for cooling atoms to sub-Kelvin tempera-

tures – cannot be used for cooling molecules as the complexity of their energy level structure, with its multitudes of vibrational and rotational components, precludes a simple extension of laser cooling [19]. Cooling molecules can instead be achieved either by placing molecules in a cryostat [20], [21], or by decelerating molecules in an expanded beam using electric, magnetic, or optical fields [22]. Our group has concentrated its efforts on deceleration techniques for polar molecules using electric fields, which is accomplished in a so-called Stark decelerator. This approach takes advantage of an expansion’s internal cooling, and simply decelerates the already cold beam in the laboratory frame by exploiting the interaction of polar molecules with inhomogeneous electric fields in much the same way that a linear particle accelerator (LINAC) exploits the interaction of charged particles with magnetic and electric fields. As the deceleration process is quantum-state specific, the state purity of the bunches of slow molecules emerging from the decelerator is close to 100%. The velocity of the molecules can be tuned over a wide range and with a very narrow velocity distribution of typically 1-10 m/s. A pioneering crossed-beam scattering experiment has been recently performed using a Stark decelerated beam of OH molecules and a beam of Xe atoms [23]. In this experiment, the Xe beam had an average velocity of 300 m/s and the velocity of the OH radicals was varied from 33 to 700 m/s, resulting in a total center-of-mass collision energy of  $50 \text{ cm}^{-1}$  to  $400 \text{ cm}^{-1}$ , with an overall energy resolution of  $13 \text{ cm}^{-1}$ . The energy range covered in this study encompassed the energetic thresholds for inelastic scattering down to the lowest rotational levels of OH. The threshold behavior of the inelastic state-to-state cross-sections was accurately measured and was compared with the outcome of coupled-channels calculations on a computed OH-Xe potential energy surface [23].

In the above experiment, both the lowest attainable energy and the energy resolution were limited by the properties of the xenon beam. One can improve upon this by using two decelerated beams, however, obtaining the required densities in the scattering region poses a major obstacle. A way to increase the number of collisions that will take place is to load the decelerated beams into a molecular synchrotron. As opposed to the crossed beam geometry, in which the particles encounter each other only once, in a synchrotron the particles meet many times. For instance, in a ring containing 20 packets of molecules revolving in opposite directions, a packet having completed 100 round trips will have had 4,000 encounters. If losses due to, e.g., background gas are kept to a minimum, the total number of collisions that will take place will increase with the same factor. The molecules that undergo elastic or inelastic collisions will be ejected from the ring, resulting in a decrease of the number of stored molecules that scales with the number of round trips. The signal after some storage time with and without counter-propagating packets can be compared as a function of collisional energy\*. Also, changing the applied electric and/or magnetic

---

\*Note that the detection sensitivity is less for measuring a loss signal, as in the case of the



fields at the points of intersection, allows for the influence of external fields on the cross-section to be studied. Primary molecules to be investigated in this manner are  $\text{ND}_3$ ,  $\text{NH}_3$ ,  $\text{OH}$ , metastable  $\text{CO}(a^3\Pi)$ , and metastable  $\text{NH}(a^1\Delta)$ .

## 1.2 Outline of this thesis

In this thesis, the strength of merging molecular beam methods with those of accelerator physics to yield new manipulation tools and specifically a synchrotron for neutral molecules is described. Chapter 2 first gives the reader an overview of the advances made in charged particle physics in a time line ending with a brief summary of today's synchrotrons and large-scale colliders (Section 2.1), and then is followed by a discussion of the similarities and differences in techniques for manipulating ions or polar molecules (Section 2.2). Furthermore, a method to calculate trajectories of particles through a synchrotron is explained, as well as how to optimize particle transmission via the principles of phase-space matching. An excellent candidate to apply these methods to is deuterated ammonia,  $\text{ND}_3$ . In this thesis all the measurements are performed using  $\text{ND}_3$ , and some of the important properties of  $\text{ND}_3$  are discussed in Section 2.3.

The components of the injection beamline for the synchrotron, consisting of a Stark decelerator and several focusing elements, are detailed in Chapter 3. The description of the motion of the particles through the molecular beam machine is given in longitudinal position and momentum space. Using such a phase-space description further underlines the parallels between accelerator physics and Stark deceleration. Measurements will be presented on the deceleration, longitudinal spatial focusing and optimization, and velocity tuning of a beam of state-selected  $\text{ND}_3$  molecules.

Chapter 4 discusses the transverse focusing force exerted on  $\text{ND}_3$  molecules in a split-hexapole ring. The oscillation frequency and trap depth of the transverse well is investigated. The independent control over each segment of the hexapole ring allows for the injection of multiple packets of molecules.

Chapter 5 presents the principle behind longitudinal focusing, or "bunching", of a packet of  $\text{ND}_3$  molecules circulating in the synchrotron by using the fringe fields in the gaps in between the two half-rings. The various voltage configurations used to manipulate the molecules are given. Measurements are reported demonstrating the stability of molecules travelling at 87 m/s in the synchrotron. The stored bunch of cold molecules ( $T = 0.5$  mK) is confined to a 2.3 mm packet even after completing 100 round trips, corresponding to a flight distance of over 80 meters. The oscillation frequency and trap depth of

---

synchrotron, as opposed to a signal coming from the population of a new state. However, this can be (at least partly) compensated for by the fact that in a synchrotron elastic collisions contribute to the loss signal, and the elastic collision cross-sections are commonly larger than those for inelastic collisions.

the longitudinal well are measured. Additionally, the successful injection and bunching of multiple packets of molecules in the synchrotron is reported.

The stability of the synchrotron in the transverse directions is discussed in Chapter 6. Due to the introduction of the buncher into the synchrotron, motional instabilities or resonances, known as stopbands, arise at particular velocities. Thus molecules travelling at those speeds will be expelled out of the synchrotron. A simple model allows for the prediction of the position of the motional resonances, and is compared to measurements. The effect of the “correcter” configuration is investigated in efforts to minimize the width of the motional resonances. Moreover, it is demonstrated how the stopbands can be completely avoided by appropriately changing the voltages applied to the ring electrodes to allow for molecules over a wide velocity range to be stored.

Chapter 7 gives a short outlook for the next generation molecular synchrotron. The advantages of building a new 40-piece synchrotron are outlined.

## Chapter 2

# History and Background

With the discovery of the nucleus in 1911, Ernest Rutherford ushered in a new era of atomic physics at the turn of the century [24]. Rutherford conducted the first laboratory nuclear reaction in 1919 when he succeeded in splitting a nitrogen nucleus by subjecting it to a bombardment of natural  $\alpha$ -particles with energies of several MeV [25]. In these experiments the  $\alpha$ -particles were projected in all directions and with a limited amount of energy and intensity. This prompted Rutherford to express his “*ambition to have available for study a copious supply of atoms and electrons which have an individual energy far transcending that of the  $\alpha$  and  $\beta$ -particles from radioactive bodies*” in an address given to the Royal Society in 1927 [26]. This statement served to fuel the race of developing an experimental means for producing high speed particles in order to perform intimate nuclear collisions. A forerunner in this pursuit was Ernest O. Lawrence, and in 1932 he declared that “*it does seem safe to conclude at least that the most efficacious nuclear projectiles will prove to be swiftly moving ions*” [27]; from that point Lawrence devoted much of his career towards developing and improving methods for accelerating ions. Seventy-six years later, Lawrence’s pioneering work is still being fervently pursued and optimized in many large-scale laboratories and accelerator facilities the world over, where particles have been accelerated to TeV energies.

The first section of this chapter intends to give the reader an overview of the history and progression of particle accelerators from cyclotron to synchrotron to large scale colliders, as well as to provide some necessary details into the operation of these three types of accelerators. The second section of this chapter will address how techniques employed for particle acceleration have been adapted for use with neutral molecules. Additionally, a few important concepts that remain the same regardless if applied to a molecular synchrotron or to its behemoth brethren for charged particles, e.g., particle motion and phase-space matching, will be discussed. In the third section, the properties of ND<sub>3</sub> – the prime candidate for deceleration and storage in a molecular synchrotron as de-

scribed in this thesis – and the effects that  $\text{ND}_3$  experiences in the presence of electric fields will be given.

## 2.1 Acceleration of charged particles

### 2.1.1 Cyclotrons

Around 1920, an idea for an electro-static charged particle accelerator using high voltages was conceived by Cockcroft and Walton. They envisioned accelerating protons over a single DC potential-drop of some hundreds of kV [28], and succeeded in performing the first nuclear reaction produced by an accelerator in 1932 [29], [30], [31]. However, already in 1925 the Swede G. Ising put forth the idea of obtaining higher energies by accelerating particles not just over a single potential-drop stage with a DC voltage, but rather over many successive stages with pulsed voltages [32]. A multi-stage accelerator based on this idea was constructed by the Norwegian Rolf Wideröe. He imposed the condition that while the particles moved in the field free regions (inside shielded electrodes) between the stages (gaps) the phase of the alternating voltage changed by  $180^\circ$ . These time-varying radio-frequency (rf) pulses resulted in the particle gaining energy as it passed each gap; this is considered the first linear accelerator. As a young professor at the University of California Berkeley in 1929, Ernest O. Lawrence came across Wideröe's article reporting on a three-stage accelerator for sodium ions [33], and wondered if, instead of building many acceleration stages in a line, it wouldn't be easier to use just one acceleration stage that could be re-used by circulating positive ions back through it with the help of a magnetic field. With this novel thought, the cyclotron was born [34].

A sketch of a basic cyclotron is drawn in Figure 2.1; a top-view is presented on the right-hand side. Two electrodes, semi-circular hollow D-shaped plates, are placed inside a vacuum chamber in between two magnets. The magnetic field is perpendicular to the electrodes. High rf-electric oscillations are applied to the plates so that an oscillating electric field is created in the diametral region between them. Ions are formed in the middle of the plates via a low-voltage gaseous discharge within a small metallic cavity set normal to the plates (not shown in the drawing). The ions are pulled out through a small hole by the oscillating electric field. If a negative voltage is applied to electrode A while electrode B is kept at ground, the ensuing electric field will accelerate positive ions in the gap towards electrode A. Inside the hollow electrode the ion is forced along a circular path by the magnetic field, and emerges again at the gap between the electrodes; this is marked in the right-hand side as path  $a\dots b$ . The centrifugal force, which is balanced by the force an ion experiences moving normal to a magnetic field,  $B$ , can be as expressed as [27], [36]

$$Bqv = \frac{mv^2}{r}, \quad (2.1)$$

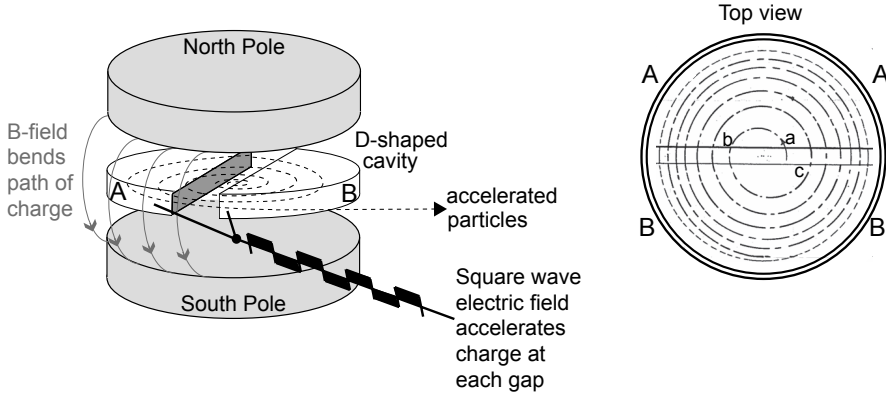


Figure 2.1: Schematic of the principle components of a cyclotron; the top view is shown on the right-hand side. The electrodes are placed inside a magnetic field. As the ions fly through the hollow electrodes the magnetic field forces them to follow a curved path. An oscillating radio-frequency pulse provides an acceleration force for the revolving ions as they move through the gap between the two D-shaped electrodes. After each acceleration stage, the now faster ion travels along a path with a larger radius until it reaches the periphery of the electrodes and can be coupled out. Adapted from Lawrence et al. [27] and [35].

where  $q$  is the charge,  $v$  is the forward velocity,  $m$  is the mass, and  $r$  is the radius of the circular path; this equation is now known as the cyclotron equation. For the condition of resonance, the magnetic field is adjusted so that the time required for an ion to complete one half-circle is equal to the half period of the electric oscillations, i.e., the cyclotron frequency,  $\Omega$ , must be equal to  $2\pi f$ , where  $f$  is the frequency of the applied field. Keeping the field oscillating under these parameters assures that the electric field will have reversed by the time the ion enters electrode B. So as the ion traverses the gap it receives a second acceleration, and passes into the interior of electrode B with a higher velocity. Again while inside electrode B it will travel along a circular path ( $b\dots c$ ), but due to the ion's higher velocity, it moves along a path with a larger radius. The time required for an ion to move along a semi-circular path is independent of its velocity, since this is proportional to the radius of the path, according to [27]

$$t = \frac{\pi r}{v} = \frac{\pi m}{Bq}. \quad (2.2)$$

Therefore, if the ion is in resonance with the electric field after moving along the first half-circle, it will remain so over the successive paths. The ion is accelerated each time it crosses a gap, travelling in ever-widening circles until it reaches the periphery of the electrodes. The final ion energy is the sum of the individual accelerations, or can be computed from the radius of the last semi-

circular path in the magnetic field [36]. Note that, when using negative ions, the process is the same except that the ions revolve in the opposite direction, if the polarity of the electrodes is kept the same.

The first cyclotron, a design with a diameter of a mere 4.5 inches ( $\sim 12$  cm) and mostly constructed by Lawrence's student at the time, M. S. Livingston, succeeded in January 1931 in accelerating hydrogen ions up to 80,000 eV with a potential of only 1.8 kV [37]. Transverse focusing of the ions was provided by the curvature of the magnetic field towards the periphery edges. The realization of the cyclotron was only made possible, as is so often the case in science, due to advances in supporting technology, in particular novel high-vacuum technology and seals, and rf-oscillators. A second cyclotron started working that same summer, an 11-inch ( $\sim 28$  cm) ring – similar in dimensions to the ring presented in this thesis – using a potential difference of 4 kV to accelerate protons to over a million electron-volts [27]. In one year's time, a third cyclotron was operating at more than twice the size, 27 inches ( $\sim 69$  cm), and with an 80-ton magnet\* it accelerated protons up to 3.6 MeV [38]. The last in this cyclotron series was a 60-inch ( $\sim 153$  cm) cyclotron completed in 1939 [40], which became the standard model for cyclotrons at the time, producing 16 MeV deuterons.

### 2.1.2 Phase stability in particle acceleration

Exceeding an upper limit of the proton energy of around 10 MeV was a serious problem for the early cyclotrons [41]. Below this threshold, protons revolve in phase with the electric field oscillation. However, near this limit, the relativistic increase of the proton's mass at such high velocities begins to slow down the proton's rotation frequency, as can be seen from Equation 2.2. Thus the proton arrives at the gap at increasingly later times and becomes out of phase with the oscillating (accelerating) electric field; eventually the phase slip is to the point that the proton is no longer accelerated. Essentially, synchronization was necessary between the cyclotron frequency and the rf-frequency. This obstacle was overcome by the idea of *phase stability*, discovered independently by Edwin McMillan [42] in the US and Vladimir Veksler [43] in Russia in 1944/45.

McMillan and Veksler proposed introducing slow variations to the oscillation frequency of the accelerating electric field or to the magnetic field – or to both – to achieve stable particle orbits. The particles, despite moving at relativistic velocities, could then cross the gap many more times in phase with the accelerating field and thus achieve a higher total acceleration, and in principle, limitless acceleration. They suggested switching the accelerating rf-fields not at the crest of the rf-amplitude but rather on the decreasing side of the waveform, to guarantee the stable locking of the particles at a certain phase. In other words, phase stability assures isochronous operation of a cyclotron for extreme-relativistic cases. Varying the frequency of the (accelerating) electric

---

\*A funny historical note is that Lawrence purchased this magnet as war surplus; it was originally built to power a transatlantic radio link in World War I [39].

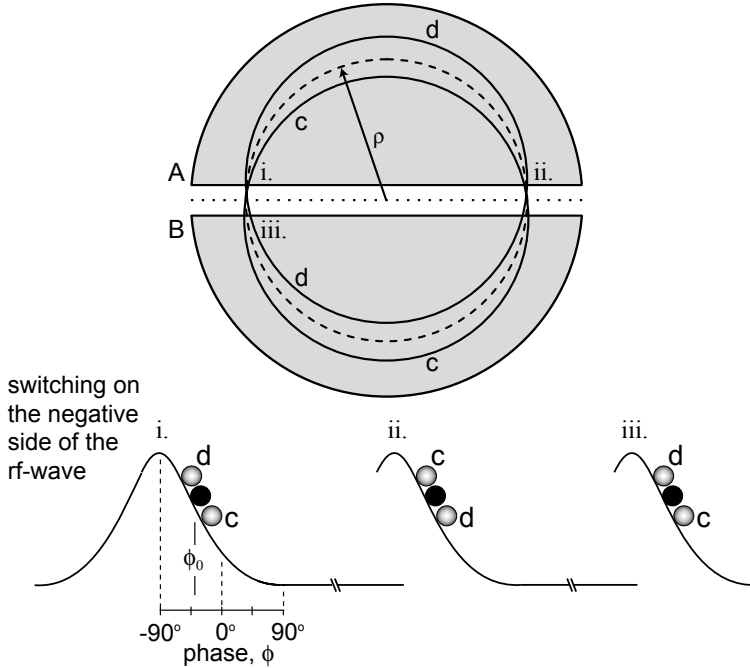


Figure 2.2: Schematic depicting the principle of phase stability in a synchrocyclotron. Switching the accelerating electric fields in between the two D cavities on the negative side of the wave form, instead of at the crest, stably locks the particles within a certain phase range into oscillations around a certain orbit (upper part) and its corresponding phase,  $\phi_0$  (lower part).

field according to the velocity of the particles leads to a *synchrocyclotron* (or rf-frequency modulation (FM)-cyclotron). Varying the magnetic field strength according to the velocity of the particles leads to a *synchrotron*.

Figure 2.2 shows a top-view sketch of a basic synchrocyclotron with two D-shaped plates. The rf-frequency is chosen such that a particle moving on the central orbit located at a radius  $\rho$  (dashed line) will always arrive at the gap at a certain constant rf-phase. This particle is marked in black in the lower part of the Figure; it has a phase-angle of  $\phi_0$ . At position (i), particle c has less than the normal energy, and so will be bent along a path with a smaller radius than that of  $\rho$ . This means that particle c will take less time to complete its half-orbit. Particle c thus arrives earlier at the next period (ii) – or at a different (increased) phase  $\phi$  – and therefore is exposed to a higher accelerating field during the decreasing edge of the rf-amplitude; this difference in the phase is sketched in (ii) in the bottom of the Figure. Particle c therefore receives a larger energy increase. Conversely, if a particle d has more than the normal

energy, it must move along a path with a larger radius than  $\rho$ . Subsequently, particle  $d$  takes more time to complete its orbit, arriving later at the next gap, and thus receives less acceleration. Between (ii) and (iii) the situation reverses itself. These particles will continue to execute “phase oscillations” around a stable phase-angle  $\phi_0$  indefinitely.

The concept of phase stability revolutionized the techniques of particle acceleration. Lawrence again took a leading role and together with McMillan had already applied the principle of phase stability to a 37-inch ( $\sim 94$  cm) model FM-cyclotron by the summer of 1946 [44]. The success of this model led to the construction of a 184-inch ( $\sim 467$  cm) synchrocyclotron capable of delivering alpha particle beams with 400 MeV of energy [45]. This machine, commissioned in 1948, supported an impressive series of discoveries, including the creation of the first man-made pi-meson [46]. Not only were protons accelerated in both classical cyclotrons and synchrocyclotrons, but also heavy ions such as deuterons and alpha-particles. Many cyclotrons and synchrocyclotrons were built across the globe in the 1950’s. The largest synchrocyclotron still in use today has iron poles 6 meters in diameter and is located in Russia. The weight of the entire accelerator is near 10,000 tons – a weight comparable to that of the Eiffel Tower [39]. It is capable of accelerating protons to energies of 1 GeV. However, the size and costs of a magnet large enough to accelerate particles in a synchrocyclotron to energies above 1 GeV were simply too great to justify further construction.

### 2.1.3 Synchrotrons

It soon became clear that the way forward to accelerate particles above 1 GeV was to use a synchrotron, which accelerates the particles along one track by varying the magnetic fields. This approach eliminates the need for a massive magnet and instead requires merely a line of magnets, which can be ramped up in field strength, fixed along one circumference to bend the particles. The weight of the necessary magnets in a synchrotron is an order of magnitude less than that needed in the synchrocyclotron. The particles must be pre-accelerated for a synchrotron, which is usually performed in a linear array of rf-cavities, to the minimum energy needed to remain along the track\*. To ensure a constant orbit after injection and acceleration, the magnetic fields are increased such as to match the energy gain of the particles in each revolution. Although proposals for such a machine had already been made by McMillan and (independently) Veksler in 1945, and Bohm and Foldy in 1946 [48], the first experimental proof of the synchrotron<sup>†</sup> was not delivered until 1946 at the

---

\*Oliphant proposed a “cyclosynchrotron” in which particles would be pre-accelerated in a synchrocyclotron until a pre-defined orbit,  $O$ , at which point a synchrotron with bending magnets along one track of tunable field strength would take over the acceleration of the particles [47].



Malvern Research Laboratory in the UK [49].

The first synchrotrons were classified as 'weak-focusing' types. In these synchrotrons, the focusing forces are coupled, i.e., transverse fields de-focus in one plane as they focus in the other (perpendicular) plane. In these synchrotrons, a vertical focusing force was achieved by sloping the magnetic fields so that the vertical field strength was larger for smaller radii and smaller for larger radii. The negative field gradient de-focuses horizontally and must not be so strong as to cancel the path curvature (focusing) effect. This arrangement resulted in a weak focusing of particles that was adequate for circular machines in which the dimensions of the magnet gap were appreciable in size to the radius of the orbit. The first synchrotron of this type was the Cosmotron at Brookhaven National Laboratory in the United States [50] where protons were accelerated in ca. 1 second to 3 GeV; the total weight of the magnets was 2000 tons. The strength of the magnetic fields is limited by the saturation of the iron components that shape the field, meaning that in order to accelerate to higher energies synchrotrons needed to be constructed with larger circumferences. This implies costly, large-bore magnets. The biggest and last-remaining weak-focusing synchrotron, the Dubna synchrotron, is located at the Petersburg Nuclear Physics Institute in Russia and has a radius of 28 meters and a total weight of magnetic iron of 36,000 tons accelerating particles to 10 GeV; Dubna is rarely used and is seen as a memorial to this epoch [39]. Increasing the energy beyond this point by building an even larger weak-focusing synchrotron was determined to be practically very difficult and too expensive to realistically pursue.

In 1952 Courant, Livingston, and Snyder published the principle of *alternating-gradient* focusing for synchrotrons that would reduce the size of the particle beam and thus reduce the size (that is the amount of iron) of the focusing magnets [51]. The principle is based on the fact that successive applications of focusing and de-focusing forces results in a strong net focusing (or collimation) in both transverse directions for the particle beam – such magnetic (and electric) focusing is analogous to the net focusing effect one achieves in optics when a focusing lens is followed by a de-focusing lens (of equal focal lengths). In fact, regardless of the order in which the lenses are placed, an overall focusing effect will always be produced. In the Cosmotron, all the magnets were C-shaped, with the open side and the magnetic field gradient facing outward. The alternating-gradient scheme was put into practice by changing the orientation of these magnets, so that some of their field gradients faced outward and some inward. For example, a magnet with an axial field component that decreased with increasing radius would be followed by a magnet with an axial field component that increased with increasing radius, i.e., a magnet de-focusing the beam vertically is then followed by a magnet focusing the beam vertically, creating a strong-focusing stable lattice where the displacement of the trajectory

---

<sup>†</sup>This synchrotron accelerated electrons rather than protons, and achieved an energy of 8 MeV [49].

does not scale with the energy of the machine. The first alternating-gradient synchrotron (AGS) was constructed at Cornell University in 1954 to accelerate electrons to 1.5 GeV in a mere 4 cm beam pipe and using only 16 tons of magnets. For accelerating protons, two almost identical AG-synchrotrons were built, one at the Brookhaven National Laboratory in the United States and one at the European laboratory known as CERN\* in Switzerland providing protons of 33 GeV and 28 GeV<sup>†</sup>, respectively. Without strong focusing, a comparable machine as powerful as the AGS – using typical apertures of only a few centimeters – would have needed apertures as large as ca. 50 by 150 cm, and therefore embarrassingly large magnets.

### 2.1.4 Collision experiments using accelerated particle beams

Major technological hurdles had to be overcome to achieve the present state where synchrotrons can produce pencil-thin beams of particles with over 100,000 times the energy of the most energetic natural radioactive emission. Following in Rutherford's footsteps, at first accelerated beams were made to smash into stationary targets in order to learn about matter and energy dynamics in collisions. However, in an experiment involving one accelerated particle beam and one stationary target, most of the available (projectile) energy will go into target recoil, leaving only a small fraction of energy to fuel the collision. It was reasoned that if two particles of equal energy travelling in opposite directions could be made to collide, the available energy would be twice the whole energy of one particle as measured in the center-of-mass system as no energy is lost to recoil action [52]. Needless to say, this is a much more effective use of energy in a collision experiment. Exactly 40 years after the demonstration of Lawrence's 4.5 inch cyclotron, the 300 m proton-proton collider, the Intersecting Storage Rings (ISR), became operational at CERN. As was the case in Lawrence's lab, CERN continued to build larger models; the next construction project was the 7 km (circumference) giant rings of the Super Proton Synchrotron (SPS), in which many different kinds of particles can be accelerated up to 450 GeV. It was in this machine that, in 1983, protons and antiprotons were smashed together head-on to form new W and Z particles; this discovery would lead to a Nobel prize in 1984 for Simon van der Meer and Carlo Rubbia [53]. CERN is still on the cutting edge of particle physics: its new 27 km (circumference) Large Hadron Collider (LHC) just started operation in September 2008 and promises an arena (100 m underground) for two counter-propagating beams of particles called 'hadrons' - either protons or lead ions - to be accelerated and smashed together in a head-on collision. This will approximately recreate the

---

\*The laboratory name stems from the French Conseil Européen pour la Recherche Nucléaire, which translates into English as European Council for Nuclear Research.

<sup>†</sup>The original proposal for a proton synchrotron at CERN was for a 5 GeV weak-focusing accelerator, however for the same cost the 28 GeV strong-focusing synchrotron was instead constructed; this synchrotron is still in use today.

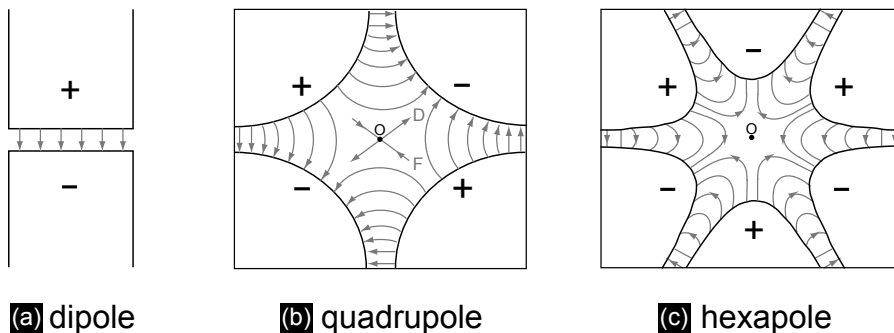


Figure 2.3: *The three field arrangements commonly used in beam transport: (a) a dipole field, (b) a quadrupole field, and (c) a hexapole field.*

conditions immediately after the Big Bang [54].

## 2.2 Manipulation of charged particles vs. neutral polar molecules

This section introduces the basic components needed for any circular accelerator. The tools for charged particles will be presented in Section 2.2.1. The effect that the individual components have on the motion of a particle that passes through them can be described by a matrix, thus allowing the whole ring to be evaluated by matrix multiplication (Section 2.2.2). There are many important concepts used in charged particle acceleration that remain exactly the same for neutral molecule acceleration (deceleration) and are worthy of some explanation here: the particle motion (Section 2.2.3), and the concept of phase-space to describe beam dynamics and good phase-space matching to reduce beam losses (Section 2.2.4). In Section 2.2.5, the idea of applying accelerator techniques to control the motion of neutral molecules – adapted from concepts used to control charged particles – is introduced.

### 2.2.1 Methods for manipulating charged particles with electric fields

In this section, I will evaluate the various building blocks for charged particle acceleration. Charged particle accelerators employ both magnetic and electric fields to manipulate the motion of the particles. I will discuss here electric fields, as these are relevant for the manipulation of polar molecules as described in this thesis; however the description for magnetic focusing is analogous.

Not any electric field you have in mind can be made. The electric field

must be derived from a potential,  $\Phi$ , where  $\vec{E} = -\vec{\nabla}\Phi$ . In a region devoid of charges, the divergence of  $\vec{E}$  must be zero, which means that the electrostatic potential then fulfills Laplace's equation,  $\nabla^2\Phi = 0$ . The solutions to Laplace's equation, which are finite at the origin, can be written in an expansion series as:

$$\Phi(x, y) = \Phi_0 + \Phi_1 \frac{x}{r_0} + \Phi_2 \frac{(x^2 - y^2)}{r_0^2} + \Phi_3 \frac{(x^3 - 3y^2x)}{r_0^3} \dots, \quad (2.3)$$

where  $r_0$  is a characteristic length scale [55]. Here the first term is a constant voltage, the second term is the potential associated with a constant electric field, the third term is a quadrupolar electric field, and the fourth term is a hexapolar electric field. This is often referred to as a multipole expansion.

To produce these fields, one needs to choose electrodes with specific geometries. A dipole field is shown in Figure 2.3(a). This geometry is typically used in accelerator physics to bend charged particles, as a charged particle moving between these two poles will be deflected in a single direction. A quadrupole field is shown in Figure 2.3(b). In this case, the field components have a linear dependence on the displacement from the origin (O). This means that a particle farther from the origin experiences a larger linear force – this is similar to a lens in optics. By squaring and adding the field components, it is clear that the field is constant on a circle centered around the origin. The quadrupole can be rotated over  $90^\circ$  to exchange the focusing (F) and defocusing (D) axes. Such a quadrupole doublet, or a pair of quadrupole lenses rotated  $90^\circ$  with respect to each other, is typically used in accelerator physics as the simplest way to achieve a convergent action in both transverse planes. For example, a positive ion moving through the field as sketched in the Figure would experience a convergent focusing force along the F-direction and a divergent de-focusing force along the orthogonal D-direction. This ion could then be re-focused along the D-direction by making it pass through a second focuser turned by  $90^\circ$ . The motion in the focussing plane can be approximated by a simple harmonic oscillator. A hexapole\* field is shown in Figure 2.3(c). Similarly as in the case of the quadrupole, the field magnitude is constant around a circle centered at the origin. The field in a hexapole, however, is proportional to the square of the radius. The hexapole configuration is typically used in accelerator physics to correct for non-linearities and higher order effects, such as chromatic aberration, and design defects and misalignments.

The basic components needed for any accelerator are a source, an injection beamline for pre-acceleration, electrostatic lenses and/or magnets for bending (dipole) and focusing (quadrupole and multipole) the beam, and a (rf-) accelerator or (de-) bunching cavity, as depicted in Figure 2.4. These fundamental elements are combined into particular sequences, or lattices, which are then repeated many times; the Figure shows a synchrotron with two repeating seg-

---

\*In charged particle physics the term 'sextupole' is more frequently used, however since it is commonplace to refer to a hexapole in molecular physics, I will use this notation here.

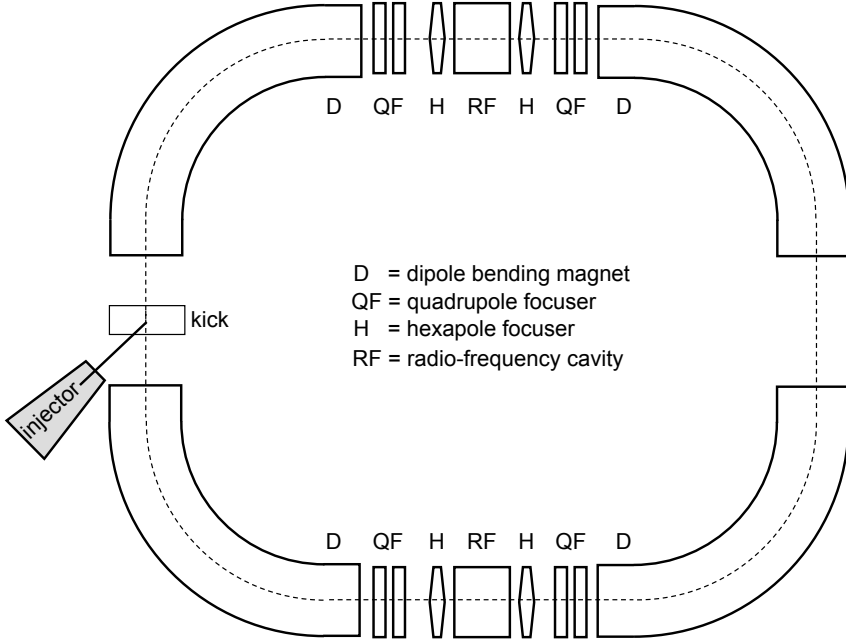


Figure 2.4: An example of a synchrotron lattice including bending dipole ( $D$ ) lenses (or magnets), quadrupole focusing ( $QF$ ) lenses, hexapole ( $H$ ) correction lenses, and an accelerating or bunching radio-frequency ( $RF$ ) cavity.

ments. Any lattice for which a periodic solution exists may be used as repetitive segment. Using repeating segments in constructing an accelerator is helpful in simplifying the design and for determining the beam dynamics. One then needs to only solve the equations of motion for one lattice and extrapolate to determine the position and velocity of the beam at any time in the accelerator.

In Figure 2.4, the beam is prepared with a certain velocity in the injector and then matched with optics into the ring via a kick magnet. The particles bend under the force of the electric (magnetic) fields in a dipole configuration ( $D$ ), which is also set along a curved path. As is often the case, the synchrotron in the Figure has some straight sections and drift sections interposed between the beam elements. In the straight sections, the particles pass through a quadrupole doublet ( $QF$ ), focussing the particles in both transverse directions, and a hexapole ( $H$ ) to correct the particles' trajectories after any disturbances. The particles in a beam during free flight between all the elements will spread out due to the small energy spread, i.e., the higher energy particles will drift ahead while the lower energy particles will lag behind. This can be corrected for in the rf-resonant cavity, where the ratio between the beam's en-

energy spread and the beam's position spread can be adjusted through a process termed *bunching* (or *debunching*). The action of the buncher is to decelerate the early arrivals and accelerate the late arrivals. In this way, particles receive a change in kinetic energy (involving a change in velocity) proportional to the time difference between their arrival and that of a particle with the average energy; the phasing of the buncher is set so as to impose no absolute change in energy. Note that either the energy spread of the beam is reduced at the expense of its position (time) spread or the reverse occurs where the particles are tightly bunched in space at some position downstream at the expense of the energy spread. The longitudinal focusing effect of a buncher is analogous to the transverse focusing effect(s) of an electrostatic lens. A bunching rf-cavity might also be located at the end of the injection transport line, where it is advantageous to shape the energy spread in order to improve transmission of particles into the synchrotron. The 'empty' drift spaces shown in the Figure are often included in a synchrotron's construction for the possibility of incorporating extra equipment, such as control systems or beam position monitors.

### 2.2.2 Matrix method

The trajectory of a particle can be determined by tracing its position and angular divergence at any time. This means that the displacement and divergence of a particle leaving an element are given in terms of the corresponding input conditions by linear simultaneous equations, in which the coefficients depend on the nature and the length of the element. It is convenient to express these linear transformations as matrices. Such matrices are known as *transformation matrices*, because they transform the coordinates of a particle in phase-space from one point in the beamline to another. The transformation matrix of the entire system can then be found by multiplying the transformation matrices of the individual elements; such a description is known as the *matrix method*. I will use this method to determine the transformation matrix of the beamline used in the experiments in Chapter 3. Here I merely aim at giving the reader a background understanding of the method, introducing the equations of motion from which the matrices are formed, and presenting a basic example with a few convenient terms.

Let us first consider the movement of a beam through a field-free drift space of length  $l_1$ . Provided that the angular divergence is small, one can use the paraxial approximation to determine the output position  $x_2$  and the output angular divergence  $x'_2$  of a particle that has travelled a distance  $l_1$ ; this can be written in terms of its input position  $x_1$  and input divergence  $x'_1$  by the equations [41], [56]

$$\begin{aligned} x_2 &= x_1 + l_1 x'_1 \\ x'_2 &= x'_1 \end{aligned} \tag{2.4}$$

This translational movement corresponds to a linear free flight in real space.

Since no forces are acting on  $x'_1$ , it remains constant. In matrix form\*, equations 2.4 become

$$\begin{bmatrix} x_2 \\ x'_2 \end{bmatrix} = \begin{bmatrix} 1 & l_1 \\ 0 & 1 \end{bmatrix} \begin{bmatrix} x_1 \\ x'_1 \end{bmatrix}. \quad (2.5)$$

It is necessary to also consider the transformation of particles moving through focusing elements, as this is critical for tracking the movement of the molecules in both the beamline (see Chapter 3) and in the synchrotron (see Chapter 5). The focusing elements in a beamline or synchrotron, e.g., quadrupoles and hexapoles, impose an instantaneous change to the particle's angular divergence, which is proportional to the position of their trajectory at the point of passing through the electrostatic lens. We describe the focusing elements using the thin lens approximation and assuming a perfectly harmonic force. The relations between particle displacement and divergence at input and output are then [41], [56]

$$\begin{aligned} x_2 &= x_1 \\ x'_2 &= x_1/f + x'_1 \end{aligned} \quad (2.6)$$

bearing in mind that  $f$  is negative for a focusing (convergent) lens. In matrix form, equations 2.6 become

$$\begin{bmatrix} x_2 \\ x'_2 \end{bmatrix} = \begin{bmatrix} 1 & 0 \\ \frac{1}{f} & 1 \end{bmatrix} \begin{bmatrix} x_1 \\ x'_1 \end{bmatrix}. \quad (2.7)$$

To illustrate a simple matrix multiplication, let us consider the elementary problem of optical imaging [56]. A particle packet at a distance  $s_1$  from a converging lens with a focal length of  $-f$  achieves its real image at a distance  $s_2$ . The displacement and divergence at the object and at the image are connected by the matrix equation

$$\begin{bmatrix} x_2 \\ x'_2 \end{bmatrix} = \begin{bmatrix} 1 & s_2 \\ 0 & 1 \end{bmatrix} \begin{bmatrix} 1 & 0 \\ -\frac{1}{f} & 1 \end{bmatrix} \begin{bmatrix} 1 & s_1 \\ 0 & 1 \end{bmatrix} \begin{bmatrix} x_1 \\ x'_1 \end{bmatrix}. \quad (2.8)$$

It is important to note the order of the matrices and that the multiplication actually works 'backwards', that is from right to left of Equation 2.8. All rays resulting from particles leaving from any point within the packet, despite their initial divergence, will be brought to a common point in the image at the focal position downstream (also see Figure 2.14). This implies that  $x_2$  depends on  $x_1$  but not on  $x'_1$ . This leads to the well-known thin lens equation

$$\frac{1}{s_1} + \frac{1}{s_2} = \frac{1}{f} \quad (2.9)$$

---

\*Note that the determinant of the transfer matrix is one, and that since a drift length must be symmetric, the diagonal elements must be equal.

The combination of these three matrices: a drift length, a thin lens, and another drift length, are often substituted in for the thick lens action of a focusing element such as a quadrupole or hexapole. In this case, a “drift length” is considered to start at the entry face and end at the exit face of an electrostatic lens; all edge effects of the field are neglected for our purposes.

### 2.2.3 Particle motion in a synchrotron

Particles revolving in a synchrotron make various oscillations leading to four distinct frequencies, which are illustrated in Figure 2.5. In part (a) two oscillations are depicted: the *cyclotron* and the *synchrotron* oscillations. Essentially the particles are trapped in a travelling potential well that revolves around the ring at a frequency associated with the time to complete a round trip, that is, the (trap) cyclotron frequency. Within this travelling well, the particles oscillate in the longitudinal direction around a perfect particle – at phase  $\phi_0$  – due to the applied (restoring) harmonic forces. The depth of the longitudinal well depends on the strength of the focusing forces and is inversely proportional to the distance between longitudinal focusing elements (e.g., buncher rf-cavities).

For a circular accelerator, there is by design an ideal reference orbit which closes in on itself at a particular radial position; this is marked in black in the figure and is referred to as the *closed orbit*. Particles flying with the same forward velocity but with a different radial position or with a non-zero radial velocity will oscillate around this closed orbit, which is marked in gray in parts (b) and (c) of Figure 2.5. These oscillations are referred to as *betatron* oscillations and occur in both transverse directions. The horizontal oscillations are sketched in (b), while the vertical oscillations are sketched in (c); note that the frequencies are arbitrarily drawn. The number of betatron oscillations that a particle makes per round trip is known as the *tune*,  $\nu$  (or sometimes  $Q$ ). There is no reason for the horizontal and vertical oscillations to be the same. Moreover, although in theory the different oscillatory motions should be independent, the horizontal betatron motion is coupled to the synchrotron motion due to the conservation of angular momentum. Details on the coupling effects in a dipole ring for neutral molecules were described by Crompvoets et al. [5].

Due to the periodic design of the synchrotron, if a particle’s trajectory is perturbed once from passing a deformation – such as a field imperfection or a physical misalignment – then it will continue to be perturbed every time it passes that deformation. If these perturbations act on a particle in synchronism with its oscillatory motion, they can lead to beam instabilities known as *motional resonances*. Such resonances caused by field imperfections are also called structural or lattice resonances\*. Linear resonances arise from linear im-

---

\*In a linear accelerator, particles of different momenta follow the same ideal trajectory, making transverse particle excursions negligible. While such a resonance situation is conceivable in a very long beam transport line composed of many periodic sections, the appearance of motional resonances is generally restricted to circular accelerators.



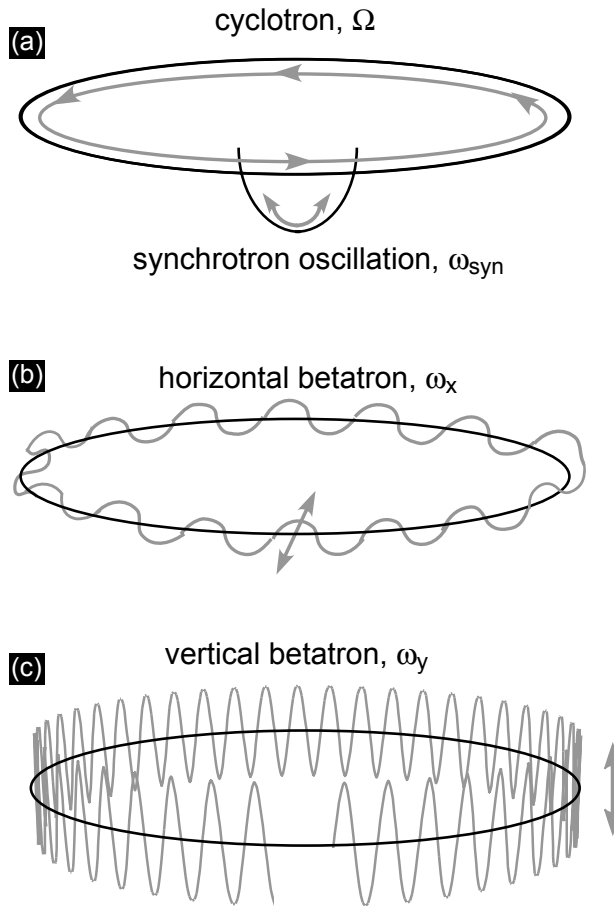


Figure 2.5: An example of various oscillatory motions of particles confined in a synchrotron. The closed orbit is marked in black and exemplary oscillations are marked in gray; the direction of the motion is denoted by the arrows. The frequencies are sketched arbitrarily.

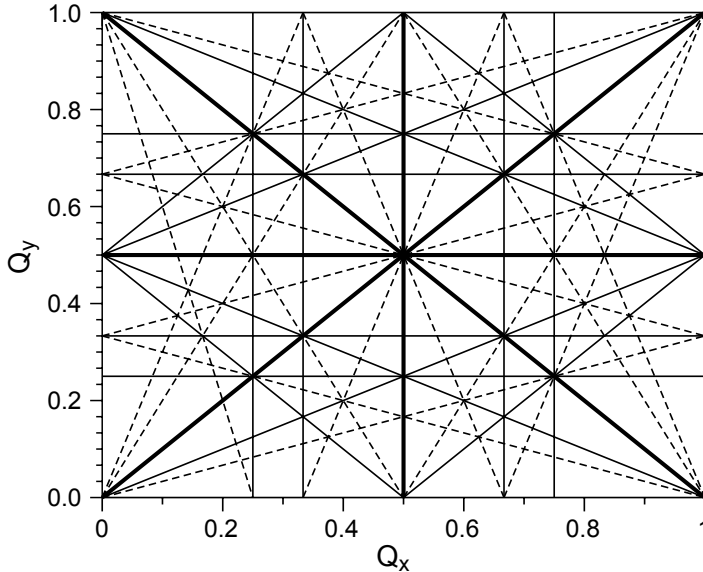


Figure 2.6: Resonance diagram up to the fourth order to help establish stable operation tunes for a synchrotron. The dark lines mark linear resonance lines, where  $m_x\nu_x + n_y\nu_y = l$  with  $|m_x| \leq 1$  and  $|n_y| \leq 1$  and  $l$  is an integer. The thin solid lines and dashed lines mark resonance lines up to the fourth order, where  $m_x\nu_x + n_y\nu_y = l$  with  $|m_x| \leq 4$  and  $|n_y| \leq 4$ . Note that  $|m| + |n|$  is the order of the resonance. The symbol  $Q_x$  and  $Q_y$  are the fractional parts of betatron tunes  $\nu_x$  and  $\nu_y$ , respectively. Adapted from [41].

perfections or *dipole errors*. Essentially the angular ‘kick’ to the particle’s orbit experienced in every turn adds up coherently because the kicks are always in the same direction. Eventually the orbit becomes too large and the particles are lost from the ring; thus in this case, a closed orbit cannot exist. This situation occurs when the betatron tunes are integers or half-integers. Hence, to avoid this amplification effect due to linear imperfections, synchrotrons are designed to avoid  $\nu_x = m$  or  $\nu_y = n$ , where  $2m, 2n$  are integers. Similarly, the betatron tunes should avoid linear coupling resonances due to skewed quadrupoles (quadrupole errors) at  $\nu_x \pm \nu_y = l$ , where  $l$  is an integer. Furthermore, although implementing hexapoles and higher multipoles is beneficial to beam stability and focusing, these same elements drive higher order resonances [41].

Figure 2.6 shows the betatron resonances up to the fourth order in what is known as a resonance diagram. The dark solid lines denote the linear resonances arising from dipole errors, the thin solid lines denote the resonances arising from quadrupole errors, and the dashed lines denote the resonances arising from hexapoles. It is clear that the available resonance-free tune space

becomes small. Synchrotrons are designed to operate at tune values well away from these resonances, or *stopbands*. Note that the resonance lines possess some “thickness” (not shown in the Figure) which is referred to as the stopband width. The stopband width is dependent on the strength of the resonance, which tends to decrease with increasing order. A particle beam rarely can survive an integer or half-integer resonance, however it often can withstand all other resonances. In fact, it is beneficial to increase the periodicity or symmetry  $N$  in a synchrotron as this serves to reduce the density of resonance lines by the factor  $N$ , which in turn proportionally increases the stable area between resonances for operating the ring. Clearly, stopband correction is crucial for attaining beam stability; Chapter 6 of this thesis presents experimental observations of stopbands and how to avoid them in a molecular synchrotron.

### 2.2.4 Phase-space

A particle’s position and velocity can be represented by the position of a point in six-dimensional space with coordinates  $(x, p_x, y, p_y, z, p_z)$ ; this 6D space is known as *phase-space*. A particle’s movement over time can be traced by its change in phase-space coordinates, which is connected with the motion of the particle in real or ‘configuration’ space. A beam is represented by a group of points in phase-space, one for each particle in the beam, and for a beam of finite dimensions the representative points will lie within a 6D hypervolume in phase-space.

This hypervolume is subject to Liouville’s theorem, which states that: *Under the action of forces which can be derived from a Hamiltonian, the motion of a group of particles is such that the local density of the representative points in the appropriate phase-space remains everywhere constant.* [56] This brief statement requires some additional details. Liouville’s theorem refers to ‘forces which can be derived from a Hamiltonian’; by this he refers to any system of conservative forces acting on a beam. A conservative force is a force whose exertion on a moving particle is determined solely by the particle’s initial and final position and not on its intermediate path. For example, a conservative force arises from magnetic and electric fields, whereas energy changes due to radiation or collisions with targets may not be conservative; in the latter case Liouville’s theorem does not hold. One can deduce two important properties of phase-space from Liouville’s theorem. First that different trajectories in phase-space will not intersect at any given time, since within a Hamiltonian system the motion is uniquely determined by the initial conditions and time. So if two particles’ trajectories were to cross at a certain point, they would then continue from that point on along identical paths. Note that it is assumed that no interaction occurs between individual particles in the beam, e.g., their mutual electrostatic repulsion and space charge effects are neglected. This is important since one wishes to determine the trajectory of an individual particle over time as a function of its specific individual position and momentum

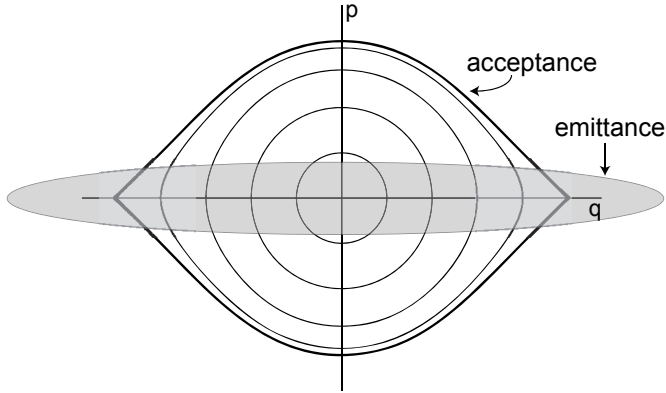


Figure 2.7: A sketch showing the relation between the phase-space emittance of a beam and the phase-space acceptance of a section. Adapted from [57].

coordinates in phase-space, and this should not depend on the phase-space coordinates of all the other particles around it. The second important property is that a boundary  $B_1$  that confines a group of particles at time  $t_1$  will transform into a boundary  $B_2$  at time  $t_2$  that confines the same group of particles. Thus, the motion of a group of particles can be determined by following the phase-space movement of the group's boundary. Taking these points into account, describing the motion of a group of particles using the phase-space representation is analogous to describing an incompressible fluid: the shape of the six-dimensional volume can change but the volume itself cannot.

### Principles of phase-space matching

It is important in accelerator physics to transport a large amount of particles and keep them densely together. Since the electric field forces do not increase the phase-space density, it is critical to start with, and then to maintain, a packet of particles with a high phase-space density. This is also the case here, as experiments presented in this thesis try to retain the largest amount of molecules, with the highest possible density – and in our case the lowest possible temperature (smallest velocity spread) – along the beamline and throughout the synchrotron. The initial phase-space volume filled by the particles at the exit of a section is known as the *emittance* of that section. Likewise, the phase-space volume that a piece of equipment has available for the particles is known as the *acceptance* of that section; the emittance (gray shaded) and the acceptance (black contour lines) are depicted in Figure 2.7. The exact size of the acceptance depends on the parameters of the device and the forces to which the particles are exposed. The contour marking the maximum acceptance

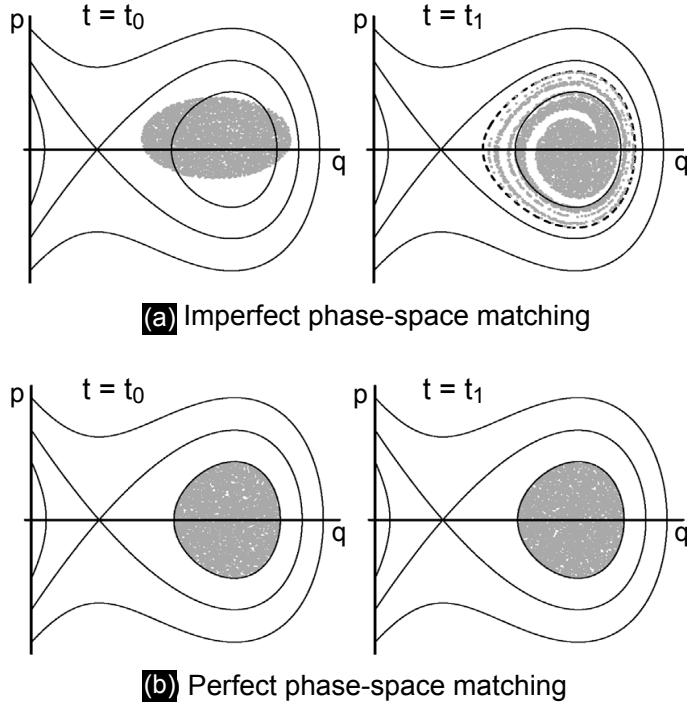


Figure 2.8: A sketch showing the phase-space matching of the emittance on to the acceptance of a **(a)** imperfect and **(b)** perfect potential well. Adapted from Cromptoets et al. (with permission) [5].

(bold black line) is also known as the *separatrix* – it ‘separates’ or marks the boundary in phase-space between two distinct areas: the oscillating motion of the stably confined particles within the separatrix and the unconfined motion outside of the separatrix. The idea of a piece of equipment possessing an acceptance in phase-space is analogous to a physical aperture, that is, the imposed limitations on beam dimensions and divergences from an equipment’s acceptance are equivalent to the limitations from physical obstacles actually preventing the passage of unwanted particles. If the emittance is larger than the acceptance, as is the case in Figure 2.7, then any particles located outside the separatrix will be lost. All the particles inside the seperatrix will begin to oscillate, or in phase-space trace ellipses, along the contour lines.

In Figure 2.8**(a)** a similar sketch as in Figure 2.7 of an elliptical emittance is shown being coupled into a non-linear potential well at time  $t = t_0$ , but with a smaller emittance than acceptance, i.e., no particles are lost in transmission. However, it is immediately clear from the Figure that the emittance and the acceptance do not match in either shape or position. The particles reside (and

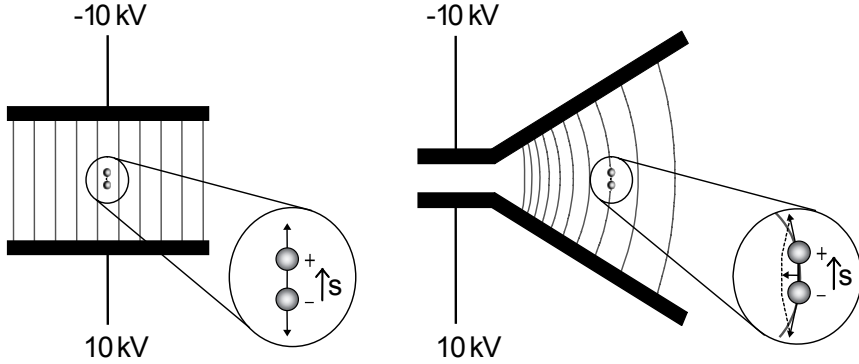


Figure 2.9: A polar molecule in a homogeneous and an inhomogeneous electric field. The net force on the left-hand molecule is zero, whereas the net force on the right-hand molecule is pointing towards higher field regions. Adapted from Bethlem *et al.* (with permission) [58].

oscillate) in the potential well (revolving in phase-space) during time  $t = t_0$  until  $t = t_1$ . Due to the phase-space mismatch and the non-linearities of the potential well, the cloud of particles thins and somewhat fragments. This leads to an increase in the *effective* area in phase-space that the particles occupy. That is to say that the envelope that encompasses the same number of (trapped) particles becomes larger in phase-space; this is marked by the dashed contour line in Figure 2.8. Compared to the original phase-space volume at  $t = t_0$ , the effective phase-space volume at  $t = t_1$  is almost double. Note that, of course, the phase-space density does not change, however the *effective* phase-space density is lower since the same number of particles remain confined in the (larger) effective phase-space volume.

With the use of transformation sections (e.g., hexapoles) to best match the shape of the emittance on to the shape of the acceptance – a process known as *phase-space matching* – and reducing field non-linearities (i.e., creating perfect fields), one can avoid, or at least minimize, any decrease in the effective phase-space density. This is illustrated in Figure 2.8(b), where a perfect match of the emittance and the acceptance is sketched. Immediately evident is that the phase-space volume packet remains constant. The packet looks the same from time  $t = t_0$  to  $t = t_1$ , i.e., no filamentation occurs. During the time that the particles reside in the potential until  $t = t_1$ , their effective phase-space density remains constant.

### 2.2.5 Methods for manipulating polar molecules with electric fields

Let us now turn our attention to how electric fields can be used to manipulate the motion of polar molecules. Let us look at a polar molecule that is located in a homogeneous electric field, as depicted on the left-hand side in Figure 2.9. Naturally the positive charge distribution is attracted towards the negative pole, and vice-versa, the negative charge distribution is attracted towards the positive pole. These forces have the same magnitude but are in opposite directions, thus the sum is zero, i.e., a polar molecule experiences no net force in an area of a homogeneous electric field.

Let us now look at a polar molecule that is located in an inhomogeneous electric field, as depicted on the right-hand side in Figure 2.9. Again the positive charge distribution is attracted towards the negative pole, and the negative charge distribution is attracted towards the positive pole. However, these attractive forces now follow along curved lines. Thus the sum of these two forces does not cancel, but rather a small component of the force remains.

In the Figure, the dipole of the molecule is orientated parallel to the electric field, and in this case the molecule experiences a force towards the high field region. If the molecule's orientation were turned around, then the molecule would experience a force towards the low field region. The force the molecule experiences can be written as

$$\vec{F} = \mu_{\text{eff}} \vec{\nabla} |\vec{E}|, \quad (2.10)$$

where  $\vec{\nabla} |\vec{E}|$  is the gradient of the electric field strength and where  $\mu_{\text{eff}}$  is the effective dipole moment given by  $\mu_{\text{eff}} = \mu \cos \theta$ . As  $\mu_{\text{eff}}$  is an inherent property of the quantum state, the force is quantum state dependent. When  $\mu_{\text{eff}}$  is positive, the molecules experience a force towards the high field region, and molecules in these states are referred to as *high-field-seeking* (hfs) molecules. Conversely, when  $\mu_{\text{eff}}$  is negative, the molecules experience a force towards the low field region, and molecules in these states are referred to as *low-field-seeking* (lfs) molecules.

Note that by simply replacing  $\mu_{\text{eff}}$  in Equation 2.10 with the charge  $q$  and the gradient of the electric field with the electric field, i.e., with the gradient of the potential  $V$ , we arrive at Coulomb's law to describe the force on a charged particle in a homogeneous electric field:

$$\vec{F} = -q \vec{\nabla} V. \quad (2.11)$$

Thus it becomes apparent that tools for manipulating ions can be easily implemented for use with molecules, despite the fact that the force a polar molecule experiences in an inhomogeneous field is typically some eight to ten orders of magnitude weaker than the force an ion experiences in an electric field.

An interesting consequence of Equation 2.10 is that polar molecules can be simultaneously focused in two dimensions. This implies that polar molecules

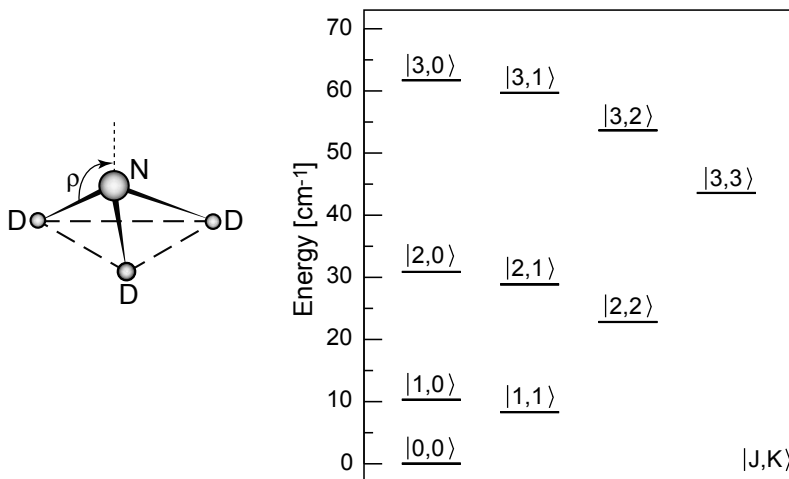


Figure 2.10: The deuterated ammonia molecule,  $\text{ND}_3$ , and its rotational energy level scheme up to the  $|J, K\rangle = |3, 3\rangle$  state.

can be confined with a static electric-field. For instance, it is possible to create a minimum of the absolute electric field in space. This trapping concept is in stark contrast to charged particles, which in accordance to Earnshaw's theorem, cannot be confined with static fields [59].

### 2.3 Properties of deuterated ammonia, $\text{ND}_3$

Ideal candidate molecules for manipulation using electric fields are those having a large dipole moment-to-mass ratio and a first-order Stark effect – a more linear Stark effect leads to fewer nonlinearities. Both of these criteria are fulfilled by deuterated ammonia: its  $\mu$  is 1.5 Debye while its mass is 20 amu, and its Stark effect is rather linear (see below). Since all the experiments in this thesis employ  $\text{ND}_3$ , some properties of the molecule will be given here. A list of additional prospective molecules well suited for manipulation using electric fields can be found elsewhere [60].

Ammonia is a pyramid-shaped symmetric-top molecule consisting of one nitrogen and either three hydrogen ( $\text{NH}_3$ ) or three deuterium atoms, as sketched in the left-hand side of Figure 2.10. The angle formed by the N-D bond with respect to the vertical plane is known as the umbrella angle,  $\rho$ . As a symmetric top molecule, two of the three principal moments of inertia are equal to each other, so only two (rotational) quantum numbers are needed to describe  $\text{ND}_3$ :



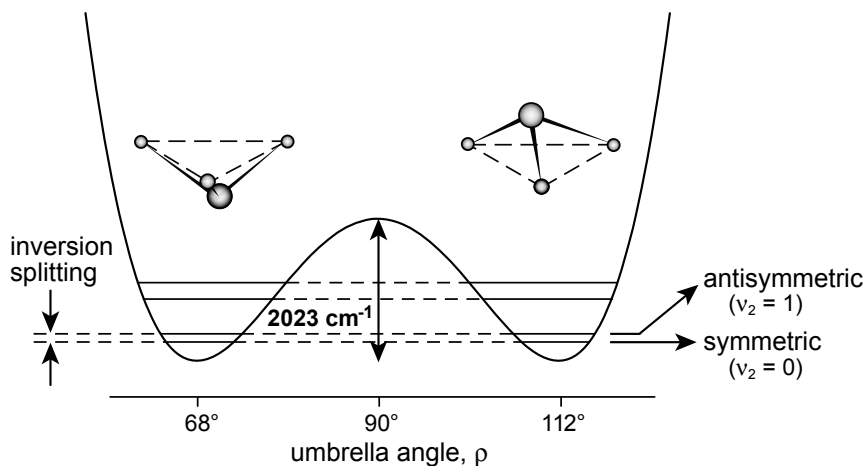


Figure 2.11: The potential energy of ND<sub>3</sub> as a function of umbrella angle,  $\rho$ . The inversion splitting of the  $|J, K\rangle = |1, 1\rangle$  level is  $0.053 \text{ cm}^{-1}$  for ND<sub>3</sub>, whereas it is  $0.79 \text{ cm}^{-1}$  for NH<sub>3</sub>.

the total angular momentum,  $J$ , and the projection of the angular momentum on the symmetry axis,  $K$ . ND<sub>3</sub> is an oblate (saucer or disc shaped) molecule meaning that  $I_a = I_b < I_c$ , where  $I$  is the moment of inertia around axes  $a$ ,  $b$ , and  $c$ . Under a rigid rotor assumption the rotational energy can be expressed (in  $\text{cm}^{-1}$ ) as [61]

$$E_r = BJ(J + 1) + (C - B)K^2, \quad (2.12)$$

where  $B$  and  $C$  are rotational constants defined by  $B = h/8\pi^2cI_B$  and  $C = h/8\pi^2cI_C$ . On the right-hand side of Figure 2.10, the lowest rotational energy levels for ND<sub>3</sub>, from the ground state  $|J, K\rangle = |0, 0\rangle$  up to the  $|J, K\rangle = |3, 3\rangle$  state\*, are shown using the rotational constants reported by Fusina et al. [62]. For an oblate symmetric top molecule, the rotational energies decrease with increasing  $K$  for a given value of  $J$ .

In Figure 2.11, the potential energy of the molecule is plotted as a function of umbrella angle. It is lowest near  $\rho = 68^\circ$  or  $\rho = 112^\circ$ . These values correspond to equivalent positions of the nitrogen atom at either the pyramid's apex or at the inverted apex position on the other side of the deuterium plane. The atoms can change between these two positions through a tunnelling process, since the potential energy barrier between the two energy minima is only  $2023 \text{ cm}^{-1}$ . This in turn leads to the splitting of all rovibrational levels below the barrier energy, as marked in the Figure, into symmetric ( $\nu_2 = 0$ ) and antisymmetric ( $\nu_2 = 1$ ) levels. The energy difference between these ensuing levels is known as the inversion splitting,  $W_{\text{inv}}$ . The inversion splitting in the  $|J, K\rangle = |1, 1\rangle$

\*On this scale, the inversion splittings of the levels cannot be seen.

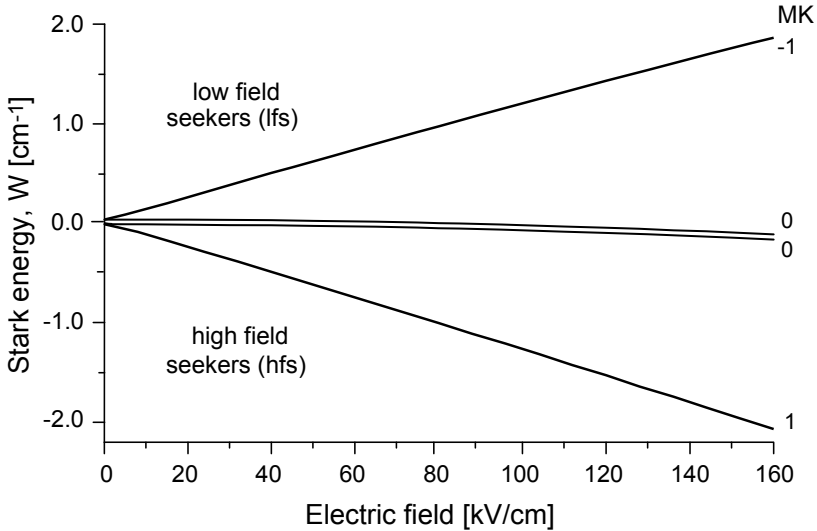


Figure 2.12: Stark effect of a  $\text{ND}_3$  molecule as a function of electric field strength. At field strengths of 100 kV/cm (typical conditions used in the experiments in this thesis), the Stark shift for the low-field seeking  $|1, -1\rangle$  state is  $1.2 \text{ cm}^{-1}$ .

level in  $\text{NH}_3$  and  $\text{ND}_3$  is  $0.79 \text{ cm}^{-1}$  [63] and  $0.053 \text{ cm}^{-1}$  [64], respectively. The larger mass of the D-atoms suppresses the tunnelling, which serves to lower the  $W_{\text{inv}}$  in  $\text{ND}_3$  as compared to  $\text{NH}_3$ . A smaller inversion splitting leads to a stronger mixing of the inversion doublet components at a given electric field strength, and therefore to a more linear Stark-effect.

Upon applying an electric field, the symmetric and antisymmetric components of the  $J = 1, K = 1$  state repel each other. This leads to four levels as illustrated in Figure 2.12. For low fields the interaction between the different  $J$  levels can be neglected and the Stark energies of the level in an electric field is approximately given by

$$\Delta W_{\text{Stark}} = \pm \sqrt{\left(\frac{W_{\text{inv}}}{2}\right)^2 + \left(\mu |\vec{E}| \frac{MK}{J(J+1)}\right)^2}, \quad (2.13)$$

where the plus and minus signs denote the low-field- and high-field-seeking states, respectively. The magnitude of the inversion splitting determines the linearity of the Stark effect. The  $\text{ND}_3$  molecule has a more linear Stark effect in electric fields between 5 and 100 kV/cm – which is the range used in the present experiments. At higher electric fields the different  $J$  levels begin to mix; for  $\text{ND}_3$  this is only a small effect as is seen in Figure 2.12.

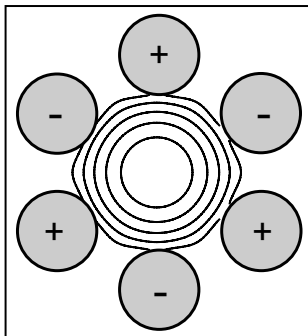


Figure 2.13: A hexapole focuser. Applying alternating voltages to the six electrodes placed around a circle creates an electric-field configuration where the center of the hexapole is at a zero-field and the electric field magnitude increases in the radial direction. In this configuration, lfs molecules will be transversely focused towards the center.

### 2.3.1 Focusing of ND<sub>3</sub> molecules using an electrostatic hexapole

As an example of how polar molecules can be manipulated with electric fields, I will address the focusing properties of an electrostatic hexapole on ND<sub>3</sub>. Figure 2.13 shows a hexapole focuser consisting of six rods\* placed equidistantly around a circle. The electrodes are held alternately at negative and positive voltages, although a negative or positive voltage against ground is also often used, to produce a voltage difference  $V$  between adjacent rods. The electric field was calculated using a finite element program [67]. The field lines in Figure 2.13 are observed to be slightly perturbed near the electrodes, skewed in a somewhat hexagonal shape [5]. Close to the center, the electric field is radially symmetric. The field points radially outwards following:

$$\vec{E}(r) = \frac{3V}{2R_{\text{hex}}^3} r^2 \hat{\mathbf{r}}, \quad (2.14)$$

where  $R_{\text{hex}}$  is the inner radius of the hexapole (or multipole) and  $r$  is the radial distance from the axis of the hexapole. Thus, molecules in the lfs state will

---

\*An ideal hexapole field is formed from six hyperbolic surfaces. However, such electrodes would nearly touch at large radii (see Figure 2.3c), greatly increasing the chance of electrical discharges ('sparks') between the electrodes when set to high voltages. Thus, it is standard practice to construct a hexapole focuser out of cylindrical electrodes. In the set-up used for the experiments presented in this thesis, the hexapoles were fashioned following the geometric suggestions of Reuss [65], where the rods have a radius of  $0.5 \cdot R_{\text{hex}}$  with  $R_{\text{hex}}$  defined as the inner radius of the hexapole. A different geometry has been proposed by Anderson [66] in which the electrodes are constructed with a rod radius of  $0.565 \cdot R_{\text{hex}}$ . In this case, the electric field lines are more circular, better approximating an ideal field.

experience a force towards the beam axis. Assuming for the moment that the inversion splitting in ND<sub>3</sub> is zero, the force is simply written as

$$\vec{F} = -kr \hat{\mathbf{r}}, \quad (2.15)$$

where  $k$  is the harmonic force constant given by

$$k = \mu \frac{3V}{R_{\text{hex}}^3} \frac{|MK|}{J(J+1)}. \quad (2.16)$$

Such a perfect harmonic motion has an angular frequency of

$$\omega = \sqrt{\frac{k}{m}}, \quad (2.17)$$

where  $m$  is the mass of the molecule.

The harmonic force of a hexapole is perturbed by the zero-field inversion splitting in ND<sub>3</sub>. The nonlinear effects must be included in order to calculate the true force exerted by the hexapole on a ND<sub>3</sub> molecule. Inserting Equation 2.14 into Equation 2.13 and subsequently applying Equation 2.10, we calculate

$$\vec{F} = -\vec{\nabla} \left[ \pm \sqrt{\left(\frac{W_{\text{inv}}}{2}\right)^2 + \left(\frac{1}{2}kr^2\right)^2} \right] \quad (2.18)$$

$$= \mp \frac{k^2 r^3 \hat{\mathbf{r}}}{\sqrt{W_{\text{inv}}^2 + k^2 r^4}} \quad (2.19)$$

$$= \mp \frac{kr \hat{\mathbf{r}}}{\sqrt{1 + \left(\frac{W_{\text{inv}}}{kr^2}\right)^2}}, \quad (2.20)$$

with the upper and lower signs denoting the low-field- and high-field-seeking states, respectively. If the magnitude of the inversion splitting would be zero, this is equal to Equation 2.15.

Figure 2.14 shows trajectories for molecules passing through a hexapole (orientated along the z-axis) while either **(a)** neglecting or **(b)** including effects from inversion splitting. The molecules are assumed to originate from the same single point. The hexapole is switched on when the molecules are at position A, and is switched off when the molecules are at position B. The molecules are completely inside the hexapole when the field is applied, so edge effects are neglected. After passing through the hexapole, the molecules continue in free flight. For the ideal case with a perfectly linear Stark effect, the molecules all moving with the same velocity starting at one point are focused back into a single point. If the inversion splitting is taken into account, one observes that in low electric fields – i.e., near the hexapole axis – the force on the molecules is reduced, thus the molecules moving close to the axis are focused less efficiently.

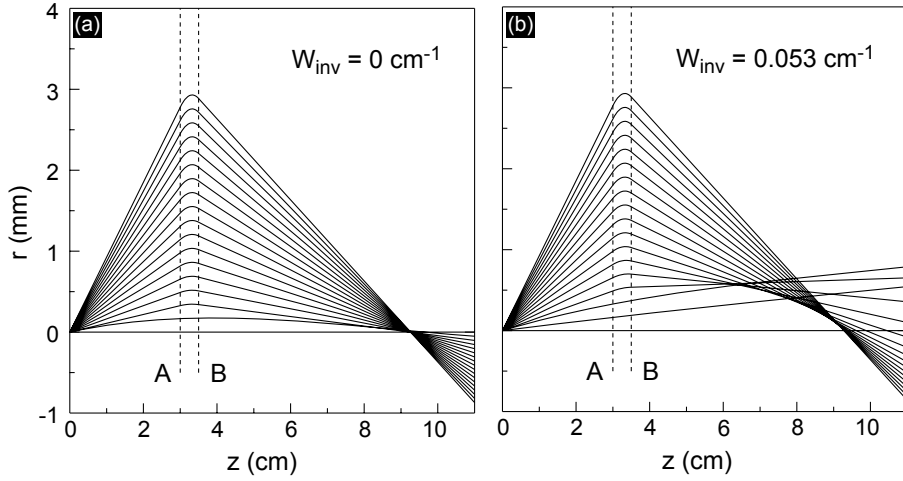


Figure 2.14: Example of the trajectories of ND<sub>3</sub> molecules passing through a hexapole focuser, either (a) neglecting or (b) including the non-linear effects of inversion splitting. In the ideal case (a), all molecules starting at one point, after experiencing a harmonic force, will be focused to the same position in space some free-flight distance away. Including the  $W_{\text{inv}}$  of ND<sub>3</sub> (b) results in a less efficient focussing force on molecules which are moving close to the hexapole axis than those which are farther off-axis. This anharmonic force leads to a blurring in the focus downstream. Adapted from Cromptoets et al. (with permission) [5].

This anharmonic force leads to a blurring in the focus downstream: the sharp point-like focus changes into a ring-shaped focus that is cylindrically symmetric around the hexapole axis [68]. This effect is similar in optics to the spherical aberration caused by lenses that leads to caustics, and in accelerator physics to the chromatic aberrations caused by quadrupoles.



## Chapter 3

# Molecular beams with a tunable velocity

### 3.1 Introduction

*“Born in leaks, the original sin of vacuum technology, molecular beams are collimated wisps of molecules traversing the chambered void that is their theatre like companies of players framed by some proscenium arch. On stage for only milliseconds between their entrances and exits, they have captivated an ever growing audience by the variety and range of their repertoire.”* This is how John Fenn affectionately summarized the properties of molecular beams in 1987, in his foreword to volume 1 of the by now classic book on “Atomic and Molecular Beam Methods” [69].

This chapter deals with yet another variety in the ‘repertoire’ of the molecular beams, namely the production of beams of polar molecules with a tunable velocity. These beams offer the possibility to extend the time that the ‘players are on stage’ from milliseconds to seconds. In this chapter, I will discuss the strength of merging molecular beam methods with those of accelerator physics, with an emphasis on phase-stability. With so many comparisons to large accelerator facilities, one may suspect that Stark decelerator experiments are extremely large, complicated, and demanding. On the contrary, the Stark-deceleration molecular beam machine that is described here is compact, simple, and easy to implement. The whole beamline is only about 70 cm long, and can be operated with a mere four high voltage switches and two high voltage power supplies for full control over the molecules. Additionally, this beam machine is optimal for use as an injection beamline for a molecular synchrotron.

The different parts of the beamline are discussed individually; it consists of

---

Adapted from:  
C. E. Heiner, H. L. Bethlem, and G. Meijer, *Phys. Chem. Chem. Phys.* **8**, 2666 (2006).

a pulsed source, a Stark-decelerator, and longitudinal and transverse focusing elements. The description of the motion of the particles through the molecular beam machine is given in longitudinal position and momentum space. The use of such a phase-space description is common practice in accelerator physics and it is most insightful here to discuss the dynamics of a molecular beamline in these terms. Measurements will be presented on the deceleration, longitudinal and transverse spatial focusing and optimization, and velocity tuning of a beam of state-selected ND<sub>3</sub> molecules.

## 3.2 Manipulation of molecular motion

### 3.2.1 Cooling in a supersonic expansion

Molecular beams are indeed born out of a controlled leak, i.e., by letting a gas expand from a container through a small hole into vacuum [70], [71]. Let us consider a gas reservoir with a high pressure of ca. 2 atm and a hole through which the molecules can escape into vacuum, as depicted in Figure 3.1. Inside the container, the molecules of the “hot”, i.e., room temperature, static gas possess a randomness in both their velocity direction and magnitude; each arrow in Figure 3.1 represents the direction and magnitude of the velocity of one molecule. In the lower graph, the velocity distribution of the gas in the reservoir is shown.

As the gas escapes into vacuum, the enthalpy associated with the random thermal motion is converted into kinetic energy (directed flow) after the hole – ideally *all* the random enthalpy that the molecules have in the container would be converted to kinetic flow energy in the expansion region, thus rendering a zero translational temperature in the moving frame of the beam [70]. As the gas adiabatically expands, the enthalpy reduces and the gas cools, whilst the velocity increases to conserve energy. In reality, the temperature in the beam is limited by both finite collision cross sections and condensation. Although the latter is a slow effect – a minimum of a three-body collision is needed to form a nucleus around which a cluster could materialize, whereas cooling requires only a two-body collision – condensation will still ultimately occur. One can lower the temperature at which condensation occurs by seeding a small amount of the gas of interest with a large amount of noble gas. Due to the weak interatomic forces between noble gas atoms, they cluster only at low temperatures, and therefore serve as a heat sink during the expansion. The terminal velocity of the beam is determined by the carrier gas, and it is usually faster than the local speed of sound, ergo the expansion is said to be supersonic. Molecules seeded in Xe, for instance, move at a terminal velocity of about 330 m/s in a room temperature expansion. When these beams are operated in a pulsed mode, pumping requirements are less severe and mm-sized orifices can be implemented.



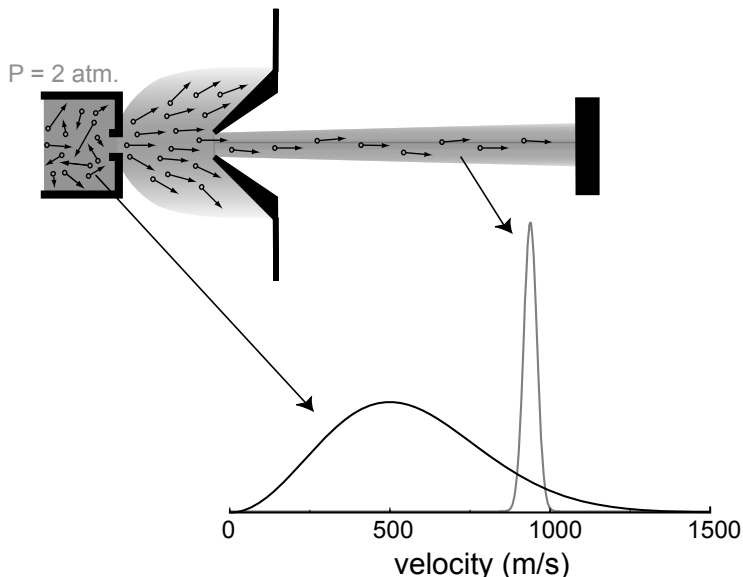


Figure 3.1: *Molecular velocities before and after beam expansion. A high-pressure thermalized gas is expanded through a small hole into vacuum. Each arrow depicts the direction and magnitude of the velocity of an individual molecule. Additionally the velocity distribution of the molecules in the reservoir vs. the distribution of the resulting supersonic beam are plotted. Adapted from Bethlem et al. (with permission) [58].*

Since all the molecules are moving at about the same fast velocity, the collisions between them in the expanded gas will be low in energy; at some point the density becomes too low to permit any further collisions and no further cooling will occur. After this occurs, the properties are often said to be ‘frozen-in’ [70], [71]. The translational temperature of the beam is  $< 1$  K. In general, the equilibration between translational and rotational motion is very fast, leading to a rotational temperature of  $< 5$  K. The equilibration between translational and vibrational motion is much slower, typically yielding temperatures around 50 K, but for light molecules this still implies that only a tiny fraction is in the excited vibrational state.

For our experiments, not only the low temperature is important, but also the high density of molecules in the molecular beam; densities of  $10^{13}$  molecules/cm<sup>3</sup> and per quantum-state can be achieved in these pulsed beams. The amount of molecules per space interval (density) and velocity interval (temperature) is known as the phase-space density. The phase-space density can be defined as

$$D = n\Lambda^3, \quad (3.1)$$

where  $n$  is the number density and  $\Lambda = (2\pi\hbar^2/mkT)^{1/2}$  is the thermal de Broglie wavelength. Equation (3.1) is a measure of the de Broglie wavelength of the particles in terms of their separation, and is also referred to as the degeneracy parameter of a gas. As this parameter increases towards one, the de Broglie wavelength of the molecules begins to overlap and quantum-degeneracy can occur [72], [73].

If the expansion is assumed to be adiabatic, the number density of the beam during the expansion is given by

$$n = n_0 \left( \frac{T}{T_0} \right)^{1/(\gamma-1)}, \quad (3.2)$$

where  $T_0$ ,  $n_0$  and  $T$ ,  $n$  are the temperatures and number densities of the gas in the container and in the beam, respectively, and  $\gamma = C_p/C_v$ , where  $C_p$  and  $C_v$  are the specific heat capacities of a gas at a constant pressure or volume, respectively [6]. The phase-space density of molecules in the beam,  $D$ , can then be expressed in terms of the initial phase-space density in the container,  $D_0$ , as

$$D = D_0 \left( \frac{T}{T_0} \right)^{\frac{5-3\gamma}{2(\gamma-1)}}. \quad (3.3)$$

Note that  $\gamma$  depends on the gas, that is  $\gamma$  can be related to the degrees of freedom,  $f$ , for an ideal gas by  $\gamma = \frac{(f+2)}{f}$ . For a monoatomic gas  $\gamma = \frac{5}{3}$ , which results in a phase-space density that remains constant during the expansion, i.e.,  $D = D_0$ . Molecules have more degrees of freedom, therefore  $\gamma$  is closer to 1. For small molecules, like  $\text{ND}_3$ , the population in the excited vibrational levels can be neglected, and only the rotational degrees of freedom need to be taken into account; for  $\text{ND}_3$  at room temperature  $\gamma = \frac{9}{7}$ . In this case, the phase-space density decreases during the expansion. Note that in our definition, the phase-space density is integrated over all internal degrees of freedom. In the expansion, the internal temperature decreases and the population of the lowest levels increases. The decrease in phase-space density is therefore merely a consequence of the entropy release associated with this internal cooling.

In our seeded beams, the fraction of  $\text{ND}_3$  molecules is very small, so the heat released by the  $\text{ND}_3$  molecules is negligible. Therefore, the temperature and density of the mixed beam are essentially the same as those in a pure Xe beam, and the phase-space density of the  $\text{ND}_3$  molecules (integrated over all levels) is approximately the same as in the container. The phase-space density of molecules in their rotational ground state will actually greatly increase. Let us calculate the phase-space density of our pulsed beam, produced by seeding 5 % ammonia in Xenon at a backing pressure of 2 atm and a temperature of 200 K. Using  $PV = nk_bT$ , the density of  $\text{ND}_3$  molecules in the container is determined to be  $3.6 \times 10^{18}$  molecules/cm<sup>3</sup>. At this temperature  $\Lambda = 0.28 \text{ \AA}$ , yielding a phase-space density of  $\text{ND}_3$  molecules integrated over all levels of  $7.9 \times 10^{-8}$ . In

the beam, the translational temperature is taken to be 2 K, thus the  $\Lambda$  becomes 2.8 Å and following Equation 3.2 the number density of ND<sub>3</sub> molecules in the beam, using an average  $\gamma$  for the gas mixture, becomes  $3 \times 10^{15}$  molecules/cm<sup>3</sup>. Note that the densities used in this work are three orders of magnitude lower than those calculated for the ideal situation. The difference is attributed to the fact that the expansion is not perfectly adiabatic. Solving Equation 3.3 (or Eq. 3.1) yields the phase-space density of the lowest rotational levels, as only these will be populated in the beam; of this population roughly 20 % of the ND<sub>3</sub> molecules will be in the  $|J, MK\rangle = |1, -1\rangle$  level, yielding a phase-space density of ND<sub>3</sub> molecules in this quantum state of  $1.3 \times 10^{-8}$ .

### 3.2.2 Stark deceleration of polar molecules

The Stark decelerator exploits the interaction of polar molecules in selected quantum-states with time-varying electric fields to manipulate their motion. Figure 3.2 depicts the basic principle of the Stark decelerator. One deceleration stage is comprised of two parallel, cylindrical, metal rods. One of the rods is connected to a positive and its partner to a negative switchable high-voltage power supply; alternating rods along the axis are connected to each other. The strength of the electric field is higher near the electrodes than on the molecular beam axis. Therefore, molecules in a low-field-seeking (lfs) state will be focused towards the beam axis. This focusing occurs only in the direction perpendicular to the electrodes; in the direction parallel to the electrodes there is practically no focusing. To achieve a net focusing effect in both transverse directions throughout the Stark decelerator, the electric field stages are alternately oriented vertically and horizontally; for clarity, all electrodes are depicted in the same direction in Figure 3.2.

In this configuration, the Stark energy  $W(z)$  of a molecule in a low-field-seeking quantum state is periodic ( $2L$ ) along the beam axis ( $z$ -axis). Suppose a lfs molecule is entering an electric field, as illustrated in Figure 3.2. This molecule gains Stark energy at the expense of kinetic energy (see Chapter 2, Figure 2.12). If nothing would change, this molecule would regain its kinetic energy upon exiting the field. However, switching off this field while the molecule is still in the high electric field region, results in a permanent loss of kinetic energy. The kinetic energy that can be extracted in a single deceleration stage is typically 0.1-0.2 meV ( $\simeq 1 - 2 \text{ cm}^{-1}$ ). Note that the initial kinetic energy of the molecules in the beam is at least 10-20 meV (ca.  $100 \text{ cm}^{-1}$ ). Thus, in order to make a significant change to the molecule's velocity, the process needs to be repeated many times. This is accomplished by switching the fields such that  $W(z)$  is repeatedly shifted over a distance  $L$ , keeping the movement of the fields synchronous with the movement of the molecules along the beam axis [74].

The amount of energy that a molecule will lose depends on its position at the time that the fields are switched. Borrowing terms from particle accelerator physics, this position is denoted as the *phase* or *phase-angle*,  $\phi = 2\pi(z/2L)$ .

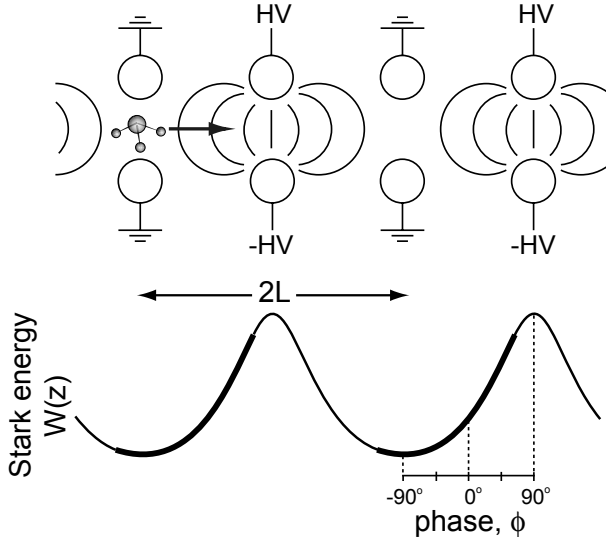


Figure 3.2: Scheme of the Stark decelerator. The Stark energy of a  $\text{ND}_3$  molecule in a low-field-seeking quantum state is shown as a function of  $z$ -position along the molecular beam axis. The energy a molecule loses per stage depends on its position at the time that the fields are switched; this position is denoted in terms of a “phase” or “phase-angle” that has a periodicity of  $2L$ . If the fields are switched at a  $0^\circ$  phase-angle, molecules will be neither decelerated nor accelerated; if switched at a  $90^\circ$  phase-angle, molecules will be decelerated the maximum amount. The bold line along  $W(z)$  marks the part of the potential experienced by the molecule with a typical phase-angle of  $70^\circ$ .

Molecules that are in the maximum electric field just prior to the fields being switched off are assigned a phase-angle  $\phi = 90^\circ$  [75], as marked in Figure 3.2. These molecules lose the maximum amount of energy possible per stage. Conversely, if molecules would gain the maximum amount of energy if the fields were switched at a  $\phi = -90^\circ$  phase-angle. If the fields are switched at a  $0^\circ$  phase-angle, molecules will be neither decelerated nor accelerated, but simply guided through the Stark decelerator.

To describe the motion of an ensemble of molecules through the Stark decelerator, it is convenient to express their position and velocity relative to the position and velocity of one “synchronous molecule” - so called because the switching of the fields is synchronized to this particular molecule. The phase and velocity of the synchronous molecule are designated as  $\phi_s$  and  $v_s$ , respectively. The synchronous molecule always travels exactly a distance  $L$  in the time interval  $\Delta T$  between the switching of the fields. Per definition it always has the same phase  $\phi_s$ , and loses the same amount of kinetic energy per stage.

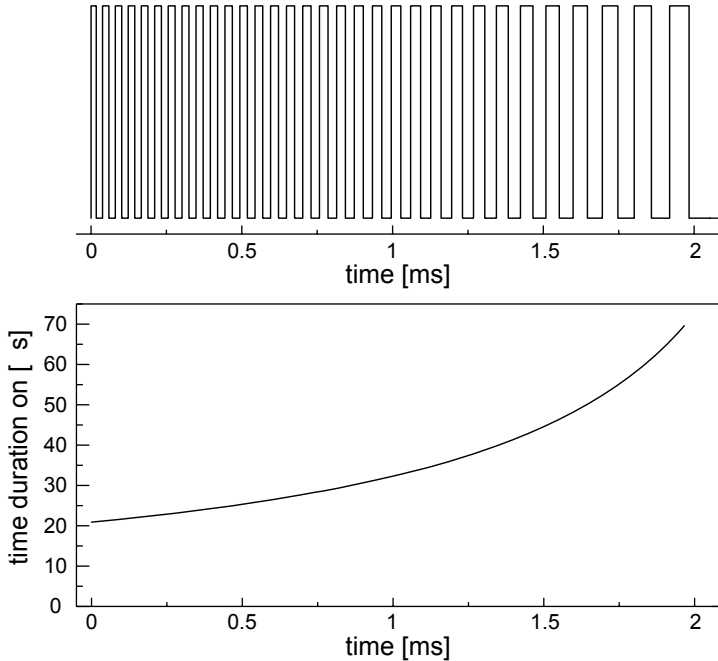


Figure 3.3: Time sequence for a typical pulse sequence (upper part) for decelerating  $\text{ND}_3$  molecules in a Stark decelerator from an initial velocity of 266 m/s down to 87 m/s. The time duration for each deceleration stage is shown (lower part) for the same time sequence. As the molecules are decelerated, they take longer to transverse the distance between the deceleration stages, hence the time duration between switches increases.

To assure this,  $\Delta T$  must be increased as the synchronous molecule is decelerated. An example of a typical time sequence applied to the Stark decelerator to switch the electric fields is depicted in the upper part of Figure 3.3, and the time duration for each deceleration stage is shown in the lower part of Figure 3.3. For the time sequence in Figure 3.3, a  $\text{ND}_3$  molecule with an initial velocity of 266 m/s is decelerated to 87 m/s. The pulse sequence lasts ca. 2 ms over 62 stages ( $L = 5.5$  mm) of deceleration at a  $70^\circ$  phase-angle. The time duration triples from the first to the last deceleration stages.

The relevance of the notion of a synchronous molecule is that other molecules, which are close to the synchronous molecule, feel a force towards the synchronous molecule and oscillate around it. Let us consider a typical deceleration experiment with  $\phi_s = 70^\circ$ ; the corresponding section of the  $W(z)$  curve for this phase-angle is marked in bold in Figure 3.2. A molecule slightly ahead of the synchronous molecule, but with the same velocity, loses more energy per

stage than the synchronous molecule. Hence, it is slowed down with respect to the synchronous molecule, and consequently its phase becomes smaller. This process repeats itself until the molecule's phase has become smaller than  $\phi_s$ , at which point it lags behind the synchronous molecule. Now the situation is reversed and this molecule loses less energy, i.e., it speeds up, with respect to the synchronous molecule, etcetera. This example illustrates that molecules with phase-space coordinates slightly different from  $(\phi_s, v_s)$  oscillate both in phase and velocity around the synchronous molecule. The molecules are trapped in a travelling potential well moving along with the synchronous molecule as described in Section 2.1.2 in the synchrocyclotron. Note that in phase-space, the non-synchronous molecules rotate around the position of the synchronous molecule.

The range of positions and velocities that is accepted by the decelerator is determined by  $\phi_s$ , which is set to  $0 \leq \phi_s \leq 90^\circ$  for deceleration experiments. The larger the phase-angle, the more kinetic energy that can be extracted per stage. However, more molecules are accepted for smaller phase-angles. As both a large deceleration and a large acceptance are desired, a compromise must be found - typically  $\phi_s$  is chosen between  $50^\circ$  and  $70^\circ$ .

Figure 3.4 shows the calculated phase-space distribution of an ensemble of ammonia molecules as they pass through the decelerator. For eight different times, the longitudinal velocity of the molecules is given as a function of their position along the beam axis ( $z$ ). In this simulation, the fields are switched such as to decelerate molecules from 272 m/s to 92 m/s using a synchronous phase of  $\phi_s = 70^\circ$ . The forward tilting of the phase-space distribution upon increasing time reflects the (almost) free flight of the molecules that are not accepted by the decelerator. A packet of molecules is seen to stay together as a "bunch" while being decelerated. In fact, a few decelerated bunches, trailing each other by a distance of 11 mm, are observed. This results from the position spread of the beam being about 30 mm at the entrance of the decelerator, which is almost three times the period  $2L = 11$  mm. Therefore, more than one travelling well ("bucket") will be filled. The inset shows the longitudinal phase-space distribution of a decelerated bunch relative to the position of the synchronous molecule, i.e., in the moving frame  $(z, v)$  of the synchronous molecule. The decelerated packet has a position spread of 2 mm and a velocity spread of 8 m/s. The solid curves in the inset result from a simple model for phase-stability [76]. Note that for a given decelerator geometry, the position and velocity spread are independent of the initial and final velocities, but are solely determined by the phase-angle. The phase-space density of the packet stays constant throughout the deceleration process, as dictated by the Liouville theorem [57].

As aforementioned, to establish transverse stability, successive pairs of electrodes are orientated at  $90^\circ$  angles relative to each other [74]. The actual transverse well depends on the synchronous phase. When operated at a phase angle of  $\phi_s = 70^\circ$ , our decelerator accepts molecules with transverse position

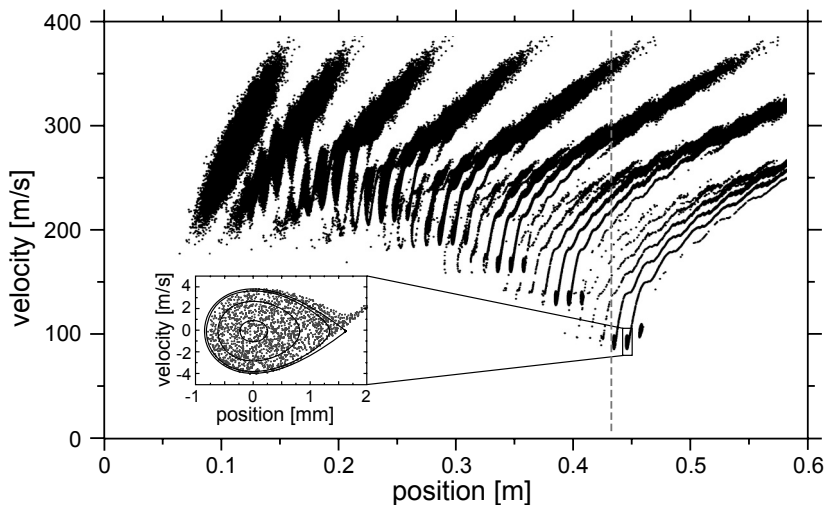


Figure 3.4: Numerical simulations of the phase-space distribution of an ensemble of  $\text{ND}_3$  molecules is shown for eight different times as the ensemble passes through the decelerator. In the inset, the phase-space distribution of a decelerated packet is shown in the moving frame of the synchronous molecule. The dashed vertical line indicates the position at which the TOF measurements shown in Figure 3.8 are taken.

and velocity spreads of 1 mm and 5 m/s, respectively [75].

### 3.2.3 Longitudinal bunching

As described above, the Stark decelerator can be used to produce a packet of molecules with a well-defined distribution in phase-space. Upon leaving the decelerator, this confined distribution spreads out in both the longitudinal and transverse directions. During free-flight, the longitudinal phase-space distribution of the packet elongates. The faster molecules pull ahead of the synchronous molecule while the slower ones lag behind; thus, the free-flight establishes a linear relation between the position of the molecule and its velocity. After free-flight over a distance  $L_1$ , a buncher - named after the device used in particle accelerators (see Section 2.2.1) - is used to longitudinally focus the molecules into the detection region, which is located a further free-flight distance  $L_2$  away. Hexapoles are used before and after the buncher to transversally focus the molecules into the buncher and into the detection region, respectively.

A schematic drawing of the buncher is shown in Figure 3.5. The buncher consists of five pairs of electrodes, with each pair being comprised of two parallel, cylindrical, metal rods. The rods are connected to either a positive or

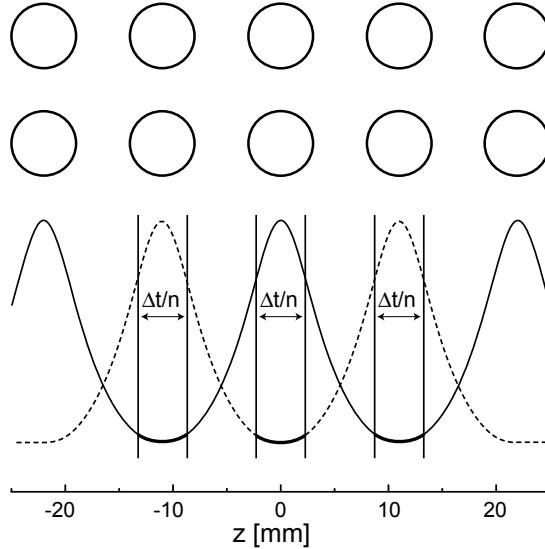


Figure 3.5: *Schematic drawing of the buncher, together with the Stark potential energy of a molecule in a low-field-seeking state as a function of  $z$ -position along the molecular beam axis.*

negative switchable high-voltage power supply; alternating rods are connected to each other, and successive pairs of electrodes are orientated at  $90^\circ$  angles relative to each other (not shown in the Figure) [77]. In this Figure, the Stark energy of a lfs molecule along the molecular beam axis ( $z$ ) is given for the case when either the odd (solid curve) or even (dotted curve) pairs of electrodes are switched to high voltages, while the others are grounded. The electric field in the buncher is turned on for a total time  $\Delta t$ . The field in the buncher is switched on when the synchronous molecule arrives at the position indicated with the left most vertical line in Figure 3.5 (when using the odd pair of electrodes); the field is switched off again when it arrives at the position indicated by the next vertical line. During this time-interval (marked by  $\Delta t/n$  in the Figure), the synchronous molecule is equally accelerated and decelerated, as it spends the same amount of time on the downward and upward slopes of the Stark potential energy curve. Molecules ahead of the synchronous one, i.e., molecules that were originally faster, spend more time on the upward slope than on the downward slope of the potential, and thus are decelerated with respect to the synchronous molecule. Likewise, molecules that are behind the synchronous molecule are accelerated with respect to the synchronous molecule. This process is repeated  $n$  times, where  $n$  has a maximum value of three for the present buncher.

The longitudinal phase-space distribution is sketched in Figure 3.6 at four



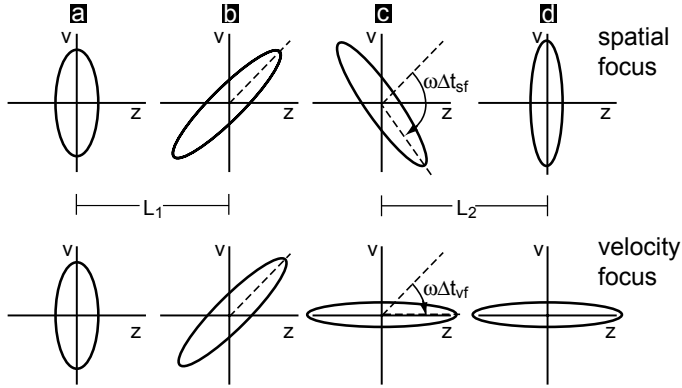


Figure 3.6: Sketches of the longitudinal phase-space distribution at four different times, namely when the synchronous molecule is at (a) the exit of the decelerator, (b) the entrance of the buncher, (c) the exit of the buncher, and (d) the detection region. The upper and lower series illustrate spatial and velocity focusing (as labelled). While moving from the exit of the decelerator to the detection region, the packet is rotated in phase-space either over (a total of)  $180^\circ$  for spatial focusing or over  $90^\circ$  for velocity focusing.

different times, for two different time-intervals ( $\Delta t$ ) that the buncher is on. The distributions are shown in the moving frame of the synchronous molecule, i.e., the synchronous molecule is always located at the origin. The phase-space distributions are plotted when the synchronous molecule is at (a) the exit of the decelerator, (b) the entrance and (c) the exit of the buncher, and (d) the detection region. Clearly seen here is the elongation and tilting of the phase-space distribution during free-flight over the distance  $L_1$ . During the time  $\Delta t$  that the buncher is on, the longitudinal phase-space distribution is uniformly rotated, with an angular frequency  $\omega$ , in the  $(z, v)$ -plane. In the upper panel of Figure 3.6,  $\Delta t$  is chosen such that a spatial focus is formed in the detection region. When the buncher is on for a shorter time, the distribution is rotated over a smaller angle  $\omega\Delta t$ . This is sketched in the lower panel of Figure 3.6, where the longitudinal velocity spread is minimized - this “velocity cooling” is equivalent to creating a spatial focus at infinity. Keeping in analogy with charged particle physics’s terms, the spatial and velocity focusing are referred to as “re-bunching” and “bunch rotation,” respectively [77].

The time-interval ( $\Delta t$ ) that the buncher needs to be turned on to achieve a particular longitudinal focus can be analytically evaluated using the matrix method (see Section 2.2.2). With this method, the final position of a molecule in longitudinal phase-space ( $z', v'$ ) can be determined as follows

$$\begin{pmatrix} z' \\ v'/\omega \end{pmatrix} = \mathbf{M} \begin{pmatrix} z \\ v/\omega \end{pmatrix}, \quad (3.4)$$

where  $\mathbf{M}$  is the transfer matrix, and  $(z, v)$  is the original position of the molecule in phase-space. Note that these coordinates are all in the moving frame of the synchronous molecule. Dividing the velocity by the angular frequency  $\omega$  has the advantage that the elements of the transfer matrix become dimensionless. The transfer matrix that describes the molecular motion during free flight over  $L_1$ , within the buncher, and during free flight over  $L_2$  can be written as the product

$$\mathbf{M} = M_{O2}M_F M_{O1} \quad (3.5)$$

with

$$\begin{aligned} M_{O1} &= \begin{pmatrix} 1 & \omega \frac{L_1}{v_s} \\ 0 & 1 \end{pmatrix} && \text{free flight} \\ M_F &= \begin{pmatrix} \cos \omega \Delta t & \sin \omega \Delta t \\ -\sin \omega \Delta t & \cos \omega \Delta t \end{pmatrix} && \text{buncher} \\ M_{O2} &= \begin{pmatrix} 1 & \omega \frac{L_2}{v_s} \\ 0 & 1 \end{pmatrix} && \text{free flight} \end{aligned} \quad (3.6)$$

We can use the approximation that  $\omega \Delta t \ll 1$ , i.e.,  $\cos \omega \Delta t \approx 1$  and  $\sin \omega \Delta t \approx \omega \Delta t$ , and that  $\Delta t \ll (L_1 + L_2)/v_s$ . This enables us to calculate the time interval  $\Delta t$ , needed for a molecule to arrive in the detection region simultaneously with the synchronous molecule, i.e.,  $\Delta t$  for re-bunching. This is done by setting  $z' = 0$  in Equation 3.4 and solving for  $\Delta t$ , as a function of the initial phase-space position  $(z, v)$ . The result can be written as:

$$\Delta t|_{z'=0}(z, v) = \frac{v_s(zv_s + v(L_1 + L_2))}{\omega^2 L_2(zv_s + vL_1) - vv_s^2}. \quad (3.7)$$

Likewise, the time-interval  $\Delta t$ , can be calculated such that a molecule has the same velocity as the synchronous molecule at the time that the latter arrives in the detection region, i.e.,  $\Delta t$  for bunch-rotation. For this,  $v' = 0$  in Equation 3.4, leading to:

$$\Delta t|_{v'=0}(z, v) = \frac{vv_s}{\omega^2(zv_s + vL_1)}. \quad (3.8)$$

Equation 3.7 and Equation 3.8 describe a distribution of time-intervals  $\Delta t$ . At the peak of the  $\Delta t|_{z'=0}(z, v)$  distribution, there is a maximum number of molecules that arrive in the detection region simultaneously with the synchronous molecule, i.e., a spatial focus is achieved. Similarly, at the peak of the  $\Delta t|_{v'=0}(z, v)$  distribution, there is a maximum number of molecules that have obtained the same velocity as the synchronous one, i.e., a velocity-focus

is achieved. As the original phase-space distribution  $(z, v)$  is centered around  $(0, 0)$ , it follows that the spatial focus is obtained at

$$\Delta t_{sf} = \frac{v_s (L_1 + L_2)}{\omega^2 L_1 L_2 - v_s^2}. \quad (3.9)$$

Likewise, from Equation 3.8, the velocity focus is obtained at

$$\Delta t_{vf} = \frac{v_s}{\omega^2 L_1}. \quad (3.10)$$

As expected, Equation 3.9 reduces to Equation 3.10 when  $L_2$  goes to infinity.

### 3.2.4 Transverse focusing

Briefly, I will address the transverse focusing of the hexapoles. The hexapoles consist of six cylindrical rods with radius  $R_{\text{rod}}$  placed equidistantly around a circle with radius  $R_{\text{hex}} = 2R_{\text{rod}}$ . The rods are alternatingly at ground potential and at high voltage, creating a cylindrically symmetric electric field as described in Section 2.2.5. Rather than the common practice of continuously applying a constant voltage to the hexapole rods, the electric field is applied for a short time-interval. It is advantageous to use high fields in the hexapole for short times, instead of using low fields for long times, as this reduces the unwanted effects of non-linearities associated with the inversion splitting in ammonia (see Figure 2.14). Also, this enables us to effectively vary the focusing strength and position of the hexapole lens. The motion of the molecules through the hexapole in the transverse direction can be evaluated using the matrix method, in the same manner as above. The use of two hexapoles allows for variations to the ratio  $\frac{\Delta x}{\Delta v_x}$  and  $\frac{\Delta y}{\Delta v_y}$ . In this scenario, the phase-space density must also remain constant, so a decrease in  $\Delta x$  and  $\Delta y$  implies an increase in  $\Delta v_x$  and  $\Delta v_y$ . In phase-space, this means that the packet's image stays the same but the axes-values change. This capability is critical for matching the phase-space distribution of the decelerator onto that of the ring and to ensure that the maximum amount of molecules are accepted into the ring; this will be discussed in Chapter 5.

## 3.3 Experimental setup

The compact molecular beam machine used for the present experiments is shown schematically in Figure 3.7, and is pictured below it. The apparatus consists of two differentially pumped vacuum chambers separated by a skimmer with a 1 mm diameter opening. The source and decelerator chambers are both pumped by 500 l/s turbo pumps. A gas mixture consisting of about 5 % ND<sub>3</sub> in Xenon at a backing pressure of 2 atm is expanded into vacuum using a solenoid valve pulsed at 10 Hz. The solenoid valve (General Valve Series 9) is

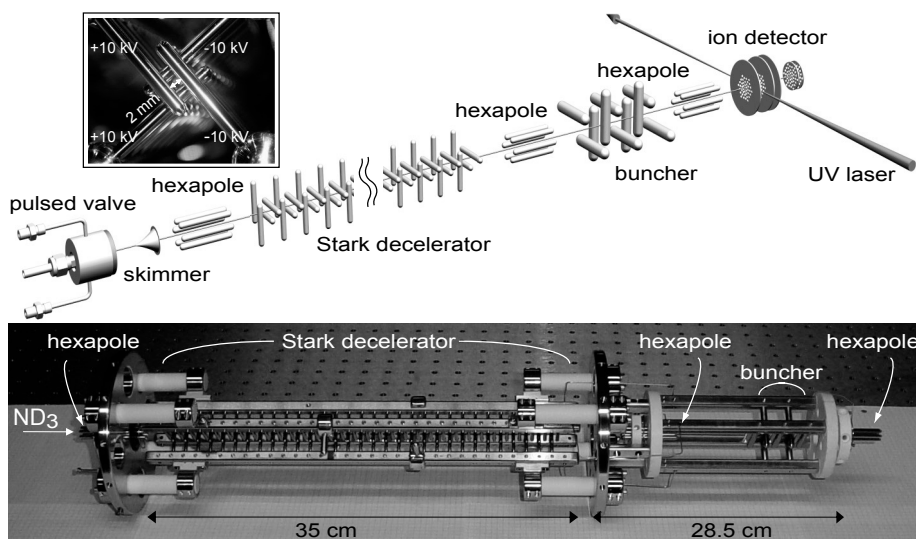


Figure 3.7: Scheme of the molecular beam machine.  $\text{ND}_3$  molecules seeded in Xe expand through a nozzle at a 10 Hz rate. After passing through a skimmer, molecules in the lfs  $|J, KM\rangle = |1, -1\rangle$  level are focused with a hexapole into the Stark decelerator. After deceleration the molecules pass through a hexapole-buncher-hexapole combination prior to entering the detection region. There, the density of the ammonia molecules is state-selectively detected using a UV-laser ionization scheme (2+1 REMPI). Below, a photo is shown of the main components: (from left to right) hexapole, decelerator, hexapole, buncher, hexapole. In the boxed inset, a photo is shown of the electrodes at the entrance of the Stark decelerator looking along the beam axis.

modified such that it can be operated down to liquid nitrogen temperatures. In these experiments, the valve is cooled to 200 K, and opens for a duration of 100  $\mu\text{s}$ . Under operation conditions, the pressure in the source and deceleration chamber is typically  $8 \times 10^{-6}$  and  $2 \times 10^{-8}$  mbar, respectively\*. In the molecular beam, only the lowest rotational levels in the electronic and vibrational ground state are occupied. In our beam, ca. 60 % of all  $\text{ND}_3$  molecules reside in the ground state of para-ammonia, of these one-third are found in the low-field seeking  $|J, KM\rangle = |1, -1\rangle$  level [75].

After passing through the skimmer, the beam is focused with a pulsed hexapole into the Stark decelerator. The Stark decelerator consists of 63 pairs

\*These values refer to the measurements in this chapter. For measurements using the synchrotron in the next few chapters, the pressure in the source chamber was typically a little higher, at about  $1 \times 10^{-5}$  mbar; the increase in the pressure of the deceleration chamber was negligible.

of highly polished, stainless steel electrodes, and has a total length of 35 cm. The cylindrical electrodes have a diameter of 3 mm with successive pairs separated by  $L = 5.5$  mm (center-to-center), leaving a 2 mm gap for the molecular beam to pass through, as seen in the photograph of the entrance to the Stark decelerator in the boxed inset of Figure 3.7. As mentioned before, successive electrode pairs are alternately orientated horizontally and vertically. The electrodes are suspended by four metal bars, which are connected to two positive and two negative high voltage switches. In these experiments, a voltage difference of 20 kV is applied across an electrode pair, creating a maximum electric field of 90 kV/cm on the molecular beam axis.

After exiting the Stark decelerator, the molecules pass through a second pulsed hexapole, and are focused into the buncher, a distance of  $L_1 = 192$  mm away. The buncher has a geometry identical to that of our decelerator, but with all dimensions scaled up by a factor of two. Behind the buncher, a third pulsed hexapole is mounted. All three hexapoles are comprised of six, cylindrical, stainless steel rods with a radius  $R_{\text{rod}} = 3$  mm; the first hexapole has a length of 60 mm, and the second and third hexapoles both have a length of 50 mm. Finally, the molecules travel into the detection region at a distance  $L_2 = 170$  mm behind the buncher, implying a total length of the beamline of about 70 cm. The molecules in the  $|J, K\rangle = |1, 1\rangle$  upper component of the inversion doublet are detected here via a (2+1) resonance-enhanced multiphoton ionization (REMPI) scheme [78]. The laser light, with a typical energy of 15 mJ around 317 nm in a 5 ns duration pulse, is focused into the detection region using a lens with a 75 cm focal length. Mass-selective detection of the parent ions is performed using hexapole electrodes (not shown in the Figure - details of the hexapole ring setup will be given in Chapter 4) as extraction electrodes in a Wiley-McLaren type [79] mass spectrometer setup. The ion signal is proportional to the density of the ammonia molecules in the detection region.

The Stark decelerator, buncher, and hexapoles are all suspended and isolated using ( $\text{Al}_2\text{O}_3$ -) ceramics. They are mounted and aligned as one unit, as shown in the photo in Figure 3.7. The decelerator, the buncher, and the hexapoles are all electrically connected. The switching of the entire unit is then accomplished with only four fast, high voltage switches (Behlke Electronic GmbH, HTS-151-03-GSM), and using two high voltage power supplies (FUG, HCN 700-12500). A bias voltage of +150 V is applied to the positive electrodes to prevent losses due to Majorana transitions to the  $|J, K M\rangle = |1, 0\rangle$  level, which is not a low-field-seeking state. The switches are triggered by a programmable delay generator running at a clock frequency of 100 MHz. The sequence of timings, during which fields are switched, is generated using a computer program that calculates the trajectory of the synchronous molecule through the beam machine. Typical time sequences last for less than 10 ms, and a new time sequence, or ‘burst’, can be loaded at a 10 Hz rate. Scans and burst execution are controlled by the program package KouDA [80].

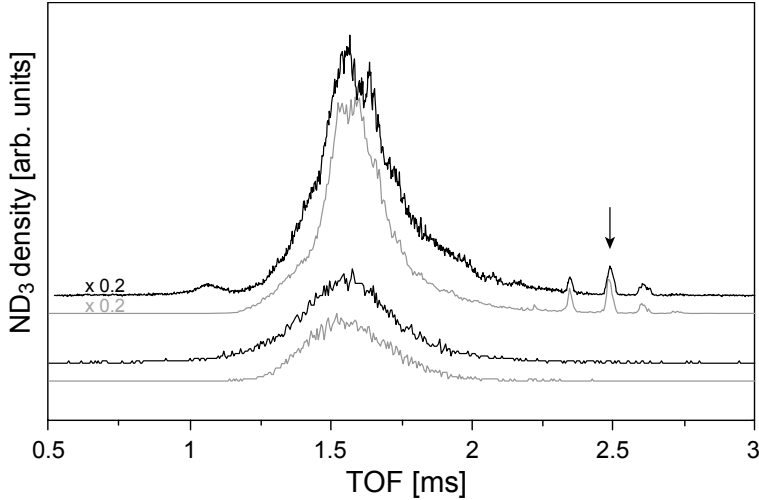


Figure 3.8: Density of  $\text{ND}_3$  molecules recorded 25 mm behind the decelerator as a function of time after the release of the gas pulse ( $t_0 = 0$ ). The lower and upper black curves show the TOF profiles of the original and decelerated (272 m/s to 92 m/s) beams, respectively. The gray curves are results of numerical simulations of the experiment. At least three bunches of slow molecules are seen to arrive in the detection region about 1 ms later than the original beam; the synchronous packet is denoted by the arrow. Note that the signal increases by more than an order of magnitude, due to the transverse focusing, when the voltages in the decelerator are switched on. Adapted from Bethlem *et al.* (with permission) [75].

## 3.4 Experimental results and discussion

### 3.4.1 The beamline: Stark decelerator

To demonstrate the performance of the Stark decelerator, I first present measurements taken directly behind the decelerator [75]. In Figure 3.8, the density of the  $\text{ND}_3$  molecules 25 mm behind the decelerator is shown as a function of time after the release of the gas pulse ( $t_0 = 0$ ). The lower black curve shows the time-of-flight (TOF) profile of the original beam (no voltages). The mean velocity of the ammonia molecules in the beam is 285 m/s. The upper curve shows the TOF profile of the beam when the Stark decelerator is used to slow down molecules from 272 m/s to 92 m/s using a phase-angle of  $70^\circ$  (the undecelerated part of the beam is also shown). The gray curves beneath the data show the results of a 3D numerical simulation of the experiment using calculated electric fields and the Stark effect of  $\text{ND}_3$  as input. The Gaussian velocity distribution that has been used as input for the numerical simulation

of the decelerated beam has been adjusted to match the observed TOF profile of the original beam. Three bunches of slow molecules are seen to arrive in the detection region about 1 ms after the undecelerated part of the beam. The transverse focusing in the decelerator leads to an increase of signal over the entire TOF profile by more than an order of magnitude when the voltages are turned on. In fact, the peak intensity of the decelerated signal is larger than the peak intensity of the original beam. The simulations are seen to quantitatively reproduce the TOF profiles. Note that the parameters set for this measurement were used to calculate the phase-space distributions presented in Figure 3.4.

Of the three decelerated bunches in Figure 3.8, the central (main) bunch contains molecules that had their initial position and velocity centered around those of the synchronous molecule, and passed through all the deceleration stages while they were being switched; these molecules have been decelerated from 272 m/s to 92 m/s and are denoted by the arrow. The earlier bunch contains molecules with the same initial velocity of 272 m/s, but which happened to be located 11 mm, or one ( $2L$ -)period, ahead of the synchronous molecule when the decelerator was first switched on. Throughout the decelerator, this bunch travels 11 mm ( $2L$ ) ahead of the synchronous packet, and of course, exits the decelerator first. Thus, these molecules experience less deceleration than the synchronous packet by two stages – resulting in a slightly higher velocity of 102 m/s. Note that this faster bunch is also nicely seen in Figure 3.4. The later bunch, on the other hand, contains molecules which had a lower initial velocity of 268 m/s, exactly one period’s worth less of energy, and entered the decelerator one period later. These molecules trail the main bunch by exactly 11 mm throughout the decelerator, and are still in the decelerator when the time sequence is completed. Although these molecules also experience two-stages-worth of deceleration less (since the switching stops as the synchronous packet exits the decelerator), owing to its lower initial energy the trailing packet still has the same final velocity, 92 m/s, as the synchronous packet. In order to guarantee a large separation distance between packets, the decelerator can be switched two extra times purposely to slow down the trailing packet; the extra switching will not affect the synchronous packet, as it is already outside of the decelerator at this time.

The final position spread,  $\Delta z_f$ , of the undecelerated part of the beam in the detection zone is determined by both the beam’s initial position spread,  $\Delta z_i$ , and its velocity spread,  $\Delta v_z$ , according to

$$\Delta z_f = \sqrt{(\Delta z_i)^2 + (\Delta v_z \cdot t)^2}, \quad (3.11)$$

where  $t$  is the flight-time. A Gaussian fitted to the TOF profile in Figure 3.8 yields a  $\Delta z_f$  of 110 mm in the detection zone. One can determine  $\Delta z_i$  of the undecelerated beam by scanning the delay time between the gas pulse release ( $t_0 = 0$ ) and the start of the time sequence, as shown in Figure 3.9. As

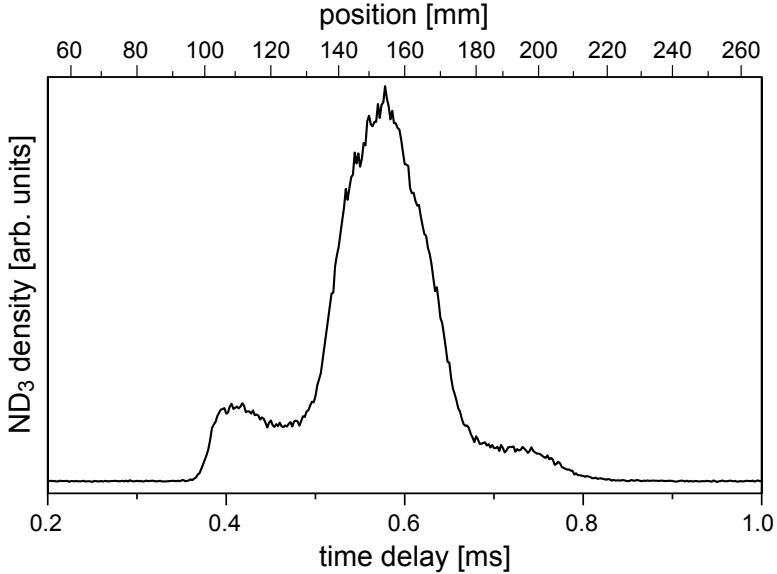


Figure 3.9: *The density of  $\text{ND}_3$  molecules as a function of delay time between the release of the gas pulse and the switching on of the Stark decelerator. This directly characterizes the position spread of molecules in the beam expansion moving at a forward velocity of exactly 266 m/s at the entrance to the decelerator.*

aforementioned, the initial velocity which is sliced out of the distribution is determined by the desired final velocity and phase-angle. Here the molecules are decelerated down to 87 m/s with a  $60^\circ$  phase-angle, so the initial velocity must be 266 m/s. Thus, this measurement directly probes the  $\Delta z_i$  of molecules with a velocity of 266 m/s. The position spread determined from fitting a Gaussian to the curve in Figure 3.9 is 30.6 mm (not including the shoulder features). This spread quantitatively agrees with Figure 3.8, in which three “buckets” separated by 11 mm are seen to be accepted into the decelerator. It is important to mention that this value only reflects the spread of molecules with a low initial velocity, which happens to be the most intense part of the beam. The actual beam width is expected to be larger. Note that the velocity distribution over the pulse varies. So similar measurements centered around other initial velocities might look very different. The odd features of the graph probably reflect this velocity discrepancy, as well as the features of how the nozzle itself opens.

Substituting  $\Delta z_i$  and  $\Delta z_f$  into Equation 3.11 and the arrival time of  $t = 1.55$  ms taken from Figure 3.8, one can solve for  $\Delta v_z$  of the original beam (no voltages). This yields a velocity spread of 68 m/s. When comparing the spread



of the beam to the average velocity,  $\Delta v/\bar{v}$ , a beam spread of ca. 24% is found. As there is no change to the molecules' velocity in this free flight, the initial and final velocity distribution is the same. Note that the initial position spread is much smaller than the  $\Delta v \cdot t$  term, i.e., the  $\Delta v_z$  is the dominant term defining  $\Delta z_f$ .

Although the beam is not in a thermal equilibrium, a translational temperature can be assigned to the beam from the  $\Delta v_z$  in the relationship

$$T = \frac{m\Delta v_z^2}{8 \ln 2 \cdot k_b}, \quad (3.12)$$

where  $m$  is the mass and  $k_b$  is the Boltzmann constant [81]. Note that this temperature definition is in the center-of-mass frame of the moving packet. A spread of 68 m/s corresponds to a translational temperature of 2.0 K.

### 3.4.2 The beamline: focusing elements

To demonstrate the performance of the buncher, measurements are again taken at a distance 36 cm behind the decelerator. For these experiments, ammonia molecules are decelerated from an initial velocity of 266 m/s to a velocity of 85 m/s at the exit of the decelerator. The longitudinal phase-space distribution ( $z, v$ ) of the decelerated package is the same as the one presented in the inset of Figure 3.4, as the phase-angle of the Stark decelerator is set at  $70^\circ$ . In part (a) of Figure 3.10, the density of  $\text{ND}_3$  molecules in the detection region is shown as a function of the time period that the buncher is turned on. The angular frequency,  $\omega$ , experienced by the  $\text{ND}_3$  molecules in the buncher is 2450 rad/s. The buncher is operated here with two stages ( $n = 2$ ), and the total  $\Delta t$  is shown on the horizontal axis. The molecules are detected at the moment that the synchronous molecule is at the center of the detection region. This measurement is best denoted as a longitudinal focusing curve, in analogy with the well-known hexapole focusing curves [6]. The gray curve is the analytically calculated longitudinal focusing curve, that directly follows from equation 3.7 using the experimental values for  $v_s$ ,  $\omega$ ,  $L_1$ , and  $L_2$ ; the initial-phase space distribution is the same as given in Figure 3.4. Time-of-flight measurements have been performed for the  $\Delta t$  values marked on the experimental longitudinal focusing curve with solid circles and arrows. These measurements are displayed in part (b) of Figure 3.10, and show the arrival time distribution of the molecules in the detection region a distance of  $L_2 = 170$  mm behind the buncher. The horizontal axis gives the time relative to the release of the gas pulse. The different TOF profiles are given an offset for clarity, and within the series the vertical scale is the same. The integrated intensity of the series remains almost constant (to within 10%).

The peak of the spatial focusing curve is found at  $\Delta t = 162 \mu\text{s}$ , in agreement with the value of  $\Delta t_{sf} = 163 \mu\text{s}$  found from equation 3.9. The calculated spatial focusing curve is considerably narrower than the measured one. This results

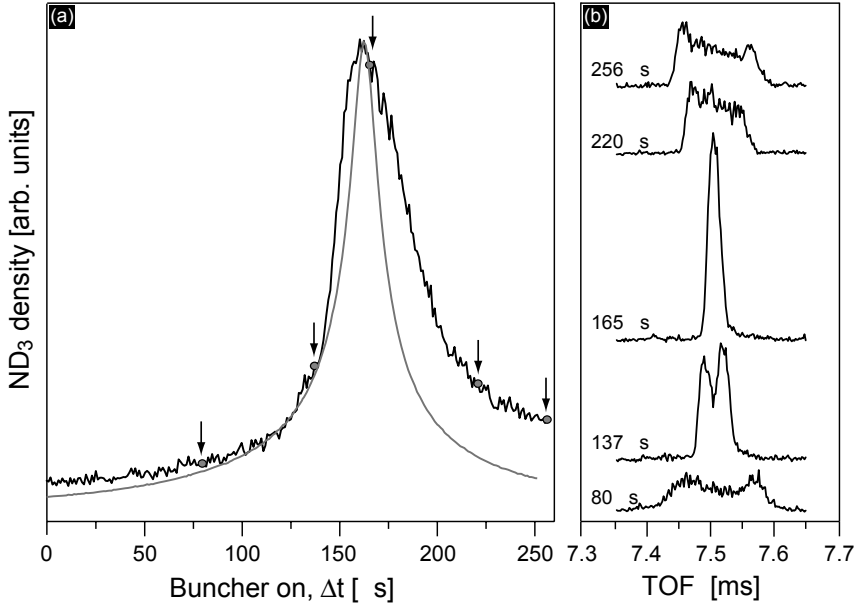


Figure 3.10: In (a) measurements are shown of the density of  $\text{ND}_3$  molecules at a position  $L_2 = 170$  mm behind the buncher as a function of the total time  $\Delta t$  that the buncher is on, together with an analytically calculated distribution. The solid circles and arrows on the longitudinal (spatial) focusing curve mark the bunching times used to obtain the TOF profiles, shown in (b); at  $t = 0$  the gas pulse is released. The measured TOF profiles are given an offset for clarity, and within the series the vertical scale is the same. The integrated signal of the TOF profiles stays constant.

from the neglect of the limited acceptance of the buncher in the calculation; the model does not take into account that the length of the (harmonic part of the) focusing potential in the buncher is finite. The series of TOF profiles nicely shows the transition from an under-focused distribution, via a focus, to an over-focused distribution. In the focus at  $L_2 = 170$  mm, the length of the packet, as deduced from the width of a Gaussian fit to the TOF profile, is about 2 mm. In this case an (almost) 1:1 image of the packet at the exit of the decelerator is made in the detection region, about 36 cm further downstream. The structures observed in the TOF-profiles can be fully explained by including the non-linearities in the buncher, as discussed elsewhere [77], [5].

For transverse focusing, two hexapoles are included into the beamline, one located before the buncher and one located after it; I refer to these hexapoles as the second and third, respectively, as the first hexapole is located before the decelerator. The second hexapole focuses the molecules to a point in between

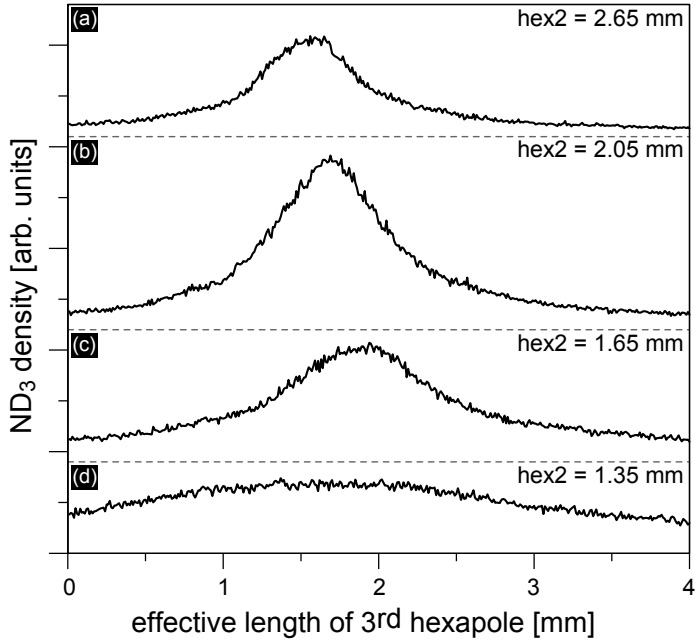


Figure 3.11: *Density of  $\text{ND}_3$  molecules with a forward velocity of 85 m/s in the detection region (36 cm behind the decelerator) as a function of the effective focusing length of the third hexapole for four different effective focusing lengths of the second hexapole. The second hexapole transversally focuses the molecules exiting the decelerator into the buncher, and the third hexapole transversally focuses the molecules exiting the buncher into the detection region.*

the second and third hexapoles, and the third hexapole focuses the molecules into the detection zone. The hexapoles are only switched on for up to  $25 \mu\text{s}$ , corresponding to an effective length of only a few millimeters. The effective position of these electrostatic lenses can be varied over almost the full length of the hexapole (50 cm). This flexibility is particularly important for focusing molecules into the synchrotron, as will be discussed in Chapter 5. Here, the two lenses are used to form a tight focus, assuring that all the molecules in the packet are focused into a small area in the detection region. That is, the maximum signal is found when  $\Delta x$  and  $\Delta y$  are minimized.

Figure 3.11 presents the density of decelerated  $\text{ND}_3$  molecules (from 266 m/s down to 85 m/s) in the detection region (36 cm behind the decelerator) as a function of the effective focusing length of the third hexapole for four different effective focusing lengths of the second hexapole. In this experiment, the effective position of each hexapole lens is kept constant. The effective length of the

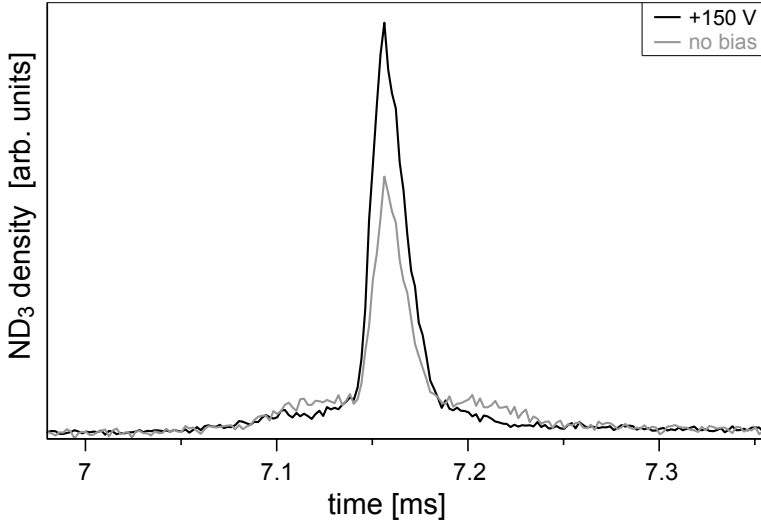


Figure 3.12: The density of decelerated  $\text{ND}_3$  molecules in the detection region measured with (black curve) and without (gray curve) an applied bias voltage as a function of time after release of the gas pulse ( $t_0 = 0$ ).

second hexapole is changed, and in so doing the focal point between the two hexapoles moves; for instance decreasing the length of hexapole 2 moves its focus closer to hexapole 3. It is the task of the third hexapole to (re-)focus the molecules into the detection region. To understand these graphs, one must also consider the buncher, which serves as an aperture in between the hexapoles. The maximum signal is found when the focal position of the second hexapole is near the entrance of the buncher, as shown in trace (b) when using 2.05 mm of the second hexapole and 1.70 mm of the third hexapole. Applying the forces for too long a time interval, as is the case in trace (a), focuses the molecules too far in front of the buncher, resulting in a loss of molecules. Likewise, losses will occur when focusing the molecules too far behind the buncher, as is the case in traces (c) and (d).

The amount of molecules successfully passing through the beamline can be greatly enhanced by applying a constant bias voltage to the electrodes, as shown in Figure 3.12. In a zero field region, the  $|J, KM\rangle = |1, -1\rangle$  and  $|1, 0\rangle$  levels become degenerate (see Figure 2.12), thus molecules could potentially make a transition from one level to the other; this M-changing transition is known as a Majorana transition. Note that the molecules experience no areas of zero field whilst in the decelerator. The zero field regions are after the decelerator in between the focusing elements and the detection zone. The signal peak in the gray trace, measured without a bias voltage, sits atop a pedestal comprised

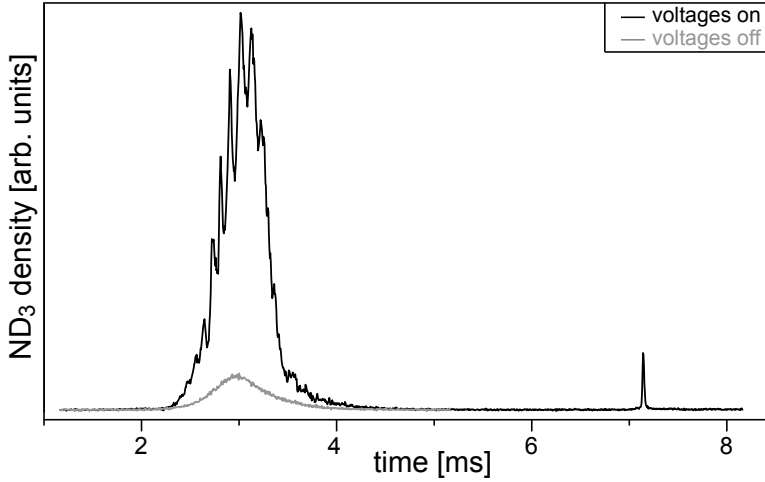


Figure 3.13: Density of  $\text{ND}_3$  molecules, spatially focused using two hexapoles and a buncher, ca. 36 cm behind the decelerator as a function of time after release of the gas pulse ( $t_0 = 0$ ). The gray and black curves show the TOF profiles of the beam with the voltages turned off and on (decelerating molecules from 266 m/s to 85 m/s), respectively. Note that the peak intensity of the decelerated beam is on the same order as that of the original beam (voltages off).

of  $\text{ND}_3$  molecules that have undergone a Majorana transition somewhere after the decelerator, and are thus not properly focused into the detection region. Molecules in the  $|1, 0\rangle$  state are simply not affected by the electric fields, meaning that they are also not deflected from their path, and so can still fly through the detection zone. There, molecules are detected from both the  $|1, 0\rangle$  and  $|1, -1\rangle$  levels. Applying a bias voltage as low as +150 V assures that molecules in the lfs  $|1, -1\rangle$  level remain in some field region (albeit fringe fields at times), and therefore prevents Majorana transitions to the  $|1, 0\rangle$  level. This results in a more effective transfer of the decelerated molecules into the detection zone, where a 35 % increase is observed in the decelerated signal (black).

### 3.4.3 A versatile molecular beam

Combining all the above focusing elements, at their optimum settings, results in a TOF profile of the decelerated beam as shown in Figure 3.13. The Figure shows the TOF profiles of the beam with voltages turned off (gray curve) and with voltages turned on (black curve), with molecules being decelerated in the latter from 266 m/s to 85 m/s. Molecules are detected 36 cm downstream from the decelerator. The structure in the undecelerated part of the beam

with the voltages turned on is real, and has been shown to be reproducible in simulations of similar measurements [82]. In this measurement, the hexapoles and buncher are set such as to transfer the molecules exiting the decelerator into the detection region while keeping the ratio of their phase-space dimensions constant, i.e., a near 1:1 image of the decelerated packet is created at the position of detection. The other two bunches of slow molecules, the leading and trailing packet seen in Figure 3.4 and Figure 3.8, are not observed here; those packets spread out too much over the long free flight to be detected.

Let us turn our attention to the signal ratio of the original and decelerated peaks. Molecules in the original beam (voltages off) expand in three directions until the detection zone. Note that in the case of Figure 3.13 the full distance – from nozzle to detection – is double that as in Figure 3.8. The  $\text{ND}_3$  density of the original beam should decrease proportionally with the flight distance cubed. Thus a ratio of 1:8 between the peak intensities of the original and decelerated beam is expected in Figure 3.13. However, the peak intensity of the original beam is observed to be on the same order as that of the decelerated beam signal – this is the same ratio that was observed when the molecules flew only half the distance in Figure 3.8. At first this might sound disheartening that the decelerator signal is so ‘small’, but let us consider the transverse velocity spreads of the two beams. For the original beam, the transverse velocity is about 0.4 m/s. Assuming an average beam velocity of 285 m/s, the beam spread of the original beam is only 0.1%. The decelerated beam, on the other hand, has a fairly large relative transverse velocity of 5 m/s. For the decelerated beam travelling at 85 m/s, the transverse velocity spread is about 6%. Despite this large difference between the beams’ transverse velocity spreads, the peak intensities for both beams are equal, which is due to the focusing elements on the decelerated beam. In fact, this peak intensity ratio could even be improved upon if losses were reduced; losses arise from (i) the anharmonicities of the restoring focusing forces, (ii) the limited acceptance of the focusing elements, and (iii) the limited acceptance of the ring in which the detection takes place (more details on the acceptance of the ring will be given in later chapters). From Figure 3.13 one can conclude that these three effects combine to form a  $8\times$  decrease in decelerated signal; this is coincidentally the same factor by which the original beam signal decreases over the expansion until the detection zone.

In Figure 3.14, the density of  $\text{ND}_3$  molecules is shown in the detection region, 36 cm behind the decelerator, as a function of velocity (solid black line). The forward velocity of the ammonia beam is continuously scanned in steps of 1 m/s over the 55-130 m/s range. This tuning is accomplished here by selecting a different initial velocity in the 257-283 m/s range, i.e, by changing the time-delay between the triggering of the pulsed valve and the switching on of the Stark decelerator. The Stark decelerator is operated at the same phase-angle of  $70^\circ$  throughout these measurements. For each velocity, the settings of the hexapoles and the buncher ( $n = 3$ ) are adjusted such as to create a

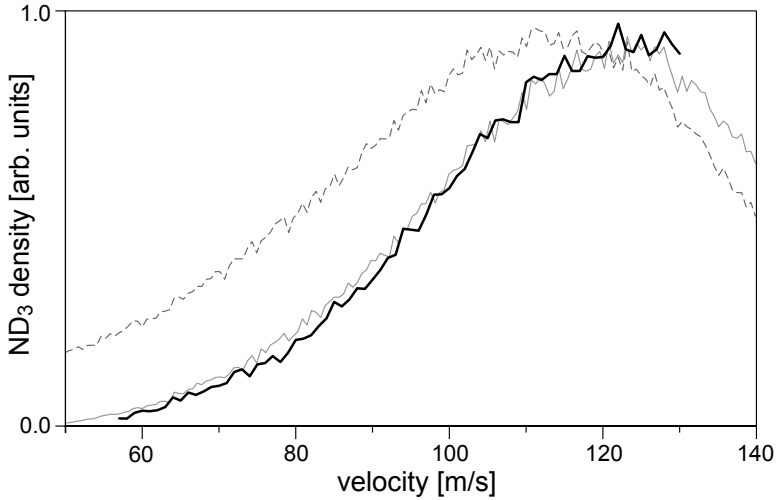


Figure 3.14: The black curve shows the measured density of  $\text{ND}_3$  molecules (36 cm behind the decelerator) as a function of velocity. Each data point represents a new packet that is decelerated and focused into the detection region using the appropriate time sequence, subsequent time sequences are loaded at a 10 Hz rate. The gray solid curve shows the results of a trajectory calculation of the experiment. The gray dashed curve also shows the results of a trajectory calculation, however in this case the apertures of the focusing elements are assumed to be infinitely large.

3D-spatial focus in the detection region. Note that in this way, the length of the decelerated beam in the detection region is always the same (about 2 mm). The data points shown in Figure 3.14 are averaged over 64 shots. For each new velocity, a new time-sequence - with the pre-calculated optimum timings for the decelerator, hexapoles, and buncher - is loaded at a 10 Hz rate. The total time it takes to perform the velocity scan, as shown in the Figure, is therefore less than thirty minutes.

Note that if the decelerator were long enough, such that the maximum of the velocity distribution could be decelerated, and the apertures of the focusing elements would be sufficiently large, one would expect the same signal for every velocity. The drop in signal seen in the Figure is caused by the lower number of molecules at the initial velocity and the finite apertures in the beamline. To illustrate this, trajectory simulations for the system were performed, as shown by the gray curves in Figure 3.14. The simulations are very sensitive to the input values of the average velocity and the initial velocity distribution of the gas pulse. These values are not well known; for matching the simulations to the experiment, values for the average velocity and the velocity spread were

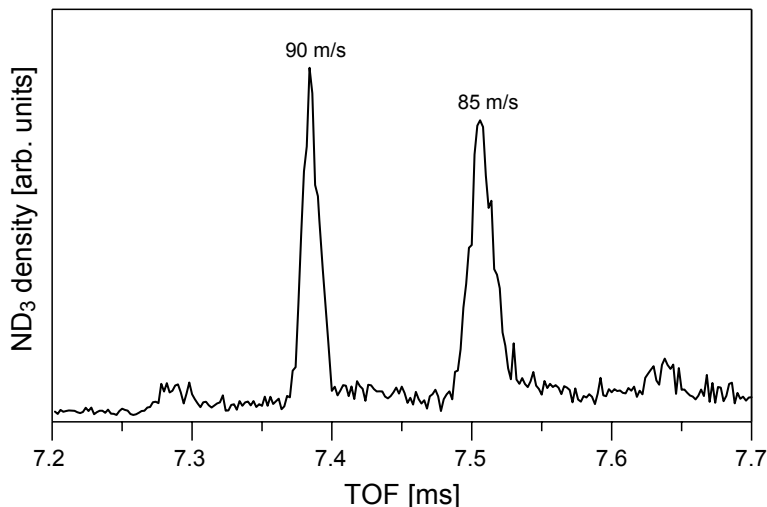


Figure 3.15: Density of  $\text{ND}_3$  molecules 36 cm behind the decelerator as a function of time after release of the gas pulse. Two 3D-spatially focused packets of molecules with forward velocities as indicated are observed. The length of each packet is about 2 mm, the separation between the packets is about 11 mm.

assumed to be 277 m/s and 26 m/s, respectively\*. With these input values, the solid gray curve reproduces the measurement, including the observed sharp reduction in signal for lower final velocities. The dashed gray curve follows from the same trajectory simulation program when the apertures of the hexapoles and buncher are set to infinity.

To give yet another example of the possibilities of this compact beamline, I demonstrate in Figure 3.15 the production and simultaneous 3D-spatial focusing of two packets of ammonia molecules, each with a slightly different forward velocity. The individual packets arrive in the detection region about  $125 \mu\text{s}$  apart. The packets originate from the same gas pulse, and are created by purposely loading two “buckets” of the decelerator simultaneously, as explained in the discussion of Figure 3.4 and Figure 3.8. The first of these two “buckets” is loaded with molecules with an initial velocity of 266 m/s, which are decelerated to a final velocity of 85 m/s. The trailing “bucket” is filled with molecules that entered the decelerator one period later, with a reduced initial velocity of 262 m/s. These molecules are also decelerated to 85 m/s, but already reach this velocity when they are still one period away from the end of the decelerator. As the leading packet is already at the exit of the decelerator

\*Note that these values refer to the velocity spread and average velocity at one moment during the expansion, rather than the velocity spread and average velocity averaged over the full gas pulse that was discussed earlier.



at this time, the electric fields in the last period of the decelerator can be used to selectively change the velocity of the trailing packet without affecting the leading packet. In this experiment, the electric fields have been applied such that the trailing packet is accelerated to a final velocity of 90 m/s. At this velocity, the trailing packet catches up with the leading packet at the center of the buncher. The two decelerated packets are then longitudinally focused simultaneously. Similarly, the hexapoles on either side of the buncher focus both packets transversally. In the detection region, the faster molecules, i.e., the ones that exited the decelerator last, arrive first. As the buncher is positioned almost half-way between the decelerator and the detection point, the 3D-spatially focused packets of molecules are again separated by about 11 mm in the detection region.

### 3.5 Conclusions and outlook

In this chapter, I have presented the compact Stark-decelerator beamline machine for the production of 3D-spatially focused beams of polar molecules with a tunable velocity, and with a tailored velocity distribution. In the experiments presented here, the velocity of the beam of state-selected ND<sub>3</sub> molecules has been varied in the 130-55 m/s range – that is a kinetic energy range of 14-2.5 cm<sup>-1</sup>. By using different seed gases and/or by setting the pulsed valve at different temperatures, the full 0-2000 m/s range can be covered with this beam machine. The laboratory velocity of a Stark decelerated beam is known to a very high precision, as it is only determined by the mechanical precision of the decelerator and by the accuracy of the timings of the high voltage switches; the experimental accuracy of the velocity of the synchronous molecule is better than 10<sup>-3</sup>. The width of the velocity distribution of the decelerated beam is determined by the phase-angle of the decelerator, and whether or not additional velocity focusing is applied, and is typically between 1-10 m/s. Together, this implies that this beam machine can be used for state-to-state scattering experiments with ammonia, for instance, covering the 0-400 meV range with an energy resolution that scales linearly with velocity, but that even at 400 meV is about 1 meV. Additionally, this beamline is optimal for use as an injection line for a synchrotron, which is the main topic of this thesis.



# Chapter 4

## Transverse stability in a sectional storage ring

### 4.1 Introduction

In this chapter, the geometry of a sectional storage ring\* for neutral molecules, consisting of two hexapole focusers bent into semi-circles, is detailed. The transverse trap for the molecules that results from the interaction between the electrostatic confinement forces and the additional centrifugal force experienced along a curved path is described. Molecules are injected tangentially into the ring via the beamline discussed in Chapter 3, and then stored for several round trips. Implementing a segmented hexapole ring allows for independent control over each section of the ring, a feature that I use here to demonstrate the loading of multiple packets into the ring.

### 4.2 Principles of confining neutral molecules in a two-piece hexapole ring

Figure 4.1 shows a cross-section slice through the hexapole ring. The ring radius,  $R_{\text{ring}}$ , is 125 mm and the inner radius of the hexapole,  $R_{\text{hex}}$ , is 4 mm. The radius of the rods is half the inner hexapole radius (2 mm); this geometry approximates the ideal hexapole following the suggestions by Reuss [65]. When  $R_{\text{hex}} \ll R_{\text{ring}}$ , the electric field will be only slightly distorted as compared to a linear hexapole [5]. The position of the molecules is given with respect to the

---

\*I use the nomenclature of *sectional storage ring* in this chapter, as no switching is performed inside the ring with respect to the moving molecules. Upon the inclusion of (phase-stable) longitudinal focusing forces, which is the subject of Chapter 5, the ring will be referred to as a *molecular synchrotron*.

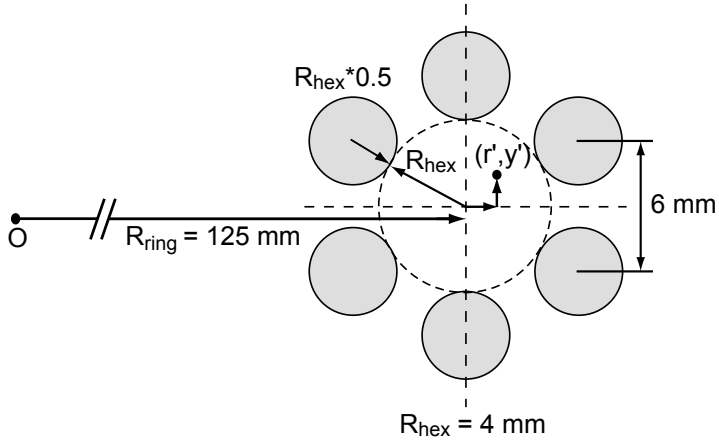


Figure 4.1: *Cross-section of a hexapole storage ring.*

center of the hexapole by the radial coordinate  $r'$  and the vertical coordinate  $y'$ . The tangential coordinate,  $\phi$ , points into the plane of the page. The coordinates with a prime indicate the system rotating with an angular frequency  $\Omega$  around the origin located at a distance  $R_{\text{ring}}$  away.

In a curved hexapole, the Stark interaction with the electric field needs to provide the appropriate centripetal force to keep the molecules on a curved path – much like in the case of a cyclotron, where the magnetic field is needed to provide the centripetal force (2.2). The electrostatic force on the molecules points radially inwards. The centrifugal force that the molecules additionally experience in a ring points outwards along the  $r'$ -axis. The molecules are located at the radial position where the sum of the electrostatic (centripetal) and centrifugal forces is zero. This can be expressed as

$$\frac{kr'}{\sqrt{1 + \left(\frac{W_{\text{inv}}}{kr'^2}\right)^2}} = \frac{mv_\phi^2}{R_{\text{ring}} + r'}, \quad (4.1)$$

where  $m$  is the mass of the molecule,  $v_\phi$  is the velocity of the molecule in the lab-frame, and  $k$  is given by Equation 2.16. Equation 4.1 is analogous to the cyclotron equation (Equation 2.1). Note that in the vertical ( $y$ -)direction, the molecules are located at the position where the sum of the electrostatic and the gravitational forces is zero; the effect of gravity was determined to be negligible [5]. There is no force on the molecules along the tangential direction.

The particular radius where these two forces cancel is known as the *equilibrium radius*,  $r'_{\text{equi}}$ . This implies that molecules with any forward velocity greater than zero will revolve at a radial distance  $R_{\text{ring}} + r'_{\text{equi}}$  (towards the outer rods of the hexapole), with  $r'_{\text{equi}}$  increasing with  $v_\phi$ . Solving for  $r'_{\text{equi}}$  in

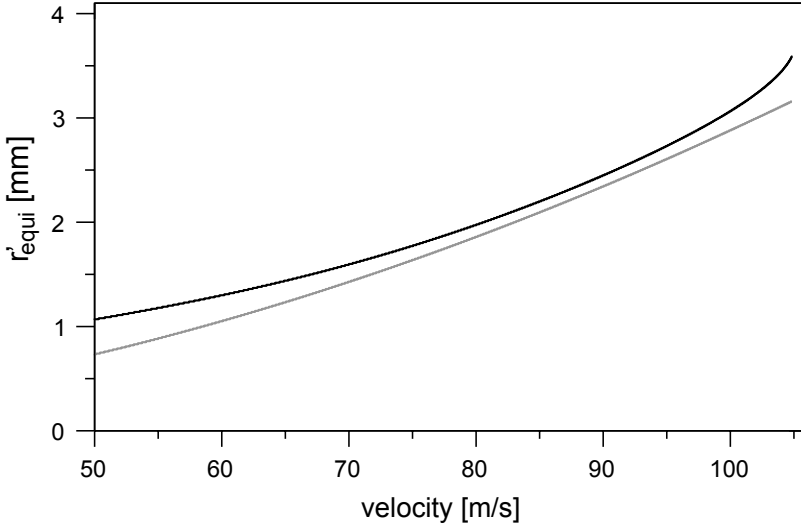


Figure 4.2: The equilibrium radius,  $r'_{\text{equi}}$ , as a function of velocity for the ideal hexapole field (gray) and for the case including the anharmonicities of the field and the inversion splitting of  $\text{ND}_3$  (black).

the ideal (hypothetical) case, i.e., when the inversion splitting is zero and the hexapole force is truly linear, yields

$$r'_{\text{equi}} = \frac{R_{\text{ring}}}{2} \left[ \sqrt{1 + \left( \frac{2v_\phi}{R_{\text{ring}}\omega} \right)^2} - 1 \right] \approx \frac{v_\phi^2}{R_{\text{ring}}\omega^2}, \quad (4.2)$$

where  $\omega$  is expressed by Equation 2.17. The last approximation is valid when  $2v_\phi \ll R_{\text{ring}}\omega$ . Figure 4.2 plots the calculated  $r'_{\text{equi}}$  value as a function of velocity for the ideal case (gray), following from equation 4.2, together with the calculated  $r'_{\text{equi}}$  taking the true hexapole field and the non-zero inversion splitting of  $\text{ND}_3$ ,  $W_{\text{inv}} = 0.053 \text{ cm}^{-1}$ , into account (black). For these calculations, the ring was set at a voltage difference between adjacent rods of 7.7 kV. The  $r'_{\text{equi}}$  varies between 1 mm and 3.5 mm for velocities between 50-105 m/s. For velocities greater than 105 m/s, the  $r'_{\text{equi}}$  approaches the electrodes; molecules at this position will be lost from the ring. Note that around  $v_\phi = 85 \text{ m/s}$ , in the velocity region where most of the experiments have been conducted, the two calculated curves deviate the least. For instance, the  $r'_{\text{equi}}$  in the ideal case for an  $\text{ND}_3$  molecule circulating with a  $v_\phi = 87 \text{ m/s}$  is 2.19 mm. Under these same parameters but including the anharmonicities of the field and  $W_{\text{inv}}$ , the  $r'_{\text{equi}}$  is 2.30 mm. Hence, the linear approximation is generally sufficient for our purposes.

The radial potential well that confines the molecules in a ring is the sum of the Stark energy of ND<sub>3</sub> in the electric field of the hexapole (see Equation 2.13) and the pseudo-potential energy associated with the centrifugal force. The latter can be written as

$$W_{\text{centri}} = - \int \frac{mv_{\phi}^2}{R_{\text{ring}} + r'} dr'. \quad (4.3)$$

Defining the constant of integration as  $W_{\text{centri}}=0$  for  $r' = 0$ , allows for the potential energy of the centrifugal force to be solved as

$$W_{\text{centri}} = -mv_{\phi}^2 \ln \left| 1 + \frac{r'}{R_{\text{ring}}} \right|. \quad (4.4)$$

Thus the resulting potential is

$$W(r') = \frac{1}{2} \frac{kr'^2}{\sqrt{1 + \left(\frac{W_{\text{inv}}}{kr'^2}\right)^2}} - mv_{\phi}^2 \ln \left| 1 + \frac{r'}{R_{\text{ring}}} \right|. \quad (4.5)$$

Figure 4.3 shows the true  $W(r')$  potential (solid curves) at three different velocities, as determined from equation 4.5. For comparison, the perfectly harmonic potential (dotted lines) and the centrifugal potential curve (dashed line) are also plotted in the Figure. The largest deviation between the non-ideal and ideal  $W(r')$ -potentials arises at the edge of the hexapole (near the electrodes); this slightly decreases the trap depth of the non-ideal  $W(r')$  with respect to the ideal case. In part **(a)** of the Figure, where the  $v_{\phi}$  is set to zero, the potential well is deepest and symmetric around  $r' = 0$ ; the centrifugal force is, of course, zero. Figure 4.2 shows that as a molecule's forward velocity is increased, its equilibrium orbit shifts outwards, so long as the ring is kept at a constant voltage difference. This shift is illustrated in part **(b)** of Figure 4.3, where the effective potential well is shown for a molecule moving at  $v_{\phi} = 90$  m/s. Again, the  $W(r')$  is determined by simply adding the same electrostatic potential as in part **(a)** – as that focusing force remains the same – to the centrifugal force at  $v_{\phi} = 90$  m/s for each position along  $r'$ . Note that the difference between the trap's deepest point and its edge has greatly decreased. Continuing to higher forward velocities in turn leads to stronger centrifugal forces; at some point the centrifugal force becomes greater than the electrostatic one, thus rendering the effective  $W(r')$  non-existent. This is depicted in part **(c)** of Figure 4.3, where the same set of potentials is shown for a molecule with a forward velocity of 150 m/s (still assuming the same voltage difference between the ring electrodes). At this velocity, no molecules will be confined. In the calculations shown in Figure 4.3,  $y$  is set to zero.

From Figure 4.3, it is clear that the well becomes less deep for increasing velocities. Assuming a linear force, the maximum radial position a molecule can have and still remain trapped is

$$r = R_{\text{hex}} - r'_{\text{equi}}. \quad (4.6)$$

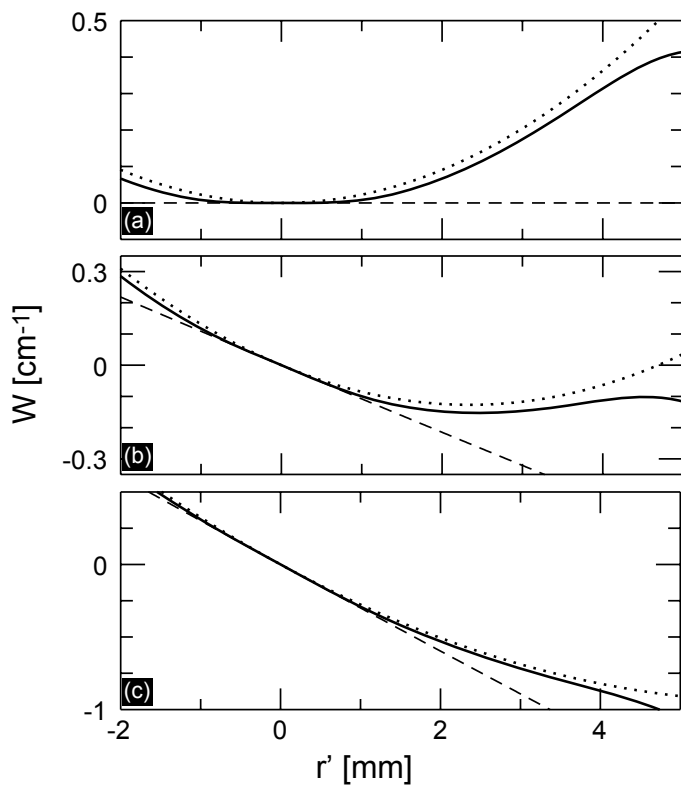


Figure 4.3: The effective potential energy well,  $W(r')$ , is shown for the true hexapole field (solid lines) and the ideal hexapole field (dotted lines) in the radial direction of the ring for  $\text{ND}_3$  molecules moving at three different forward velocities: (a) 0 m/s, (b) 90 m/s, and (c) 150 m/s.  $W(r')$  is determined by the sum of the centrifugal pseudo-potential energy (dashed line) and the Stark energy calculated at  $y=0$ .

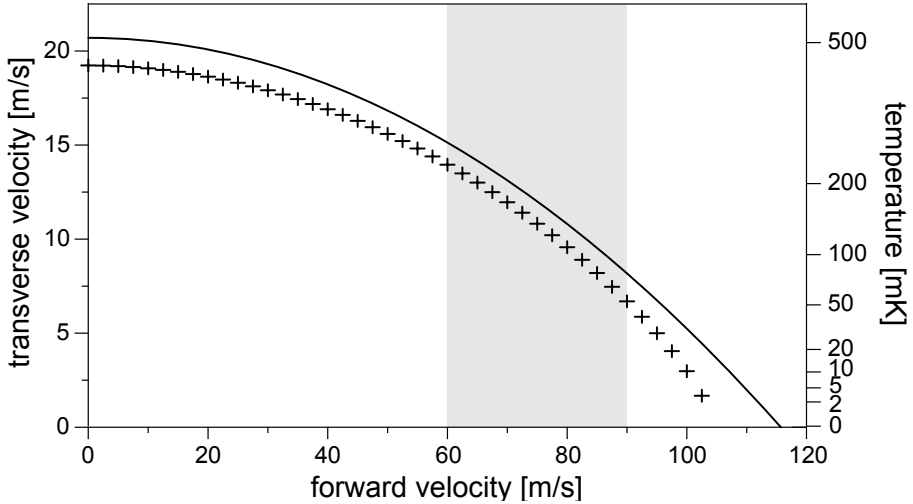


Figure 4.4: The transverse trap depth plotted both in the maximum transverse velocity accepted in the trap – the velocity spread is double this value – and in temperature units as a function of the molecules’s forward velocity. The trap depths are shown for the ideal case (solid line), assuming  $\omega/2\pi = 823$  Hz, and for the true case (crosses). The important range for the experiments performed in this thesis is between 60-90 m/s (gray shaded region).

Hence the maximum transverse velocity a molecule can have and still remain trapped is

$$v_r = \omega r \approx \omega \left( R_{\text{hex}} - \frac{v_\phi^2}{R_{\text{ring}}\omega^2} \right), \quad (4.7)$$

where  $\omega$  is the frequency at which the trapped molecules oscillate in the transverse directions (see Section 2.2.3). The relationship between the maximum transverse velocity and the forward velocity is shown in Figure 4.4 for both the ideal case (black), assuming a  $\omega/2\pi = 823$  Hz, and for the true case (crosses) including the nonlinearities in the potential. The vertical axis on the right plots the trap depth in terms of temperature units. The important velocity range is between 60-90 m/s (shaded gray). The maximum velocity that can be confined at 60 m/s is  $(\pm)15$  m/s, and is half that at 90 m/s with  $(\pm)7.5$  m/s. This corresponds to transverse temperatures of about 200 mK and 50 mK, respectively.

The transverse frequency of the molecules oscillating in the trap is plotted as a function of radial position in the hexapole for the ideal case (gray) and the true case (black) in Figure 4.5. First looking at the ideal case, the  $\omega/2\pi$  remains constant at 823 Hz. Upon including the field nonlinearities, the  $\omega/2\pi$



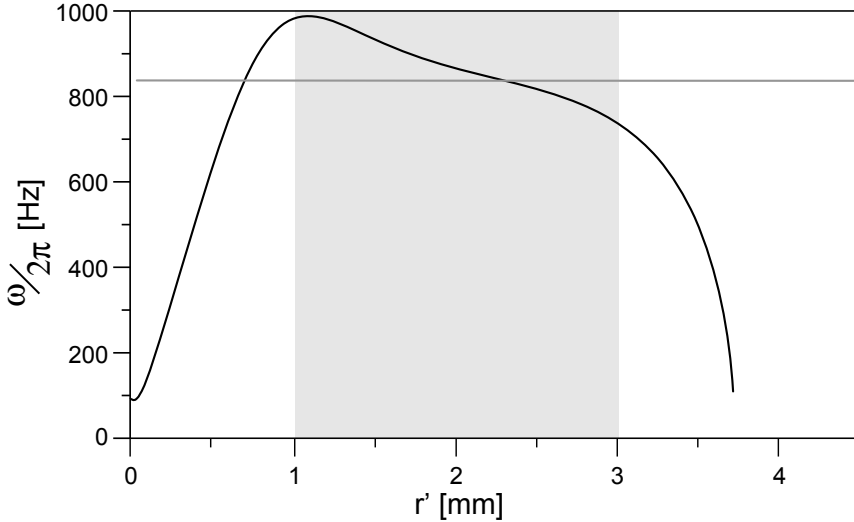


Figure 4.5: *The oscillation frequency in the transverse direction,  $\omega/2\pi$ , as a function of radial position for the ideal case (gray) and for the case including the inversion splitting of  $\text{ND}_3$  (black). Typically,  $\omega/2\pi$  is between 700-1000 Hz under operating conditions (shaded region).*

changes dramatically – varying from 200-1000 Hz. For the velocity range used in the present experiments (shaded gray in the Figure) the range for  $\omega/2\pi$  reduces to between 750-1000 Hz. Note that the slower molecules oscillate at higher frequencies and the faster molecules oscillate at lower frequencies. The large deviation near the center of the hexapole is solely due to the inversion splitting in  $\text{ND}_3$ , whereas the deviation towards the outer edge of the hexapole is a result of the field non-linearities close to the electrodes.

### 4.3 Experimental set-up

The compact molecular beam machine used for the present experiments is the same as described in Chapter 3. Figure 4.6 shows the exact distances between the decelerator focusing components and the ring (in mm). The molecules enter a (pulsed) hexapole some 55 mm downstream from the Stark decelerator and continue to fly 65 mm downstream to the buncher. For these experiments the buncher is set such as to create a velocity focus, i.e., to minimize the packet’s velocity spread. Behind the buncher another (pulsed) hexapole is mounted 21 mm away. Finally, the molecules are injected into the ring 75 mm behind the last hexapole.

The two hexapole half-rings are separated by a 2 mm gap. In confinement

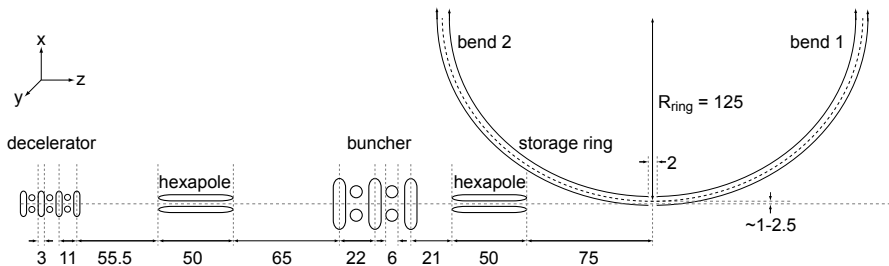


Figure 4.6: *Basic layout of the final elements in the injection beamline and the hexapole storage ring; distances are given in mm.*

operation, (alternating) positive and negative voltages of  $(\pm)5.0$  kV are applied to adjacent rods of the hexapole. Since the molecules revolve at an equilibrium radial position shifted away ( $\sim 2$  mm) from the zero-field region in the center of the hexapole, molecules will not undergo Majorana transitions. The density of molecules in the upper component of the  $|J, K\rangle = |1, -1\rangle$  inversion doublet is probed in the gap of the ring via a  $(2+1)$  resonance-enhanced multi-photon ionization (REMPI) scheme using UV laser light around 317 nm. Immediately prior to firing the laser, the high voltages on the ring are switched off. The residual electric field formed by the bias voltages on the ring electrodes - set to  $-300$  V on the top rods,  $-170$  V on the middle-top rods,  $+170$  V on the middle-bottom rods, and  $+300$  V on the bottom rods - serves to accelerate the parent ions perpendicularly upwards ( $y$ -direction), through a flight tube ( $-1700$  V), to be mass-selectively detected by a multi-channel plate ( $-1900$  V) ion-counter. The ion signal is proportional to the density of the ammonia molecules in the detection region of the ring.

## 4.4 Experimental results and discussion

To demonstrate the performance of the hexapole storage ring, I present measurements of the first six round trips of a packet of ammonia molecules. Figure 4.7 shows the  $\text{ND}_3$  density in the detection zone of the ring as a function of storage time. Here a packet of  $\text{ND}_3$  molecules is decelerated to  $91.8$  m/s and subsequently injected into the ring; at  $t_0 = 0$  the storage ring is switched on. The peaks in the signal correspond to the packet moving through the laser focus in the detection region upon completion of a round trip. In comparing the time-of-flight profile of the six round trips, the packet is seen to broaden upon increasing storage times. The time-integrated signal of the peaks, however, stays fairly constant, as evident in the graph in the upper part of Figure 4.7. This provides further corroboration that the molecules are not lost from the

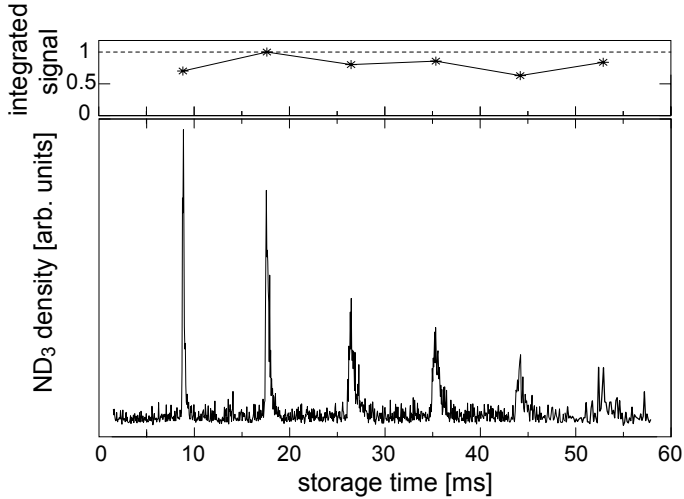


Figure 4.7: The density of ammonia molecules at the detection zone inside the hexapole storage ring is shown as a function of storage time up to the 6<sup>th</sup> round trip. The upper graph shows the time-integrated signal of each round trip. The integrated signal of each peak stays fairly constant over the 6 round trips, i.e. the molecules are not lost from the ring, but only spread out tangentially inside it.

ring but rather spread out.

To determine the packet's round-trip time and position distribution, Gaussian curves were fitted to the individual round-trip peaks in Figure 4.7; the results are shown in Figure 4.8. First, in part (a) the arrival time of the molecules in the detection region is plotted as a function of round-trip number. The theoretical round-trip time calculated for molecules moving with a forward velocity of 91.8 m/s in the hexapole storage ring set at a 10 kV voltage difference across the electrodes is 8.86 ms. A linear fit to the experimental data reveals that the molecules take 8.83 ms to complete one round trip. The small discrepancy can be due to (i) slight deviations in the forward velocity, (ii) slight deviations in the in-coupling  $r'$  position of the packet into the ring, and (iii) a misalignment of the two half rings, which may either increase or decrease the molecules' flight path. For instance, a variation of 0.5 m/s on the absolute value of the forward velocity or of a few millimeters on the total circumference could account for this 0.03 ms difference between the experimental and calculated round-trip times.

Secondly, in part (b) the tangential broadening of the packet is plotted as a function of storage time. The temporal width of the decelerated and velocity focused packet is about 100  $\mu$ s, which is tantamount to a position spread of

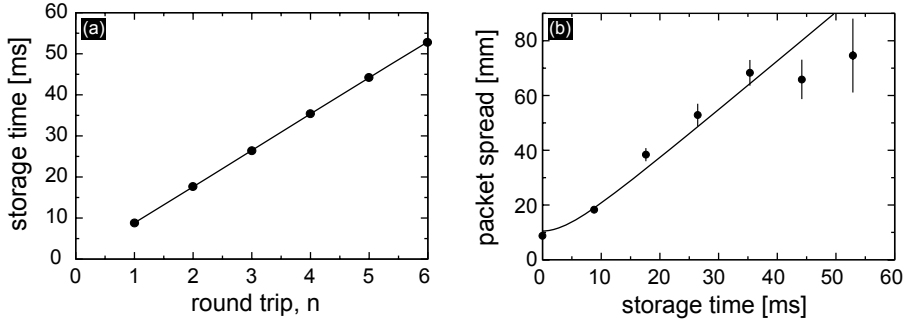


Figure 4.8: Analysis of individual round trips. **(a)** The storage time is plotted as a function of the number of completed round trips,  $n$ . The round-trip flight time can be deduced from a linear fit as  $t_{RT} = 8.83$  ms. **(b)** The position spread of the stored molecules in the detection zone, determined from the TOF profiles shown in Fig. 4.7, is plotted as a function of storage time; error bars are shown where necessary. From Gaussian fits to these profiles, the 1<sup>st</sup> round trip is determined to have a temporal width of  $200 \mu\text{s}$ , corresponding to a position spread of  $18.5$  mm, and for the 6<sup>th</sup> round trip a temporal width of  $815 \mu\text{s}$ , corresponding to a position spread of  $74.8$  mm. The solid line in the graph shows the result from a fit to the data using a simple formula, yielding a  $\Delta z_i$  of  $10.7$  mm and a  $\Delta v_z$  of  $1.8$  m/s.

the packet of  $9$  mm. After only the 1<sup>st</sup> round trip the packet expands to about  $200 \mu\text{s}$ , corresponding to a  $18.5$  mm position spread. As the molecules continue to complete another five round trips, i.e., completing an equivalent free-flight distance of  $4$  m, the width of the packet quadruples to almost  $75$  mm. The broadening is a result of the residual velocity distribution of the stored molecules. Note that molecules moving in free-flight would experience a similar expansion to that observed in the ring, however in the ring the expansion only occurs in one direction ( $z$ ). Note that the expansion occurs slightly slower in the ring structure due to the effects of the faster molecules travelling along a larger circumference and the slower molecules travelling along a smaller circumference, but its effect on the spreading is marginal and can be neglected in the current case [5].

The solid line in Figure 4.8**(b)** shows the result from a fit to the data of Equation 3.11, where  $\Delta z_i$  is the initial longitudinal position spread of the packet and  $t$  is the storage time. From this fit, a  $\Delta z_i$  of  $10.7$  mm and a  $\Delta v_z$  of  $1.8$  m/s is determined. Substituting the  $\Delta v_z$  value into Equation 3.12 a (translational) temperature estimate of the packet is  $1.4$  mK.

There are two main advantages in having a split ring: (i) the inclusion of “bunching” elements into the ring to keep the molecules together along the tangential direction, which is the subject of the next chapter, and (ii) the ca-

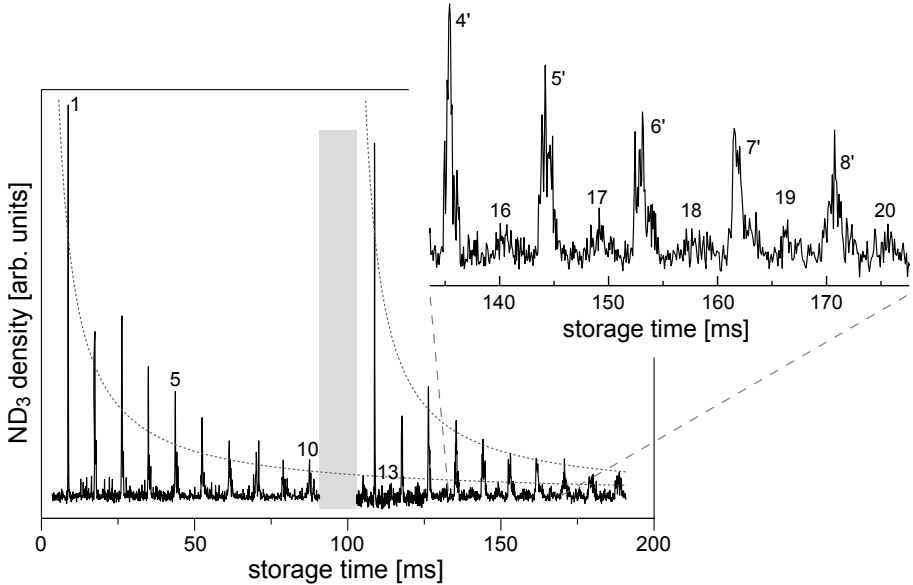


Figure 4.9: *Multiple packets in the hexapole ring. TOF profiles showing two packets of ammonia molecules, each moving at  $v_\phi = 91.8$  m/s, revolving inside the hexapole storage ring; the two dotted lines are  $1/t$  plots to guide the eye. The second packet is injected 100 ms after the first packet, and trails it by ca. 35 cm (almost 1/2 the ring). Prior to injection of the second packet, the detection system is briefly switched off (indicated by the gray bar) to avoid saturation of the detector as the undecelerated part of the ammonia beam passes through the detection region. The inset shows a zoom-in of a TOF profile of the first packet after completing its 16<sup>th</sup> – 20<sup>th</sup> round trips and the second packet after completing its 4<sup>th</sup> – 8<sup>th</sup> round trips.*

pability of injecting multiple packets into the ring without disturbing molecules that are already stored. Storage of multiple packets cannot be accomplished in a non-fragmented ring structure since subsequent packets of IFS molecules would not enter the high-electric field region of the ring when its voltages were turned on. Yet, the momentary switching off of the ring voltages to allow for a second injection would also not work because the already stored molecules would then escape tangentially out of the ring.

To demonstrate multi-loading and storing, I present measurements in Figure 4.9 of two packets of  $\text{ND}_3$  molecules, injected consecutively and stored simultaneously, in the segmented hexapole storage ring as a function of time after the storage ring is switched on ( $t_0 = 0$  for the first injection). The measurements in Figure 4.9 are similar to those in Figure 4.7, but now a second packet is injected 100 ms later. In this case, the second packet trails the first

by 35 cm, i.e., the second packet is roughly a half-ring behind. This distance separation can be inferred from the time between the round trip signal of the two packets in the inset of Figure 4.9. In the Figure, both the first and second packets are seen to spread out; the two dotted lines are  $1/t$  plots to guide the eye. The first packet, moving at a velocity of 92 m/s, completes its 1<sup>st</sup> round trip in 8.8 ms, and has a position spread at this time of 12 mm. After completing its 16<sup>th</sup> round trip, the packet has broadened by an order of magnitude to 118 mm. The second packet also moves at 92 m/s with similar initial dimensions, and thus has the same round-trip time and longitudinal dispersion. The injection and storage of the second packet does not interfere with the first packet although it becomes more difficult to ascertain detection of molecules belonging solely to the first packet. The detection system is not switched on when the undecelerated part of the second ammonia beam passes through the detection region, as indicated by the gray bar, to avoid saturation of the detector.

### 4.5 Conclusions and outlook

In this chapter, I have discussed the transverse properties of a segmented-hexapole storage ring for neutral molecules. I have presented measurements in which two packets of molecules were successfully confined in two dimensions inside the storage ring. Due to the, albeit small, velocity spread of the packet the molecules disperse along the tangential direction of the ring – already by tens of millimeters after completing only a few round trips. The corresponding decrease in density in the ring over an extended storage time is detrimental for future collision studies. Thus, it is critical to apply a longitudinal focusing force on the molecules to keep them together, as will be discussed in the next chapter.

# Chapter 5

## A synchrotron for neutral molecules

### 5.1 Introduction

To date, the few experiments dealing with ring structures for neutral particles have employed cylindrically symmetric schemes [1], [2], [3]. In these rings, the molecules are stably confined in the transverse directions, however, no force is applied to the particles along the longitudinal direction. Thus the stored molecules spread out, as was seen in the previous chapter, and will eventually fill the entire ring. To fully exploit the possibilities offered by a ring structure, it is imperative that the particles remain in a bunch as they revolve around the ring. Confining molecules in the longitudinal direction, however, requires “bunching” forces to be applied to the molecules synchronously with their movement in a circle. That is to say, one needs to upgrade from simply storing the molecules in a ring to actively re-focusing them, in their moving frame, in a synchrotron.

In the two-piece molecular synchrotron demonstrated in this chapter, a packet of deuterated ammonia molecules is focused along the longitudinal direction (“bunched”), as well as decelerated and accelerated, using the fringe fields between the two halves of a segmented hexapole ring. Measurements are presented demonstrating the stability of molecules travelling at 87 m/s in the synchrotron. The stored bunch of cold molecules is confined to a tight packet even after completing 100 round trips, corresponding to a flight distance of over 80 meters. Further investigations into the synchrotron provide details into the longitudinal potential well and the parameters of the synchrotron. Additionally, the successful injection and bunching of multiple packets of molecules in

---

Adapted from:  
C. E. Heiner, D. Carty, G. Meijer, and H. L. Bethlem, *Nature Physics* **3**, 115 (2007).

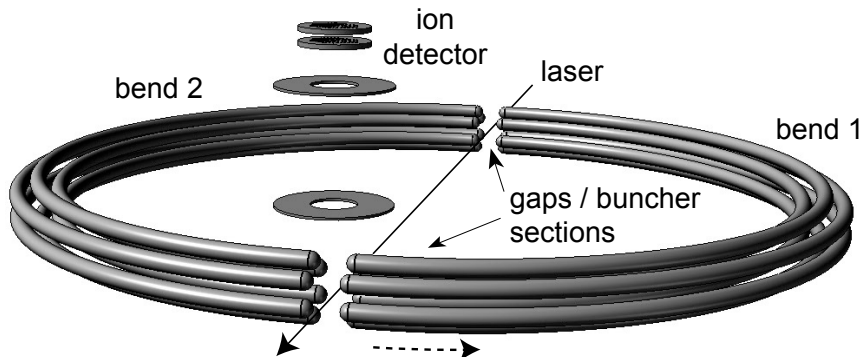


Figure 5.1: *Experimental set-up.*  $\text{ND}_3$  molecules are decelerated to a forward velocity of 87 m/s (kinetic energy of  $6.33 \text{ cm}^{-1}$ ) and are then tangentially injected into bend 1 of the synchrotron. The hexapole ring radius is 125 mm with two 2 mm gaps between the two halves; the electrodes each have a radius of 2 mm and are placed around a circle with a radius of  $R_{\text{hex}} = 4 \text{ mm}$ . Molecules in the detection region are ionized using (2+1)-resonance enhanced multi-photon ionization (REMPI) with pulsed laser light around 317 nm, and are then extracted perpendicularly to the plane of the ring and counted by an ion detector.

the synchrotron is reported.

## 5.2 Design of a two-piece synchrotron for neutral molecules

Our synchrotron is depicted in Figure 5.1 and pictured in Figure 5.2. The synchrotron is formed by two hexapoles, bent into a semi-circle with  $R_{\text{ring}} = 125 \text{ mm}$ , that are separated by a 2 mm gap. The electrodes have a 4 mm diameter, and are positioned symmetrically on the outside of a circle with a radius,  $R_{\text{hex}}$ , of 4 mm. The electrodes were machined such that they have smooth ‘endcaps’, thus there is a linear section of 2 mm before and after the gap. On that account, the molecules fly through a 6 mm long straight section, very subtly altering the geometry from a circle to a slightly oval ‘race-track’.

As the molecules revolve around the ring in the direction indicated by the dashed arrow, the voltages applied to the electrodes are switched between the four configurations shown in Figure 5.3(a)-(d). As discussed in the previous chapter, the configuration in Figure 5.3(a), where the voltages are applied such



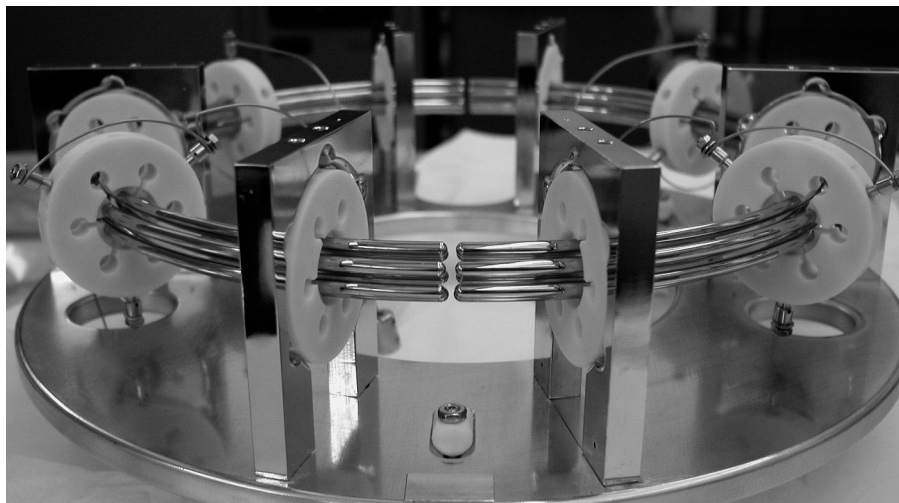


Figure 5.2: Photograph of the molecular synchrotron. The electrodes are held in place by ceramics, which are fixed with respect to the baseplate via aluminum housings. The 2 mm gap separating the two half-rings is in the center of the photograph.

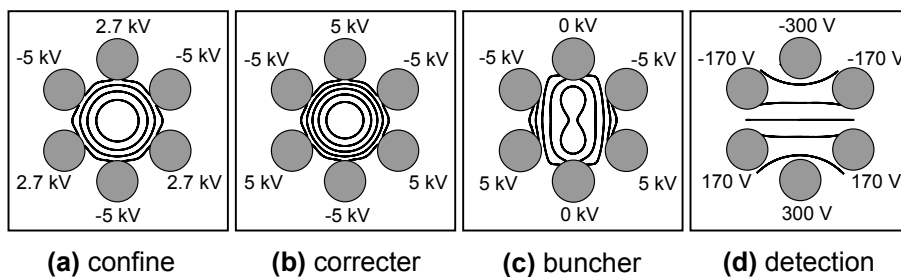


Figure 5.3: The four voltage configurations necessary for (a) confinement, (b) performing transverse (stability) correction, (c) acceleration/deceleration and bunching, and (d) extracting laser-ionized molecules are shown. The contours represent the absolute electric field in steps of 8 kV/cm for (a), (b), and (c), and the electrostatic potential is steps of 100 V for (d).

as to create a zero electric field in the hexapole center and a linearly increasing field radially outwards, provides the two-dimensional confinement force on lfs molecules. In the gap regions, the molecules can be bunched (and accelerated/decelerated) by applying the voltages shown in Figure 5.3(c) to one bend, while the other bend is kept at a ground potential, in the manner that will be further discussed below. Note that the molecules are not transversely confined during the bunching process, thus they spread out in the two transverse directions during bunching. To offset this effect, the focusing force is increased by 30% during a short period of time before and after the molecules pass through the gap, by switching to the corrector configuration shown in Figure 5.1(b); further details of the stability of the transverse motion of the molecules due to the gaps and the influence of the corrector will be presented in Chapter 6. For detection, the stored molecules are ionized and extracted perpendicularly to the plane of the ring, using the configuration shown in Figure 5.1(d), and then counted by an ion detector, as shown in the schematic in Figure 5.1.

### 5.2.1 Bunching neutral molecules in a synchrotron

This section describes the basic principles for implementing longitudinal (bunching) forces in the synchrotron. Figure 5.4 depicts the buncher scheme. As molecules enter the gap from left to right, the voltages in bend 1 are turned off and the voltages in bend 2 are turned on to a bunching configuration. This results in the smooth field gradient, which causes molecules in the  $|J, KM\rangle = |1, -1\rangle$  state to gain Stark energy and consequently lose kinetic energy, i.e., the molecules are decelerated while they move into the gap. The Stark energy, or potential energy, in this configuration is denoted by  $W_1$  in Figure 5.4. As the molecules exit the gap, however, the voltages in bend 2 are turned off and the voltages in bend 1 are turned on to a bunching configuration. This creates the opposing field gradient, which causes lfs molecules to lose Stark energy and thus gain kinetic energy, i.e., the molecules are accelerated as they move out of the gap. The potential energy in this configuration is denoted by  $W_2$ . The difference between  $W_1$  and  $W_2$ ,  $\Delta W$ , provides the restoring force in the longitudinal direction.

The time to switch between these two potentials is defined with respect to the position (and velocity) of the aforementioned synchronous molecule. This molecule is always at the same position in the gap when the fields are switched,  $z'$ . In Figure 5.4, the buncher fields are switched after the synchronous molecule has passed the center of the gap,  $z_0$ , resulting in it spending more time on the decelerating slope of  $W_1$  than on the accelerating slope of  $W_2$ , as marked in bold in part (a) of the Figure. This leads to a net deceleration force on the synchronous molecule. As all the molecules are focused towards the synchronous molecule, decelerating it imposes the same velocity change over the entire molecular packet. Likewise, if the buncher fields are switched before the synchronous molecule has reached the center of the gap, it will spend more time

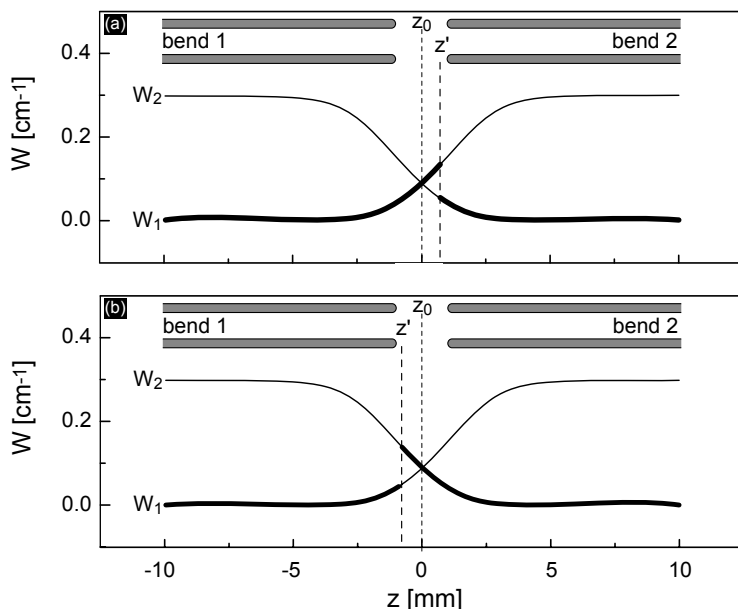


Figure 5.4: Principle idea for stably **(a)** decelerating or **(b)** accelerating molecules in the gaps of the ring. The potential energy curves  $W_1$  and  $W_2$ , which a molecule flying at  $r_0$  experiences in the vicinity of a gap, are plotted as a function of the  $z$  position. The center of the gap,  $z_0$ , is denoted by the dotted line. The  $z$ -position,  $z'$ , at which the synchronous molecule is located when the fields are switched is denoted by a dashed line; the bold sections denote the parts of the potential curves that are exploited for either deceleration or acceleration.

on the accelerating slope than on the decelerating slope, as marked in bold in part **(b)** of the Figure, thus accelerating the entire molecular packet.

It follows that simply bunching the molecules, that is re-focusing the molecules without altering their forward velocities, only occurs in the case that the fields are switched at  $z'=z_0$ , i.e., where  $\Delta W = 0$ . Operating the ring in this way is referred to as *normal operation*. This point is illustrated in Figure 5.5, in which the potential energy curves  $W_1$  and  $W_2$  and the resulting  $\Delta W$  curves are plotted. Looking at the  $\Delta W$  curve, the only position at which the energy difference is zero is at  $z_0$  – the position of the synchronous molecule under normal operation. The synchronous molecule will, therefore, lose and gain the same amount of kinetic energy per round trip. It follows that molecules in front of the synchronous molecule will lose more kinetic energy, and vice versa, molecules that are behind the synchronous molecule will gain more kinetic en-

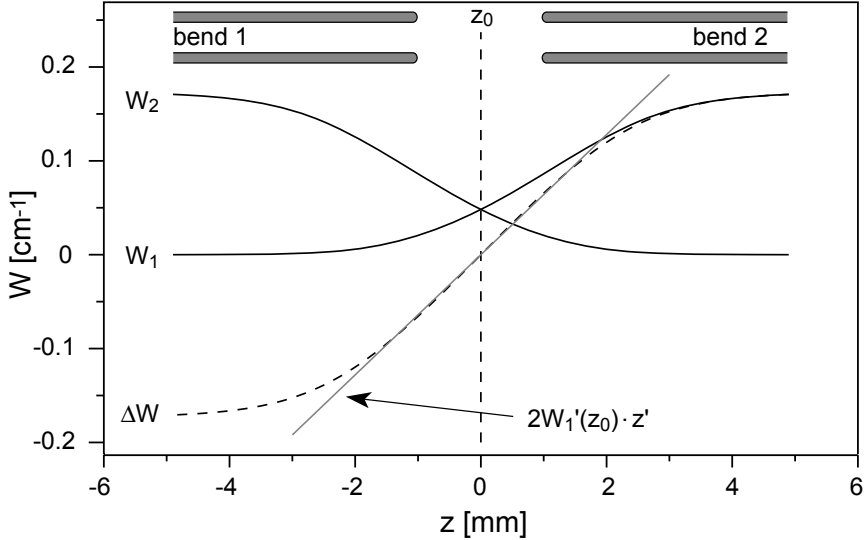


Figure 5.5: Principle idea for bunching molecules using the fringe fields in the gaps. The potential energy curves  $W_1$  and  $W_2$ , which a molecule flying at  $r_0$  experiences in the vicinity of a gap, are plotted as a function of the  $z$  position. The center of the gap is denoted by  $z_0$ ; when the synchronous molecule is located at this position the fields are switched. Additionally the potential energy difference,  $\Delta W$  is shown. A linear fit to the  $\Delta W$  curve yields a slope,  $2W_1'(z_0)$ , of  $0.065 \text{ cm}^{-1}/\text{mm}$  and approximates the linear restoring force. Adapted from Cromptoets et al. (with permission) [5].

ergy with respect to the synchronous molecule. Due to the mirror symmetry of the two potentials,  $W_1(z_0 - \Delta z) = W_2(z_0 + \Delta z)$ , thus allowing the difference between the two curves to be written as

$$\Delta W = W_1(z + \Delta z) - W_1(z - \Delta z) = 2 \frac{\partial W_1}{\partial z} \Big|_{z=z_0} \Delta z = 2W_1'(z_0) \Delta z. \quad (5.1)$$

I can introduce an average force\*,  $\langle F \rangle$ , which encompasses the force over one

---

\*The notion of an average longitudinal force is only useful in the case when  $\frac{L}{v_\phi} \ll \frac{1}{\omega_{\text{syn}}}$ , i.e., that the molecules pass many gaps (bunchers) before completing one longitudinal oscillation. This condition is not strictly fulfilled in our case as the molecules pass only four gaps before completing an oscillation. This implies that the shape of the packet in phase-space changes as a function of the position in the ring; it is larger at the gaps and smaller at the quarter-ring positions. Note that for molecules moving slower than 50 m/s the model breaks down completely, and the buncher is no longer stable.

section of the ring with a length  $L$  over one gap and one bend, around  $z_0$  to be

$$\langle F \rangle = -\frac{2W'_1(z_0) \cdot \Delta z}{L}; \quad (5.2)$$

if  $\Delta z$  is small. The  $\langle F \rangle$  force is a linear restoring force, with an angular frequency,  $\omega_{\text{syn}}$ , that can be expressed by

$$\omega_{\text{syn}} = \sqrt{\frac{2W'_1(z_0)}{mL}}. \quad (5.3)$$

The value found for  $2W'_1(z_0)$  from the linear fit of  $\Delta W$  in Figure 5.5, through  $z = 0$ , is  $0.065 \text{ cm}^{-1}/\text{mm}$  for  $\text{ND}_3$ , yielding an  $\omega_{\text{syn}}/2\pi = 46 \text{ Hz}$ . Taking the harmonic (linear) part of the buncher fields into consideration ( $\Delta v = \omega_{\text{syn}}\Delta z$ ), molecules within a position interval of  $\Delta z = \pm 2.5 \text{ mm}$  and a velocity interval of  $\Delta v_z = \pm 0.5 \text{ m/s}$  will experience a linear restoring force towards the synchronous molecule and oscillate around it. Thus the molecules are trapped in a travelling potential well that revolves around the ring. Operating the synchrotron in normal mode, the acceptance of the longitudinal well is given by

$$\text{Area}|_{z'_s=z_0} = \pi \cdot \omega_{\text{syn}} \cdot z_{\text{max}}^2, \quad (5.4)$$

where  $z_{\text{max}}$  is the maximum distance at which a molecule can be away from  $z_0$  and still be bunched; in the current set-up  $z_{\text{max}} = \pm 2.5 \text{ mm}$ .

Note that for decelerating molecules in Figure 5.4(a), the position at which the buncher fields are switched shifts towards positive  $z$ -values, i.e., the molecules that are stably decelerated are actually those that are further ahead. Similarly for accelerating molecules, the position at which the buncher fields are switched shifts towards negative  $z$ -values, i.e., the molecules that are stably accelerated are those that are further behind. Moreover, the amount of molecules trapped inside the longitudinal potential well is  $z$ -position dependent. Although the synchrotron is more often operated in normal mode, it is useful to look at the phase-space area of the packet if the molecules are accelerated or decelerated (i.e., negatively accelerated) in the gaps – this provides insight into the shape of the longitudinal potential well at the edges. The longitudinal acceleration is

$$a_s = -\omega_{\text{syn}}^2 z'_s. \quad (5.5)$$

The acceptance is smaller than that for normally bunched molecules by  $(z_{\text{max}} - |z'|)$ , thus reducing the entire phase-space area to

$$\text{Area}|_{z'_s \neq z_0} = \pi \cdot \omega_{\text{syn}} \left( z_{\text{max}} - \left| \frac{a_s}{\omega_{\text{syn}}^2} \right| \right)^2. \quad (5.6)$$

The density of molecules will linearly decrease when  $\Delta z$  decreases and  $\omega_{\text{syn}}$  stays constant, since the number of trapped molecules scales as  $\Delta z \cdot \Delta v_z -$

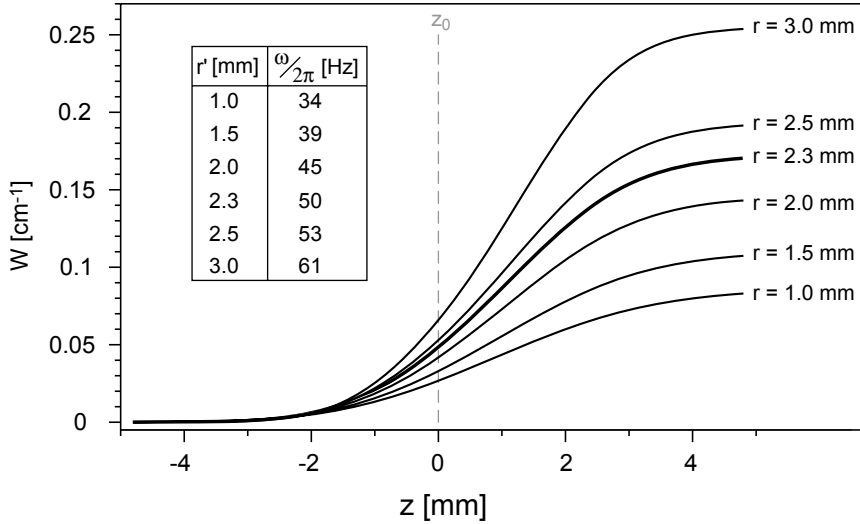


Figure 5.6: Radial dependence of the buncher potential energy curve  $W_1$  as a function of  $z$ -position. The curves are shown for  $r' = 1.0, 1.5, 2.0, 2.3$  (equilibrium radius for 87 m/s), 2.5, and 3.0 mm. The center of the gap is denoted by  $z_0$  (dashed line). The inset lists the angular frequencies for the different radii. Adapted from Crompvoets et al. [5].

which is equal to  $\Delta z^2 \cdot \omega_{\text{syn}}$ . Similarly the density of molecules will also decrease if the trap becomes more shallow, i.e.,  $\Delta v_z$  decreases and  $\Delta z$  stays constant.

Considerations as to the radial position of the molecules must also be taken into account. Looking at the buncher configuration in Figure 5.3c, it is clear that the electric field is not homogeneous along the radial direction. Thus the restoring buncher force that the molecules experience is radial dependent;  $W_1$  curves for various radii are presented in Figure 5.6. The effect of this radial dependence is that the molecules experience a small force towards the center of the synchrotron as the electric field increases radially outwards. The radial dependence causes a coupling between the longitudinal and transverse motions of the molecules. However, due to the large difference in frequency between the synchrotron and betatron oscillations, the coupling is expected to be weak. For instance, inserting  $W_1'(z_0)$  listed in the inset table for a molecule moving at 87 m/s located at  $r = 2.3$  mm ( $r_{\text{equi}}$ ) into equation 5.3, gives a synchrotron oscillation frequency of around 50 Hz, whereas the betatron oscillation frequency is predicted to be on the order of 1 kHz.

## 5.3 Experimental set-up

The compact molecular beam machine used in the present experiments for decelerating a packet of  $\text{ND}_3$  molecules to 87 m/s and subsequently injecting it into the synchrotron is implemented as described in Chapter 3. The timings are determined by a home-built program. The pulses along the beamline are executed by a four-channel digital delay/pulse generator (Stanford Research Systems, Inc., DG535) and forwarded to the switches via two VME burst units and a logic unit that were built at the Fritz-Haber-Institut Electronics Workshop. The  $\text{ND}_3$  molecules are detected at the injection point in the synchrotron using (2+1)-resonance enhanced multi-photon ionization (REMPI) with pulsed laser light around 317 nm. The ring usually runs at a 10 Hz repetition rate, however for measurements with storage times exceeding 100 ms, the repetition rate of the beamline - which includes the nozzle firing and one decelerator pulse train - is reduced to between 1-5 Hz via the digital delay generator. The repetition rate for detection is also decreased to 1-5 Hz by placing a mechanical shutter before the entrance of the chamber to block the laser light; the laser system is always operated at a 10 Hz repetition rate.

### Switching between ring voltage configurations

In Figure 5.7, a pulse sequence for one round trip (not including detection) is shown. The scheme on top illustrates when each configuration – confinement, correcter, and buncher (see Figure 5.3) – are applied to each bend. Independent switching of the half rings allows for, e.g., voltages on bend 2 to be set to ground while voltages on bend 1 are set to confinement. Bunching the molecules requires two consecutive pulses, as indicated. It is important to apply the buncher voltages for a short time, since the molecules experience no transversal focusing forces during bunching; however, if the forces are applied for too short a time the longitudinal forces will not be as effective. A good compromise value was determined experimentally to be 98  $\mu\text{s}$ , which corresponds to a length of 8.5 mm for molecules moving at 87 m/s. Furthermore, the increase in electric field strength between the confinement and the correcter configuration is clearly depicted. The correcter configuration was applied for 170  $\mu\text{s}$  before and after the gaps, i.e., a total of 340  $\mu\text{s}$  (see Section 6.4.2).

The scheme in the middle of Figure 5.7 details the voltages applied to the individual rods in each bend to form the corresponding configurations. Four independent switching schemes are applied to the six hexapole electrodes, which are labelled  $T$  for the top rod,  $MT$  for the two middle top rods,  $MB$  for the two middle bottom rods, and  $Bot$  for the bottom rod – the middle top and middle bottom rods are electronically connected *in situ*. The voltage configurations are labelled along the top:  $C$  represents confinement,  $B$  represents the buncher, and  $K$  represents the correcter; the numbers 1 and 2 denote bend 1 and bend 2, respectively. Note that the correcter is applied simultaneously

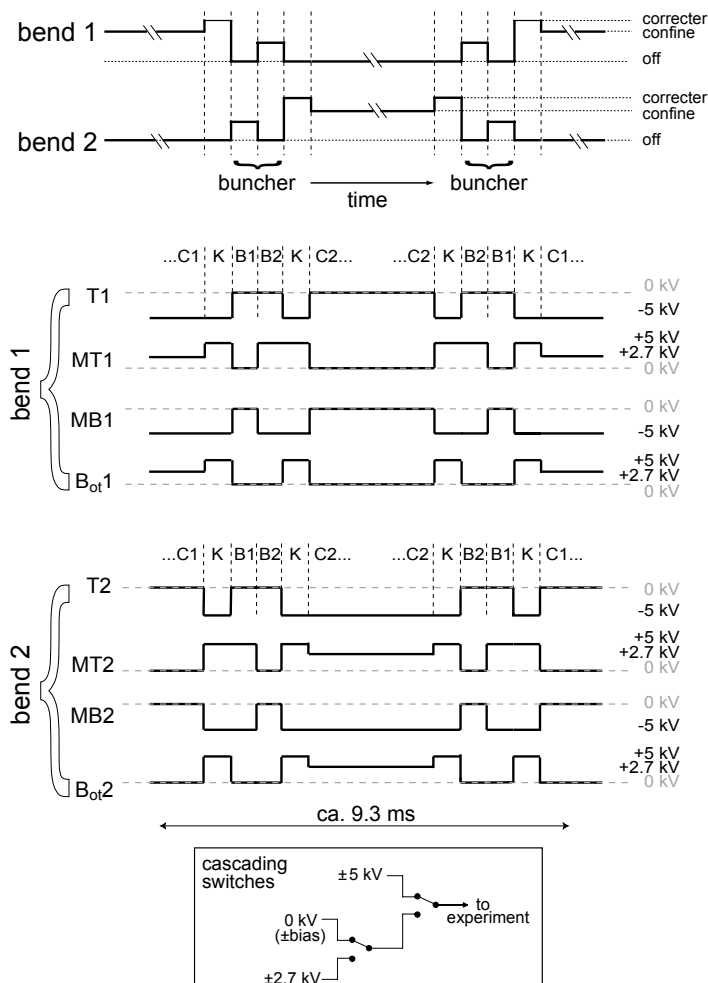


Figure 5.7: Switching sequence for molecules completing one round trip (without detection) in the ring, starting from the dashed arrow indicated in Figure 5.1. The upper scheme shows the general configurations – confinement, correcter, and buncher – applied to each bend for a round trip. The middle scheme shows the voltages applied to the individual rods in bend 1 or bend 2. Four independent switching schemes are applied to each hexapole half-ring – for the top rod ( $T$ ), the two middle top rods ( $MT$ ), the two middle bottom rods ( $MB$ ), and the bottom rod ( $B_{ot}$ ). The configurations are labelled  $C1/C2$  for confinement,  $B1/B2$  for the buncher, and  $K$  for the correcter (always applied to both bends). The voltages on the  $T$  and  $MB$  electrodes are switched 645 times per second, and the voltages on the  $B_{ot}$  and  $MT$  electrodes are switched 860 times per second. The inset box shows the cascading switches.



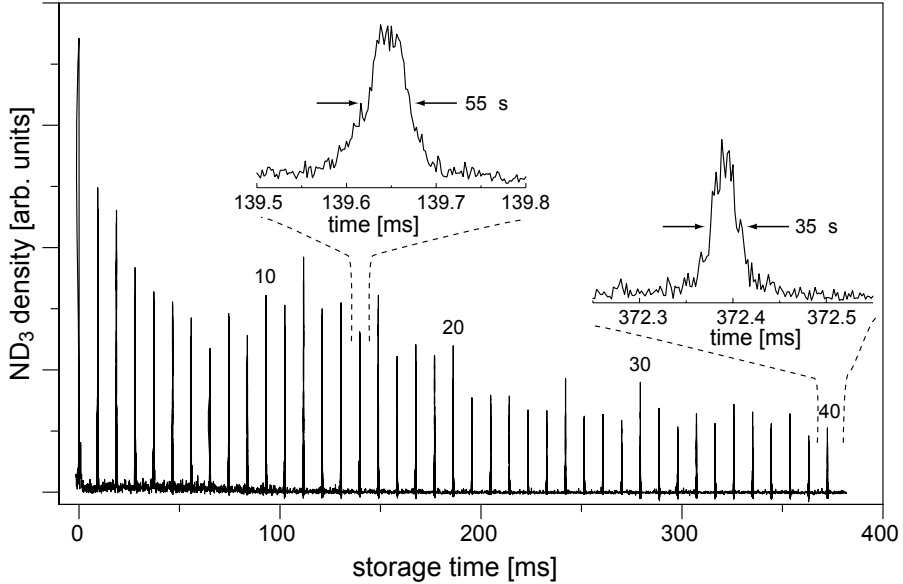


Figure 5.8: Round-trip TOF profiles. The density of ammonia molecules at the detection zone inside the synchrotron is shown as a function of storage time. The two insets show zoom-ins of the TOF profiles of the 15<sup>th</sup> and 40<sup>th</sup> round trips. Their respective temporal widths, as determined from Gaussian fits, correspond to longitudinal position spreads of 4.8 mm and 3.0 mm.

to both bends, and thus is not denoted with a bend number. One round trip for molecules moving at 87 m/s takes approximately 9.3 ms, implying that the voltages applied to the top and middle bottom electrodes are switched 645 times per second, and the voltages applied to the bottom and middle top electrodes are switched 860 times per second. The cascading double switch scheme for the ring voltages between ground (or bias field),  $\pm 2.7$  kV, and  $\pm 5$  kV is shown in the boxed inset.

## 5.4 Experimental results and discussion

### 5.4.1 Bunching molecules in the synchrotron

For the experiments presented in this chapter, packets of ammonia molecules are decelerated to 87 m/s and bunched in the synchrotron. Figure 5.8 shows the time-of-flight (TOF) profile of the ammonia density in the detection zone of the ring as a function of storage time. As compared to Figure 4.7, the TOF peaks are narrower, approaching a delta-function on this scale. To more clearly

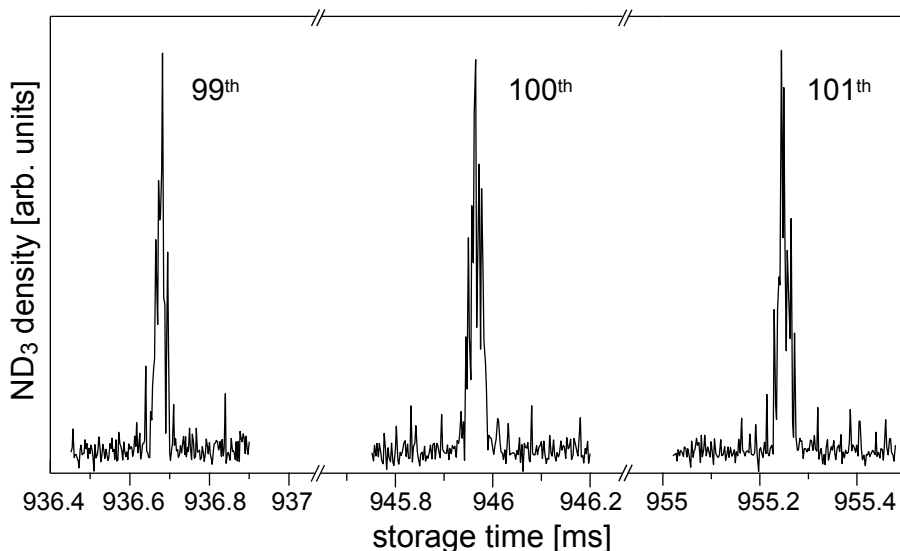


Figure 5.9: TOF profiles for the 99<sup>th</sup>, 100<sup>th</sup>, and 101<sup>th</sup> round trips. Here the molecules are stored for nearly 1 s. As determined from Gaussian fits to these profiles, the molecular packet retains a temporal width of only 26.5  $\mu$ s, corresponding to a position spread of 2.3 mm, after flying a distance of over 80 m.

illustrate the absolute widths of these peaks, a zoom-in of two TOF profiles is shown as insets in the Figure. From Gaussian fits to these profiles, the 15<sup>th</sup> round trip is determined to have a temporal width of 55  $\mu$ s, corresponding to a longitudinal position spread of 4.8 mm, and for the 40<sup>th</sup> round trip a temporal width of 35  $\mu$ s is determined, corresponding to a longitudinal position spread of 3.0 mm. After an initial rapid decrease, and some modulations, the signal is seen to become relatively constant. Starting from about the 20<sup>th</sup> round trip, the signal decays with a 1/e time of 0.5 seconds, which is consistent with losses due to collisions with background gas in our  $2 \times 10^{-8}$  mbar vacuum. Round trips 1 – 8 were measured at a 10 Hz rate, round trips 9 – 19 were measured at a 5 Hz rate, and round trips 20 – 40 were measured at a 2.5 Hz rate.

Reducing the repetition rate of the beamline and detection still further, to 1 Hz, molecules are observed completing their 100<sup>th</sup> round trip, as shown in Figure 5.9. Even after flying over 80 m, the molecules remain together in a packet the length of only 2.3 mm. The decrease in signal between the 40<sup>th</sup> and the 100<sup>th</sup> round trips is attributed to collisions with the background gas. Still, a good signal-to-background is observed in the experiment.

The TOF profiles for each of the 40 round trips shown in Figure 5.8, as well as for the 99<sup>th</sup>, 100<sup>th</sup>, and 101<sup>st</sup> round trips shown in Figure 5.9, were

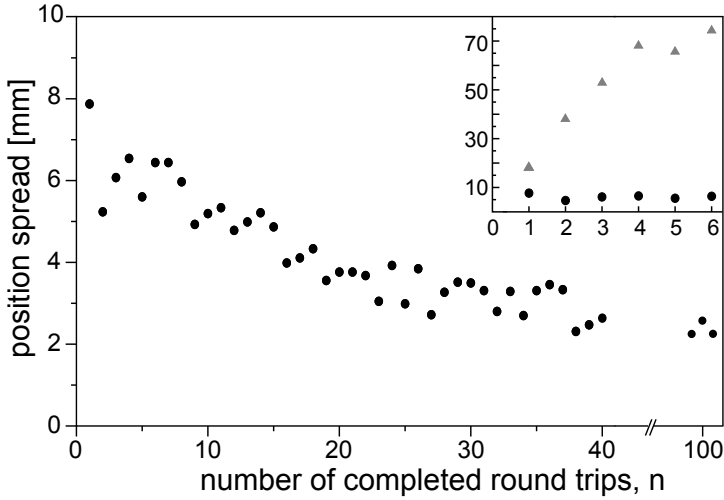


Figure 5.10: The measured longitudinal position spreads of the stored molecules in the detection zone, determined from the TOF profiles shown in Figures 5.8 and 5.9, are plotted as a function of the number of completed round trips,  $n$ . The inset compares the longitudinal position spread of the stored molecules after the first 6 round trips with ( $\circ$ ) and without ( $\triangle$ ) bunching; the latter data points are taken from Figure 4.8.

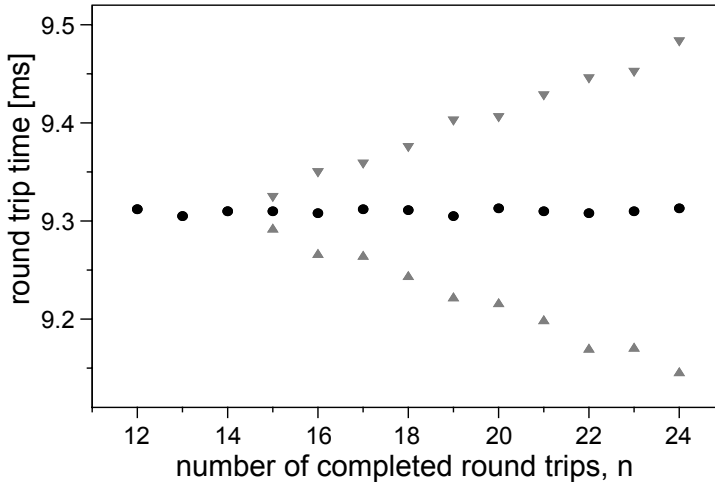


Figure 5.11: The round trip time, defined as  $t(n) - t(n - 1)$ , where  $t$  is the time of arrival and  $n$  is the number of completed round trips, is plotted as a function of  $n$ . Measurements are shown when the mean velocity of the packet is held constant ( $\circ$ ), increased ( $\triangle$ ), or decreased ( $\nabla$ ).

fitted with Gaussians. From these fits, the longitudinal position spread can be inferred; this is plotted as a function of completed round trips,  $n$ , in Figure 5.10. For comparison, the inset shows the longitudinal position spread of a packet of molecules completing 6 round trips with ( $\circ$ ) and without ( $\triangle$ ) using the buncher in the ring; the latter data points are taken from Figure 4.8. Although the molecules are stored for less than 100 ms, the unbunched molecular packet already obtains a length of 70 mm, as compared to the 6 mm bunched molecular packet. The width of the bunched packet is seen to further decrease until about the 20<sup>th</sup> round trip, after which it stabilizes around a value of 3 mm. This initial loss is attributed to injected molecules that are at first accepted into the ring but possess trajectories that are unstable in the long term. As the width of the packet stays constant for the later round trips, one can conclude that the trajectories of these molecules are stable and they will, in principle, be confined indefinitely. In other words, by confining the molecules for a minimum of 15 round trips, one really probes the dynamics of the trapped molecules and can safely assume that any contributions from the meta-stably trapped molecules is negligible. Hence, all investigations into the ring dynamics have been measured here after the molecules have completed either their 15<sup>th</sup> or 20<sup>th</sup> round trip, which is a compromise setting between good signal – as longer storage times suffer from losses due to background collisions – and studying the characteristics of the (truly) trapped molecules.

From the Gaussians fitted to the data shown in Figure 5.8, one can also determine the time needed by the molecules to complete one round trip; these times are plotted as circles ( $\circ$ ) in Figure 5.11. Molecules moving at 87 m/s around the 81 cm circumference ring take 9.31 ms to complete one round trip. In these measurements the velocity is held constant, i.e., the buncher fields are switched normally at  $z'=z_0$  ( $\Delta W = 0$ , see Figure 5.5), and therefore the round trip time is also constant. Measurements have also been conducted in which, starting after the 15<sup>th</sup> round trip, the molecules' kinetic energy is changed by  $(\pm)0.025 \text{ cm}^{-1}$  per round trip by switching the buncher fields at  $z' \neq z_0$  when the synchronous molecule is at some other position in the gap where its  $\Delta W \neq 0$  (see Figure 5.4). As expected, the decelerated packet revolves more slowly around the ring, while the accelerated packet revolves faster around the ring with respect to the round-trip time for a packet when the synchrotron is normally operated.

### 5.4.2 Characterizing the longitudinal potential well

Figure 5.12 shows the TOF profiles of a packet of ammonia molecules completing 20 round trips in the ring, of which the molecules are normally bunched for the first 15 round trips, and are either **(a)** decelerated ( $-\Delta E_{\text{kin}}$ ) or **(b)** accelerated ( $+\Delta E_{\text{kin}}$ ) in each gap for the final five round trips. The upper bold trace in both graphs is the same TOF profile of the 20<sup>th</sup> round trip with the ring operated normally ( $\Delta E_{\text{kin}} = 0$ ); its time-of-arrival is assigned to  $t_0$ . In the

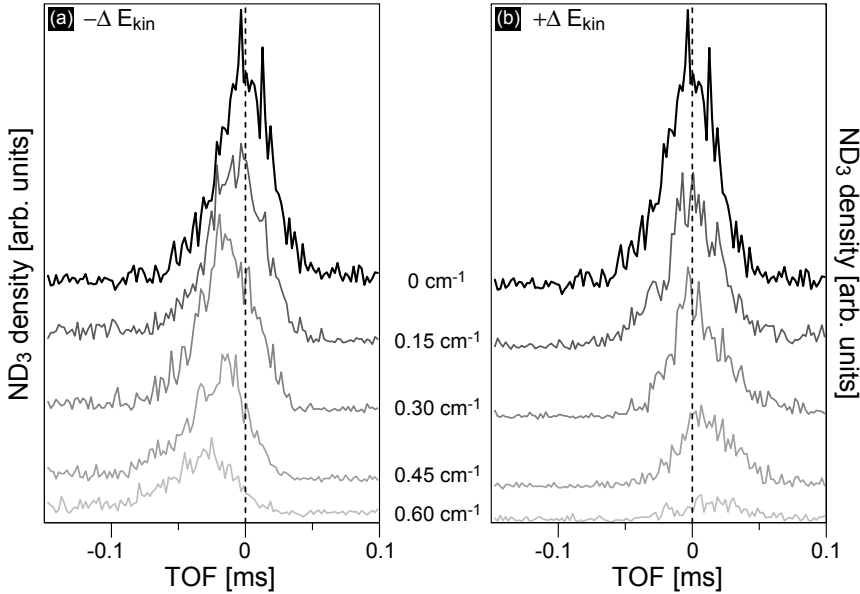


Figure 5.12: TOF profiles of the density of ammonia molecules in the detection zone after completing 20 round trips with the buncher fields switched such that the energy in the packet was either (a) decreased or (b) increased between  $0.015 - 0.06 \text{ cm}^{-1}$  per gap, for the final five round trips, i.e. a total  $\Delta E_{\text{kin}} = (\pm)0.15 - 0.6 \text{ cm}^{-1}$ . The arrival-time of the upper bold trace ( $\Delta E_{\text{kin}} = 0 \text{ cm}^{-1}$ ) is assigned as  $t_0$ ; this is the same TOF profile in both panels. The total  $\Delta E_{\text{kin}}$  added to/extracted from the packet is labelled in the center of the figure and refers to the traces in both graphs; the traces from top to bottom are either steadily decelerated (left) or accelerated (right). The traces are vertically shifted for clarity, and the dashed lines are guides for the eye.

left panel, the traces from top to bottom have more energy removed from the packet, whereas in the right panel, the traces from top to bottom have more energy added to the packet. The total amount of energy extracted from/added to each packet is labelled in the center of the Figure, ranging from  $(\pm)0.15$  to  $(\pm)0.60 \text{ cm}^{-1}$ .

Note that the more decelerated molecules are seen to arrive at earlier flight times (left panel), and vice-versa, the more accelerated molecules are seen to arrive at later flight times (right panel). This may seem counter-intuitive, since one would expect slower molecules to arrive in the detection zone later and faster molecules to arrive in the detection zone sooner, however, one simply needs to take the molecules' z-position in the gap into account. It was established in the discussion for Figure 5.4 (Section 5.2.1), that the molecules

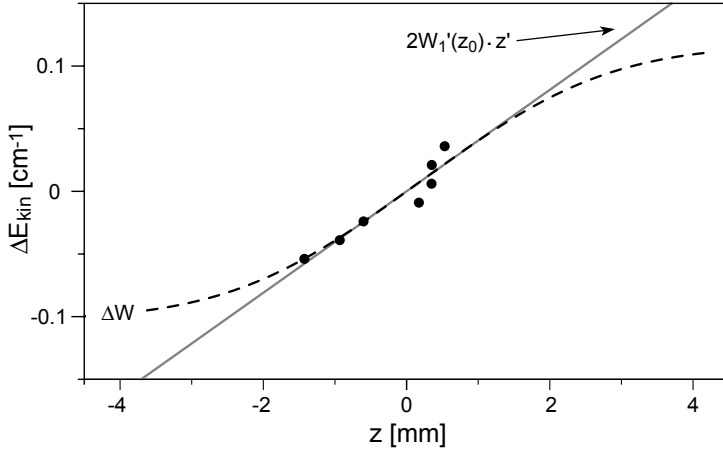


Figure 5.13: The packet's total change in energy ( $\Delta E_{\text{kin}}$ ) is plotted as a function of their  $z$ -position in the gap with respect to the middle of the gap (plotted as circles  $\circ$ ), as determined from analysis of the TOF profiles shown in Fig. 5.12. The dashed line in the Figure shows the results from a linear fit to the data. The slope of the fit,  $m = 0.04 \text{ cm}^{-1}/\text{mm}$ , can be used in equation 5.3 to solve for the frequency of the buncher; in this case  $\omega_{\text{syn}}/2\pi = 39 \text{ Hz}$ . The data fits well to the  $\Delta W$  curve (solid line) for a molecule with a  $r'_{\text{equi}} = 1.5 \text{ mm}$ .

which are stably decelerated are actually those which are further ahead, due to the shifted  $z'$ . Thus the  $\text{ND}_3$  density at different positive  $z$ -positions in the buncher can be determined by taking the difference between the time-of-arrival between the normally bunched molecules and those that were accelerated (decelerated), together with the final respective velocities of the packet. That is to say the TOF profiles in Figure 5.12(a) are probing the  $\text{ND}_3$  density at different positive  $z$ -positions in the buncher. In the same manner, the TOF profiles in Figure 5.12(b) are probing the  $\text{ND}_3$  density at different negative  $z$ -positions in the buncher, since the molecules that are stably accelerated are those which are further behind.

In Figure 5.13 the total change in energy ( $\Delta E_{\text{kin}}$ ) of the packet is plotted ( $\circ$ ) as a function of their  $z$ -position in the gap, with respect to the middle of the gap. The molecules that are normally bunched arrive at  $z = z_0 = 0$ . A linear fit (dashed line) to the data approximates the harmonic section of the buncher's restoring force. The slope of the fit,  $m = 0.04 \text{ cm}^{-1}/\text{mm}$ , equals  $2W'_1(z_0)$ . Substituting this value into Equation 5.3 yields  $\omega_{\text{syn}}/2\pi = 39 \text{ Hz}$ . This is in fairly good agreement with the value determined from calculated trajectories of 46 Hz. Additionally, this measurement can be compared to the calculated  $\Delta W$  curves for various  $r'_{\text{equi}}$  positions presented in Figure 5.6. The  $\Delta W$  curve shown in Figure 5.13 (solid line) is for a  $r'_{\text{equi}} = 1.5 \text{ mm}$ . This

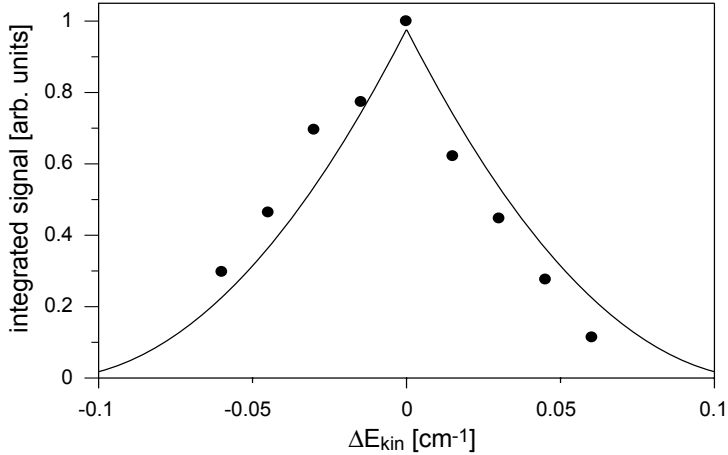


Figure 5.14: The integrated signal of the stored molecules in the detection zone, determined from the TOF profiles shown in Fig. 5.12, is plotted as a function of the packet's total change in energy ( $\Delta E_{\text{kin}}$ ). The solid line in the figure shows the results from a fit to the data using equation 5.6, which yields a synchrotron oscillation frequency in the longitudinal potential of 42 Hz.

graph can be immediately compared to Figure 5.5 (Section 5.2.1), however in the latter figure the  $r'_{\text{equi}} = 2.3$  mm. This difference can be explained by misalignments of the ring and the shift in  $r'_{\text{equi}}$  due to the kicker; effects from the kicker will be extensively discussed in Chapter 6.

In Figure 5.14 the integrated signal for each TOF profile shown in Figure 5.12 is plotted as a function of  $\Delta E_{\text{kin}}$ . The integrated signal is normalized to the trap's deepest point,  $z = z_0$  ( $\Delta E_{\text{kin}} = 0$ ). The integrated signal becomes less as the trap becomes shallower towards the edges. Note that the amount of  $\Delta E_{\text{kin}}$  that can be added to/removed from the molecules is limited due to neighboring resonance stopbands, as described in Section 2.2.3 (see Figure 2.6), and that losses due to these bands might already be influencing the integrated signal. From this data one can estimate the size of the phase-space area that the packet occupies, as discussed in Section 5.2.1. The solid line in the figure shows the results from a fit to the data using Equation 5.6. The synchrotron oscillation frequency is determined to be 42 Hz.

Figure 5.15 presents measurements investigating the expansion time of the molecules after release from their longitudinal well. As in Figure 4.8, such a measurement provides an estimate of the temperature of the packet – the colder the packet, the slower the expansion – which can also be used to give an estimate for  $\omega_{\text{syn}}$ . First, the molecules are confined and bunched in normal operation for some storage time, then the buncher is turned off (confinement

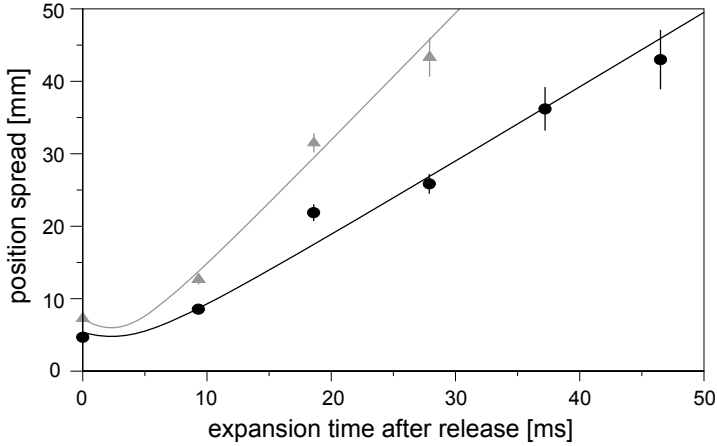


Figure 5.15: The position spread of a molecular packet that completes either four ( $\Delta$ ) or sixteen ( $\circ$ ) round trips before being released from the longitudinal well is plotted as a function of expansion time; error bars are shown where necessary. The solid lines in the Figure show the results from a simple formula fitted (Equation 3.11) to the expansions.

fields are still applied), and the longitudinal spread of the packet is monitored. Molecules completing their 4<sup>th</sup> and 16<sup>th</sup> round trips before being released are indicated by triangles ( $\Delta$ ) and circles ( $\circ$ ), respectively. The solid lines in the Figure show the results from a fit of Equation 3.11, but here replacing  $t$  with  $(t - t_0)$ , where  $t_0$  is the time at which the packet has its minimum position spread – the molecules are focused at the quarter-ring position by the last buncher forces before freely expanding. The position and velocity spreads of the packet released after the 4<sup>th</sup> round trip are found to be 6 mm and 1.8 m/s, respectively. For the packet released after completing its 16<sup>th</sup> round trip, a position and velocity spread of 4.8 mm and 1.0 m/s is determined.

The velocity spread can be inserted into Equation 3.12 to yield a temperature estimate of the packet. For the packet released after 4 round trips the temperature is determined to be 1.4 mK, and for the packet released after 16 round trips the temperature is determined to be 0.5 mK. Note that additional measurements were taken for a packet released after completing its 25<sup>th</sup> round trip, where the same temperature value of 0.5 mK was determined. So the hottest molecules, although initially confined, are slowly expelled from the ring. This is attributed to coupling between the longitudinal and transverse motions, which causes the initial decrease in the position spread observed in Figure 5.10. That the temperature of the packet remains constant for the later round trips is further evidence that these are the molecules which are, indeed,



stably trapped. Additionally, one can use  $\Delta z$  and  $\Delta v_z$  to solve for  $\omega_{\text{syn}}$ ; this yields a synchrotron oscillation frequency of 47 Hz and 34 Hz for a packet released after completing its 4<sup>th</sup> and 16<sup>th</sup> round trips, respectively.

Note that all four values determined experimentally for  $\omega_{\text{syn}}/2\pi$  are based on measurements taken over 50 ms. At a 40 Hz rate, the packet has then only completed two synchronous oscillations. It is difficult to assign a very precise frequency based on these measurements. The average value for  $\omega_{\text{syn}}/2\pi$  is 40 Hz. Thus the measured values are in reasonable agreement with the predicted 46 Hz (Section 5.2.1). In any case, some deviation from the theoretical value is expected due to misalignments in the ring. It was found that upon cutting the electrodes, the stress of the bent rods caused them to warp by ‘springing’ outwards, meaning that the two hexapole half-rings are not perfect semi-circles. Hence the molecules are closer to the geometrical center of the hexapole than would be expected – as also seen in Figure 5.13 – where the longitudinal oscillation frequency is smaller (see Figure 5.6).

### 5.4.3 Phase-space matching

In this section, the optimum phase-space matching between the emittance of the molecular packet from the injection beamline and the acceptance of the ring will be investigated. Presented in Figure 5.16 is a longitudinal focusing curve for the molecules after completing 20 round trips in the ring (solid line). For reference, the longitudinal focusing curve for position focusing at the injection point from Figure 3.10 is shown (dotted line), as well as a longitudinal focusing curve for velocity focusing (dashed line). Clearly the buncher (in the beamline) is on for a longer time when focusing at the entrance of the ring and a shorter time for focusing at infinity. The focusing forces are applied for a total of 110  $\mu\text{s}$ , an amount in between that needed for the position and velocity foci; in phase-space, the packet is rotated over an angle of 75°. This best matches the longitudinal acceptance of the buncher in the synchrotron, which corresponds to the (synchrotron) buncher’s quarter-ring focal point.

The timing between the arrival of the molecular packet and the switching on of the synchrotron is critical for ensuring the acceptance of a large number of molecules into the ring. Figure 5.17 shows the density of ammonia molecules at the detection zone inside the synchrotron after completing 20 round trips as a function of the time delay of turning on the synchrotron;  $t = 0 \mu\text{s}$  refers to the time that the decelerator is switched off. The plots above the curve show the longitudinal phase-space dimensions of the packet,  $[\Delta z \times \Delta v_z] = [4 \text{ mm} \times 4 \text{ m/s}]$  (dotted-line oval), and the longitudinal acceptance of the ring at the quarter-ring position,  $[4 \text{ mm} \times 1 \text{ m/s}]$  (solid-line oval). Molecules located in the overlapping phase-space areas (shaded in gray) will be accepted into the ring. The ring is turned on either (a) 4160  $\mu\text{s}$ , (b) 4190  $\mu\text{s}$ , (c) 4220  $\mu\text{s}$ , (d) 4250  $\mu\text{s}$ , and (e) 4280  $\mu\text{s}$  after the decelerator has been switched off. At the optimal phase-space matching, in (c), the centers of the two areas coincide

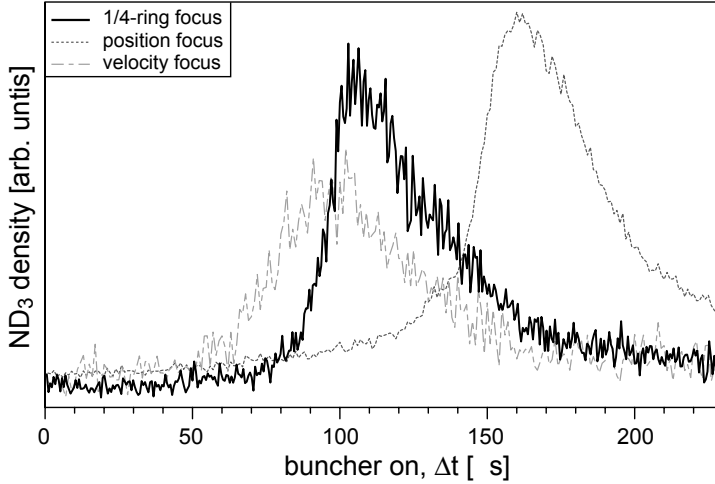


Figure 5.16: *The density of ammonia molecules at the detection zone inside the synchrotron after completing 20 round trips as a function of the total time  $\Delta t$  that the buncher (in the beamline) is switched on is shown (solid line). The measurement shows an optimum at 110  $\mu\text{s}$ , or a total of 10 mm of buncher forces. The longitudinal focusing curve for position focusing (dotted line), as measured at the entrance of the ring, and for velocity focusing (dashed line), as measured after the fourth round trip, are also shown.*

maximizing the overlap. Clearly, if the ring is switched on too soon, which is the case in plot (a), the centers of the two phase-space areas are separated by a distance of 5.2 mm. Likewise, if the ring is switched on too late, as sketched in plot (e), the centers of the two phase-space areas are separated by a distance of -5.2 mm. There is a partial overlap in (b) and (d), where the centers of the areas are ( $\pm$ )2.6 mm apart.

Let us now consider the phase-space matching for the transverse directions. As briefly discussed in Section 3.2.4, the ratios of  $\frac{\Delta x}{\Delta v_x}$  and  $\frac{\Delta y}{\Delta v_y}$  can be adjusted with two hexapoles. Figure 5.18 presents the density of ammonia molecules at the detection zone inside the synchrotron after completing 20 round trips (black) as a function of the effective position of the third hexapole (or lens). For comparison the  $\text{ND}_3$  density in the detection zone upon injection (gray) is also shown. In this measurement, both the total duration (1.7 mm) and effective position of the second hexapole is fixed, while the effective position of the third hexapole is varied; the total duration of the third hexapole, though, is kept fixed at 2.05 mm following from Figure 3.11. For the measurement on the 0<sup>th</sup> round trip we expect, the highest intensity when the packet is focused the strongest, which will be the case when a 1:1 image is made. Note that the drop after 45 mm is due to the fact that the focusing force decreases towards

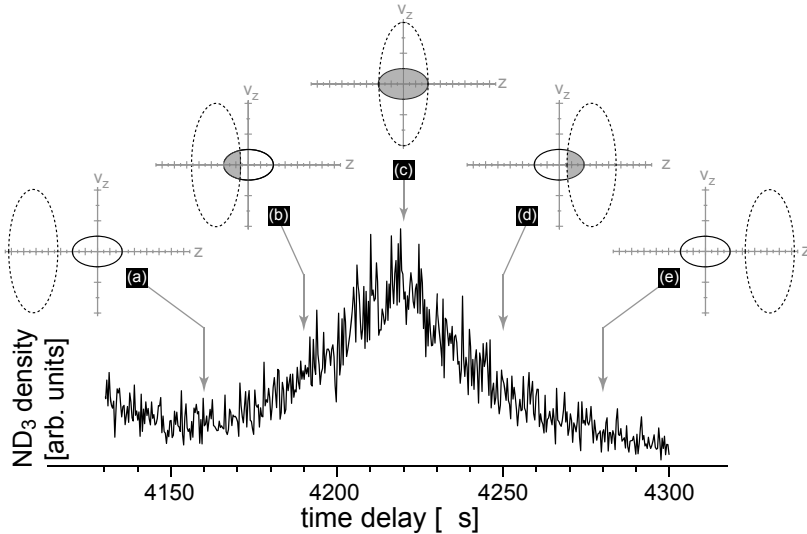


Figure 5.17: The density of ammonia molecules at the detection zone inside the synchrotron after completing 20 round trips as a function of time delay for the switching on of the ring;  $t = 0 \mu\text{s}$  refers to the time that the decelerator is switched off. The insets (a)-(e) above the curve show cartoons representing the phase-space dimensions of the molecular packet (dotted-line oval) and the acceptance of the ring (solid-line oval) for the corresponding time delays of injection. Molecules are accepted when the phase-space areas overlap, marked by gray shading in the insets. Few (or no) molecules are captured in the longitudinal well of the ring if it is turned on either too early or too late.

the ends of the hexapole. One would expect the same trend to be seen in the measurement taken after 20 round trips, yet surprisingly this is not the case. Instead a lens position of about 10 mm is found, magnifying the packet by 1.9, to yield the maximum signal. This means that the beam is cooled in the third hexapole.

#### 5.4.4 Bunching two packets of molecules in the synchrotron

Thus far, all the experiments have been concerned with the storage and bunching of a single packet in the synchrotron. However, for possible collision studies in the synchrotron a bare minimum of two packets needs to be properly stored and bunched. As demonstrated in the last chapter, two packets of molecules can be consecutively injected and subsequently confined without interfering with one another. Ideally one would load the molecules the same way as in Figure 4.9, and now simultaneously bunch one packet in each gap. In the cur-

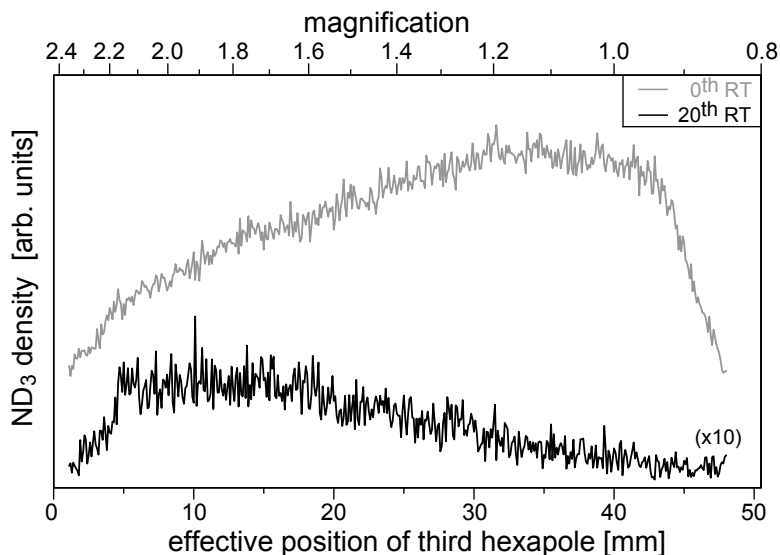


Figure 5.18: The density of ammonia molecules at the detection zone is shown at injection (gray) and inside the synchrotron after completing 20 round trips (black) as a function of effective position of the third hexapole (lens). The signal for the injected beam is seen to be optimum near 35 mm, making a near 1:1 image. The maximum signal in the ring occurs at an effective lens position of around 10 mm, which is a magnification of 1.9 times.

rent set-up, however, the molecules can only be injected co-linearly. This leads to the following predicament: in order to bunch a packet leaving bend 1 and entering bend 2, bend 1 must be turned off and bend 2 must be turned on. Yet, to bunch a packet leaving bend 2 and entering bend 1, bend 1 must be turned on and bend 2 must be turned off. As one can see, simultaneously running the ring in such a mode would remove the dichotomy of the ring and no bunching would take place. Instead, to enable a demonstration of dual packet bunching in the current set-up, the synchrotron is operated using a different, albeit not optimum, switching scheme. We have introduced a ‘fake’ gap at a quarter ring position, i.e., the voltages are switched to a buncher configuration twice as often. This means that while one packet is being properly bunched in the (real) gap, another packet a quarter-ring away only experiences one-half of the bunching sequence, that is, it simply experiences an abnormal confinement force. Note that the packet is also the smallest at this position - although I often refer to the bunching taking place ‘in the gaps’, the buncher configuration merely applies the focusing forces in the gap regions actually (longitudinally) focusing the packet at a position a quarter-ring downstream. Hence, one expects only minimal losses due to the effect of the ‘fake’ gap on the tightly

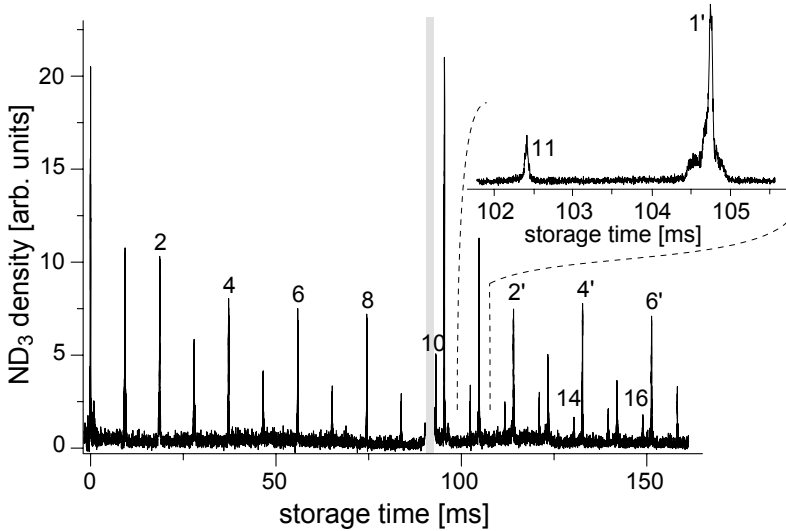


Figure 5.19: TOF profiles showing two packets of ammonia molecules revolving inside the synchrotron. The second packet is injected 95.3 ms after the first packet, and trails it by 20 cm. Prior to injection of the second packet, the detection system is briefly switched off (indicated by the gray bar) to avoid saturation of the detector as the undecelerated part of the ammonia beam passes through the detection region. The alternating intensities observed between round trips arise from a less than ideal loading of the packet into the ring. The inset shows a zoom-in of a TOF profile of the first packet after completing its 11<sup>th</sup> round trip and the second packet after completing its 1<sup>st</sup> round trip.

focused molecules at the quarter-ring position.

Figure 5.19 shows a similar measurement to that in Figure 5.8. Here a second molecular packet is injected 95.3 ms after injection of the first packet. In this case, the second packet trails the first by 20 cm. For symmetry reasons, the extra switching for the ‘fake’ gap is always performed, even if only one packet is stored in the ring. Some oscillations are seen in the first ten round trips of the 1<sup>st</sup> packet which are not present under normal operation conditions. This is attributed to effects from the less-than-ideal confinement force experienced by the molecules during the ‘fake gap’. Nevertheless, the scheme suffices for a demonstration of multi-packet loading. In principle, one can load many more packets into the ring by introducing more ‘fake’ gaps. However, as molecules in these ‘fake’ gaps experience a different transverse force as in a true gap, a more promising route is to construct a ring out of many short segments. As the depth of the longitudinal well is inversely proportional to the distance between the

gaps, the longitudinal well will be deeper in a ring with many short segments. Moreover, as the symmetry of such a ring is higher, the transverse well will also be deeper. The design of such a multi-segmented hexapole ring will be discussed in Chapter 7 of this thesis.

### 5.5 Conclusions and outlook

I have demonstrated the stability of molecules confined in three dimensions in a synchrotron. Molecules are confined for up to 1 s in a longitudinal potential well with a temperature of about 0.5 mK and a trapping frequency of ca. 40 Hz. Additionally, two packets, travelling co-linearly, were successfully confined and bunched in the ring. One of the most obvious applications of the ring is to use it as a neutral molecule collider where stored packets of molecules will meet as they revolve in both directions around the ring. Storing many such packets over an extended time increases the number of collisions by orders of magnitude.

# Chapter 6

## Motional resonances in a molecular synchrotron

### 6.1 Introduction

Bunching elements, used to provide the necessary longitudinal focusing forces in a synchrotron, break the cylindrical symmetry of the ring. As a consequence, the transverse confining force will vary as a function of the longitudinal position in the ring. The variation of the confinement force has major consequences for the stability of the particles's trajectories. For certain longitudinal velocities, the disturbance caused by the bunchers will add up, meaning that all trajectories become unstable and those particles will be lost. These unstable velocity regions are well known in charged particle accelerator physics and great efforts are exerted in the design of a synchrotron to minimize these so-called *stopbands* or motional resonances as discussed in Section 2.2.3. This chapter presents an experimental study of motional resonances occurring in a molecular synchrotron. These resonances can be understood and predicted from a simple model, and their width minimized using a correcter configuration in the synchrotron. Moreover, the resonances can be completely avoided by appropriately changing the voltages applied to the ring electrodes to allow for molecules over a wide velocity range to be stored.

### 6.2 Experimental set-up

A schematic of the full experimental set-up from source to synchrotron is shown in Figure 6.1. The  $\text{ND}_3$  molecules, prepared in the same fashion as described

---

Adapted from:  
C. E. Heiner, G. Meijer, and H. L. Bethlem, *Phys. Rev. A* **78**, 030702(R) (2008).

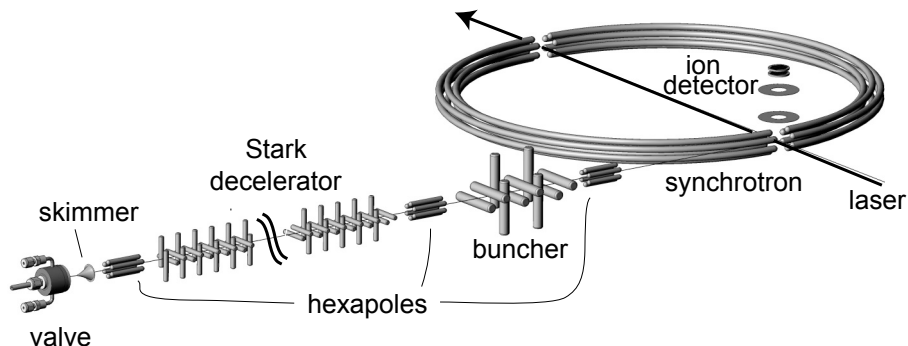


Figure 6.1: *Experimental set-up of the injection beamline and molecular synchrotron. A pulsed beam of  $\text{ND}_3$  molecules is decelerated, bunched and focused into a split hexapole ring. The two half-rings have a radius of 125 mm; they are separated by a gap of 2 mm. Molecules in the detection region are ionized using pulsed laser light around 317 nm, extracted perpendicularly to the plane of the ring, and counted by an ion detector.*

in Chapter 3, are decelerated to velocities between 60 m/s and ca. 100 m/s and subsequently injected into the synchrotron. The synchrotron, consisting of two semi-circular hexapole focusers, is operated such as to confine, correct, and bunch the packet of molecules, as described in Chapter 5. The  $\text{ND}_3$  molecules are detected at the injection point of the synchrotron via a (2+1)-resonance enhanced multi-photon ionization (REMPI) scheme using pulsed laser light around 317 nm.

## 6.3 Transverse motion in a synchrotron

### 6.3.1 Trajectory stability

As aforementioned the introduction of gaps affects the transverse motion of the molecules. In the gap, the confinement force temporarily vanishes. The disturbance on the molecules' trajectory as the result of one gap is small, and is, in itself, not necessarily a problem. However, if the disturbance accumulates the consequences will become disastrous. Calculated trajectories are shown in Figure 6.2 for a molecule with a longitudinal velocity,  $v_\phi$ , of 76 m/s (a,b) and 82 m/s (c,d). The voltage difference between adjacent electrodes,  $V$ , is taken to be 7.5 kV. In Figure 6.2(a), the radial position of a molecule flying with a longitudinal velocity of 76 m/s is plotted as a function of time. At this velocity, the equilibrium orbit is displaced by a distance  $r'_{\text{equi}} = 1.9$  mm from the geometrical center of the hexapole. The molecule whose trajectory



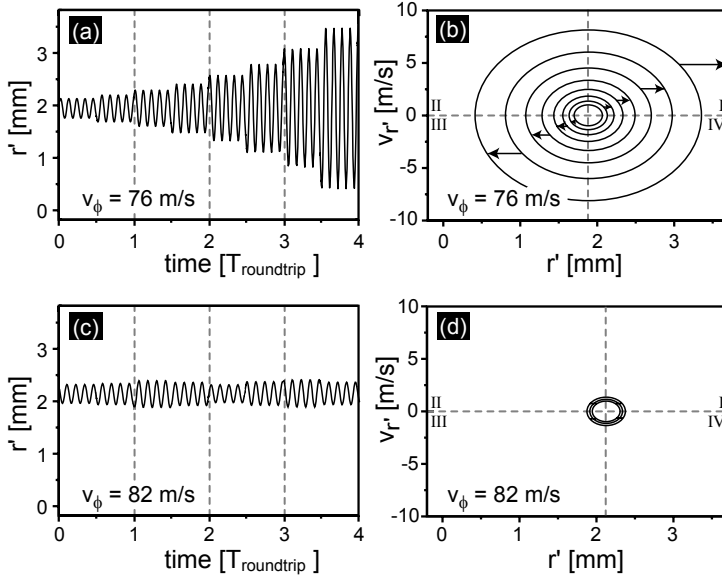


Figure 6.2: The radial trajectories of two molecules moving at (a) 76 m/s and (c) 82 m/s completing four round trips in a synchrotron. The same trajectories are plotted in phase-space in (b) and (d), respectively. At a voltage difference of 7.5 kV, a molecule moving at a velocity of 76 m/s makes 4.5 oscillations as it completes a half-roundtrip. In this case, the amplitude of the betatron oscillation grows each time the molecule passes the gap until it is lost from the ring. A molecule moving at a velocity of 82 m/s makes 4.1 oscillations as it completes a half-roundtrip. In this case, the amplitude of the molecule's betatron oscillation is modulated, but the overall result on the trajectory averages out.

is plotted in Figure 6.2(a) began at an initial radial position  $r'$  different from  $r'_{\text{equi}}$ , hence it oscillates around the equilibrium radius. At a voltage difference of 7.5 kV the betatron frequency is around 850 Hz. In phase-space, shown in Figure 6.2(b), this oscillation results in an ellipse. The molecule moves in a clockwise direction around the position and velocity of the closed orbit (located at the intersection of the gray dashed axes). When the molecule is in a gap, it experiences no confinement force and thus it moves along a straight horizontal line in phase-space; the trajectory in a gap is denoted by an arrow. The length and direction of the displacement is determined by the velocity of the molecule as it enters the gap. The molecule plotted in Figure 6.2(a) and (b) has a positive velocity and a positive displacement from the equilibrium orbit as it passes the first gap, i.e., the molecule is in quadrant I. This means it will

move away from the equilibrium orbit. After the gap, the molecule is captured again and now moves along a larger ellipse; the molecule now oscillates with a larger amplitude. At a forward velocity of 76 m/s the molecule oscillates 4.5 times around the equilibrium orbit every half round trip. This means that as the molecule passes the next gap, it has a negative velocity and a negative displacement from the equilibrium orbit, i.e. the molecule is in quadrant III. The molecule again moves away from the equilibrium orbit and the amplitude of its betatron oscillation further increases. As the molecule continues to revolve it is always located in either quadrant I or III as it enters a gap, and the molecule's oscillation amplitude continues to increase until it is ejected from the ring.

In Figure 6.2(c) and (d) similar graphs are shown for a molecule with a longitudinal velocity of 82 m/s. Again the molecule oscillates around the equilibrium orbit, which at this velocity is displaced by 2.1 mm from the geometrical center of the hexapole. For 82 m/s, the molecule oscillates 4.1 times around the equilibrium orbit every half round trip. As the molecule passes the first two gaps it is located in quadrant I and III, therefore its amplitude increases. However, as it passes the third gap it is located in quadrant IV. This means that the molecule now moves towards the equilibrium orbit and the amplitude of its betatron oscillation actually decreases. In this way, as the molecule continues to revolve its betatron oscillation amplitude varies – however – the overall effect of the gaps averages out, leaving the molecule stably confined.

### 6.3.2 Betatron tune

From the discussion above, one concludes that the number of betatron oscillations a molecule makes in between the gaps is decisive for whether or not its trajectory is stable. I have also discussed this in Section 2.2.3 in relation to accelerator physics, where this number is called the *betatron tune*,  $\nu$  [41]. Motional resonances occur when the betatron tune is equal to a half-integer value (including integer values). In order to stably confine molecules, the synchrotron needs to be operated at a tune that is sufficiently far away from these values. Note that although close to a half-integer value the trajectory is mathematically stable, the amplitude widely varies. If the amplitude at some point is larger than the aperture of the ring, the molecule will be lost from the ring. The width of the resonance, therefore, scales with the length of the gap and is inversely proportional to the aperture of the ring.

It is instructive to look at how the betatron tune scales with respect to the molecule's longitudinal velocity and the applied voltage difference between the ring electrodes. The betatron tune is given by  $\nu = \omega/n\Omega$ , where  $\omega/2\pi$  is the betatron frequency,  $\Omega/2\pi$  is the cyclotron frequency, and  $n$  is the number of repeating units, or superperiods, in the ring; in our case  $n = 2$ . Both the betatron and cyclotron frequency have a complicated dependence on  $v_\phi$  and  $V$ , however, a simple formula can be derived using the following approximations:

(i) the radius of the ring is much larger than the aperture, i.e.,  $R_{\text{ring}}/R_{\text{hex}} \gg 1$ , (ii) the electric field is perfectly harmonic, and (iii) the Stark shift is positive and linear,  $W_{\text{Stark}} = \mu_{\text{eff}}|\vec{E}|$ , where  $|\vec{E}|$  is the absolute value of the electric field and  $\mu_{\text{eff}}$  is the effective dipole moment of the molecule. Under these approximations the tune can be written as

$$\nu = \frac{R_{\text{ring}}}{nv_{\phi}} \sqrt{\frac{\mu_{\text{eff}}}{m} \frac{3V}{R_{\text{hex}}^3}}, \quad (6.1)$$

where  $m$  is the mass of the molecule. From this equation, one sees that in order to keep the tune at a constant value, the  $V$  must be adjusted proportionately to  $v_{\phi}^2$ . Note that when the tune is held constant, the equilibrium radius, approximately given by [5]:

$$r'_{\text{equi}} = \frac{v_{\phi}^2}{R_{\text{ring}} \frac{\mu_{\text{eff}}}{m} \frac{3V}{R_{\text{hex}}^3}}, \quad (6.2)$$

remains constant as well. This is important as it implies that the optimal position to inject and detect molecules does not change as a function of velocity.

## 6.4 Experimental results and discussion

### 6.4.1 Measurements in the synchrotron at various velocities

As compared to the measurements presented in Chapter 5, in which ND<sub>3</sub> molecules were always decelerated to 87 m/s, here the synchrotron is injected with packets of ND<sub>3</sub> molecules decelerated to between 60-105 m/s. The density of ND<sub>3</sub> molecules completing a number of round trips as a function of the molecules' longitudinal velocity is depicted in Figure 6.3. For comparison, the ND<sub>3</sub> density of the decelerated beam at the point of injection is also shown in the upper-most trace (0<sup>th</sup>); this curve is similar to the measurement shown in Figure 3.14. For each data point, a new time-sequence is loaded with the optimum timings for switching the electric fields throughout the injection beamline. Each measurement is averaged over 128 shots. For the measurements in Figure 6.3, the corrector was applied for a time corresponding to a total length of 30 mm per gap, i.e., over a length of 15 mm before and 15 mm after each gap.

After completing one round trip in the synchrotron, one can observe a change relative to the continuous signal observed at injection. A complicated distribution is seen with the highest density of ND<sub>3</sub> molecules observed near 82 m/s. It is predicted that molecules with a velocity as high as 105 m/s could be stored in the ring operated at this voltage difference (see Figure 4.2). This is clearly not the case experimentally as only a few molecules are observed above

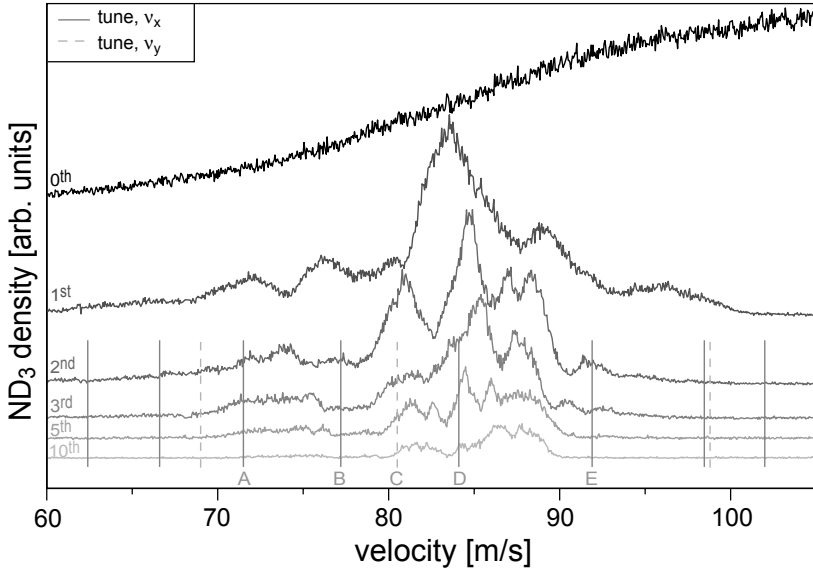


Figure 6.3: The density of  $\text{ND}_3$  molecules in the detection zone of the synchrotron having completed some number of round trips is shown as a function of velocity. Molecules at various velocities are not equally well accepted and stored in the ring. Additionally, the velocity at which stopbands arise are marked either by dotted lines ( $\nu_x$ ) or by dashed lines ( $\nu_y$ ); the labels A-E refer to the stopbands mentioned in the text. After 10 round trips, most of the meta-stably trapped molecules have been ejected from the ring by these stopbands, and only those on trajectories far enough away from a stopband are still observed.

90 m/s and no molecules are observed moving at a velocity above 100 m/s. This can be understood by taking the position at which the molecules are injected into the ring into account, which is around  $r' = 2$  mm from the geometrical center of the hexapole. This experimental constraint makes loading conditions more favorable for those molecules moving around 82 m/s, since these molecules have their equilibrium radius near 2 mm at this voltage difference.

In the absence of stopbands, one might expect to continue to observe a broad distribution of molecules centered around 82 m/s. However, as the molecules continue to revolve the signal decreases, and the profile features change due to the effects from the stopbands. The velocity where the betatron tune is equal to a half-integer value (including integer values), i.e., the velocities where the stopbands arise, are marked for betatron oscillations in the  $x$ -direction by dotted lines ( $\nu_x$ ), and for betatron oscillations in the  $y$ -direction by dashed lines ( $\nu_y$ ). After the fifth round trip (nine gaps), the additive effect to the

molecules' trajectories has resulted in the observed losses at certain velocities: few molecules are detected below 71.5 m/s ( $\nu_x = 5.0$ ), near 77 m/s ( $\nu_x = 4.5$ ), near 80.5 m/s ( $\nu_y = 4.0$ ), near 84 m/s ( $\nu_x = 4.0$ ), or above 92 m/s ( $\nu_x = 3.5$ ) – these values correspond to the stopbands labelled A-E, respectively. Upon completion of the tenth round trip most of the meta-stably trapped molecules have been ejected from the ring. Especially remarkable is that the large signal near 83.5 m/s (in the 1<sup>st</sup> round trip scan) is almost completely gone at this point due to the strength of stopband D. One can recognize both the velocities at which stopbands exist and those at which the molecules' possess stable trajectories: around 75 m/s (barely visible on this scale), 82 m/s, and 87 m/s. Particularly the fact that molecules near 82 m/s are detected and molecules near 77 m/s are no longer detected is consistent with the calculated trajectories presented in Figure 6.2 – where it was shown that the changes to the oscillation amplitude of a molecule moving at 82 m/s average out, whereas the oscillation amplitude of a molecule moving at 76 m/s grows larger than the aperture of the ring after only four round trips (seven gaps).

### 6.4.2 The correcter

The correcter configuration is necessary to aid in the confinement of molecules in the synchrotron over long storage times\*. As discussed in Section 5.2, the correcter configuration is simply a 30% stronger confinement force before and after the gaps set in place to compensate for the missing transverse forces during the gaps. The idea is that the molecules will then experience a constant transverse confinement force over the whole ring.

To determine the optimum correcter settings for molecules moving at different velocities, Figure 6.4 presents velocity scans of the ND<sub>3</sub> density after completing 20 round trips in the synchrotron for several effective correcter ('kick') lengths. The lengths, in mm, refer to the total correcter field on both sides of a gap. The upper-most trace is measured without applying the correcter, and almost no signal is detected after 20 round trips. The signal – and stopbands – begin to appear with increasing correcter lengths; note that these occur at the same velocities as observed in the lowest trace of Figure 6.3. Since the molecules are bunched for 8.5 mm in the synchrotron, one might naively expect a correcter force to be applied for a compensating length of  $\frac{1}{0.3}$  of the buncher, or kick = 28.3 mm. At kick = 25 mm the two signal bands are roughly equally intense, and the stopband is at its narrowest. It should be remarked that although the use of the correcter can not eliminate stopbands, it can reduce their strength (width) by effectively increasing the aperture of the hexapole; the central position of the stopbands is not affected.

It is interesting to note, though, that molecules moving between 80–83 m/s are seen to benefit from shorter correcter lengths, whereas molecules moving

---

\*In fact, the good signal-to-noise-ratio in the measurements in Chapter 5 was only possible by implementing the correcter configuration.

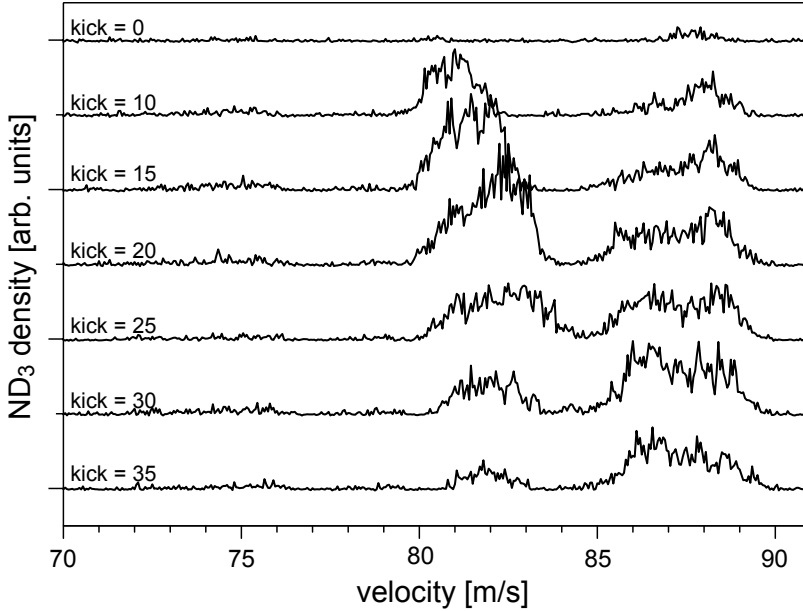


Figure 6.4: *The density of ND<sub>3</sub> molecules in the detection zone of the synchrotron after completing 20 round trips is shown as a function of the magnitude of the applied correcter forces (labelled in mm). It is experimentally advantageous to switch on the correcter configuration for a longer time than expected from numerical simulations, at kick = 20 mm.*

between 86–89 m/s are seen to benefit from longer correcter lengths. This effect can be traced back to the uncompensated centrifugal force that the molecules experience over the buncher’s remaining 2.5 mm of curved flight at every gap. This results in an outwards shift of  $r'_{\text{equi}}$ , for which the correcter’s increased focusing strength can help offset. In this way, it is understandable that a stronger signal is observed at kick = 30 mm for molecules moving at 87 m/s, the velocity for which all the measurements in Chapter 5 were taken, as the larger centrifugal force on the molecules during the same 2.5 mm would push the molecules even further outwards, requiring a longer kicker to return the molecules to their original  $r'_{\text{equi}}$ . We can speculate that to avoid stopband-induced losses, a shorter correcter is apparently beneficial for slower molecules.

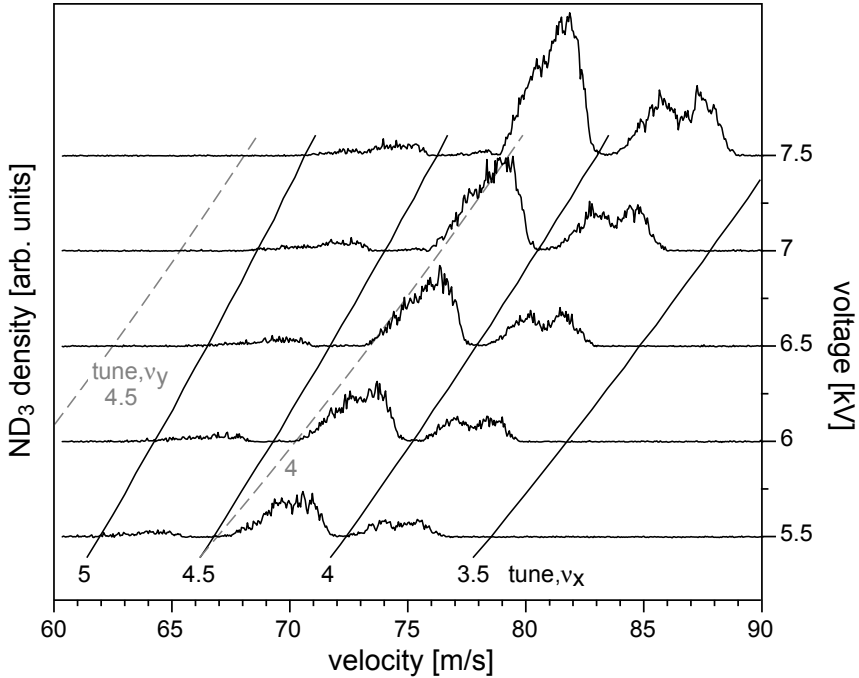


Figure 6.5: The density of  $\text{ND}_3$  molecules upon completion of the 20<sup>th</sup> round trip as a function of the molecules' longitudinal velocity measured at five different voltages. The solid and dashed lines indicate when the horizontal and vertical betatron tunes have a half-integer value, respectively.

### 6.4.3 Measurements in the synchrotron at various voltages

In Figure 6.5, the density of ammonia molecules after completing 20 round trips is again shown as a function of velocity, but now at five different ring voltages as indicated on the right hand side of the figure. Note that the voltage difference refers to the confinement configuration; the voltage difference for the corrector configuration is always set an additional 30% above that of the confinement. Each measurement is averaged over 96 shots. For the measurements in Figure 6.5 the corrector was used over a total length of 20 mm per gap, i.e., over a length of 10 mm before and 10 mm after each gap. Similar measurements taken after the 40<sup>th</sup> round trip (not shown) look identical after taking into account the additional losses due to collisions with background gas.

Looking at the upper-most measurement, taken at  $V = 7.5$  kV, again only molecules with velocities centered around 74 m/s, 81 m/s, and 86 m/s are stored, while molecules with velocities around 76 m/s and 83 m/s are lost from

the ring. Upon reducing the voltage difference the stable bands shift to lower velocities. In fact, 76 m/s corresponds to a stopband position for the measurement taken at  $V = 7.5$  kV but a signal band position in the measurement taken at  $V = 6.5$  kV. Of course, the stopbands shift as well, as the additive effects causing the resonances still exist, but simply occur at other velocities. In the lower-most measurement, taken at  $V = 5.5$  kV, molecules with velocities centered around 64 m/s, 70 m/s, and 75 m/s are stored, while molecules with velocities around 66 m/s and 72 m/s are lost from the ring. Although there is a stopband at 78 m/s, one might still expect to see another band of signal near 80 m/s; however such low confining voltages cannot balance the centrifugal force experienced by molecules moving at these higher velocities.

Using the electric field from a finite element program [67] and the known Stark shift of  $\text{ND}_3$  (taking a dipole moment of 1.48 D [83]), the betatron tune has been calculated as a function of the applied voltage and the longitudinal velocity of the molecules. The solid and dashed lines in Figure 6.5 indicate when the horizontal and vertical betatron tunes have a half-integer value, respectively. Note that within the approximations made to derive Equation (6.1) the horizontal and vertical tunes are identical. Apart from the (strong) half-integer resonances due to the bunching elements, additional (weaker) resonances may arise due to imperfections and misalignments of the ring\*. Every round trip, as the molecule passes a particular defect in the ring, its trajectory will be slightly disturbed. These disturbances will accumulate when the molecules make a half-integer number of oscillations *per round trip*. These resonances are found by setting  $n=1$  in Eq. (6.1). The dip observed around 86 m/s in the upper-most trace ( $V = 7.5$  kV) results from a resonance occurring when the molecules make 7.5 oscillations per round trip. The overall profile is seen to shift to lower velocities as the voltages are lowered. Although the exact velocities of the calculated stopbands is not always in perfect agreement with observed dips in the velocity scans, it is evident that the stopbands indeed explain all the observed structure. Numerical simulations have been also performed that were in reasonable agreement with these measurements; however, these simulations are highly sensitive to the exact input parameters. Furthermore, it proved difficult to properly take into account misalignments in the ring.

#### 6.4.4 Operating the synchrotron at a constant tune

The density of molecules injected into the synchrotron as a function of their forward velocity is presented in Figure 6.6(a); this is a similar measurement to that in Figure 3.14, but here only two buncher stages are used in the beamline. The measurement is averaged over 96 shots. The longitudinal velocity spread of the packet is on the order of 1 m/s. The number of molecules exiting the decelerator does not depend on the final velocity; however, due to the finite

---

\*The distortions of the ring from a perfect circle, as measured *ex-situ*, yielded deviations ranging from -0.3 mm to +0.8 mm.



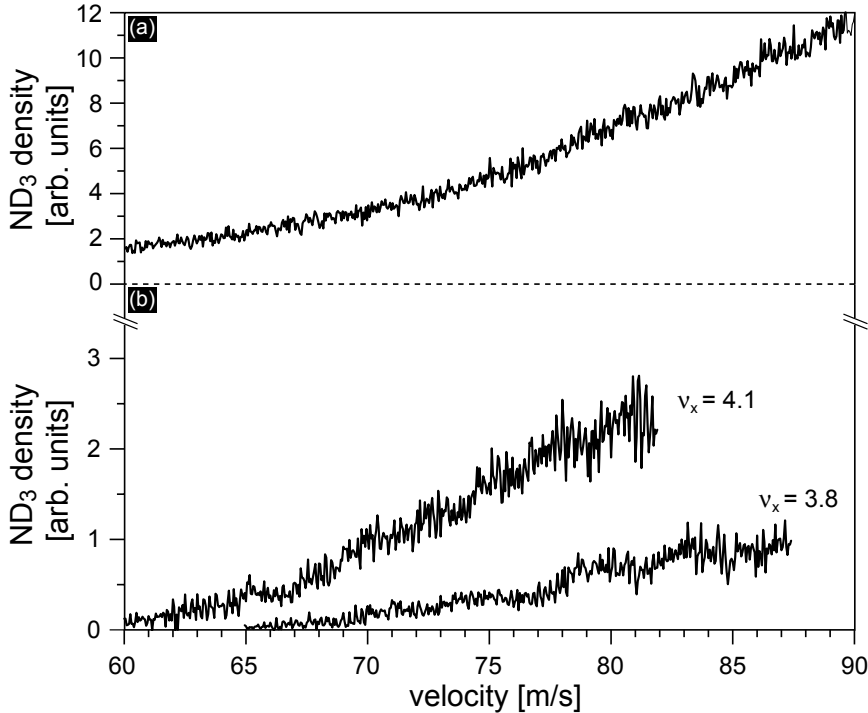


Figure 6.6: **(a)** The density of  $\text{ND}_3$  molecules at the injection position is shown as a function of the molecules' longitudinal velocity. **(b)** The density of  $\text{ND}_3$  molecules upon completion of the 20<sup>th</sup> round trip is shown as a function of the molecules' longitudinal velocity, but now with the voltages changed in sync with the velocity such as to keep the horizontal betatron tune constant at either 4.1 or 3.8 as indicated.

aperture of the hexapoles used in the beamline, the number of molecules loaded into the ring decreases at lower velocities (see Section 3.4.3).

From the discussion in this Chapter and in Chapter 2 it is clear that the synchrotron must be operated at a tune sufficiently far away from a resonance to successfully store molecules. In order to keep the tune constant, the ring must be operated at a specific voltage difference proportional to the square of the injected molecule's forward velocity. Figure 6.6(b) again shows the density of ammonia molecules after completing 20 round trips, but now the voltages are varied for each velocity such that the horizontal betatron tune,  $\nu_x$ , is always equal to either 4.1 or 3.8 as indicated in the Figure. In the measurement where  $\nu_x$  is kept at 4.1 the voltage difference is lowered from 7.7 kV at 82 m/s to 3.8 kV at 60 m/s, and in the measurement where  $\nu_x$  is kept at 3.8 the voltage difference is lowered from 7.7 kV at 87.5 m/s to 3.8 kV at 65 m/s. As can

be seen, the density of the stored molecules now resembles that of the injected beam shown in Figure 6.6(a). For the measurement where  $\nu_x$  is kept at 4.1 the signal at the 20<sup>th</sup> round trip at 82 m/s is almost four times lower, and at 60 m/s about twenty times lower, than that of the injected beam. The decrease at lower velocities is due to the shallower longitudinal trapping potential at lower voltages.

### 6.5 Conclusions and outlook

In this Chapter, it is demonstrated that molecules can be stored with different velocities in a molecular synchrotron. Motional resonances, similar to those observed in charged particle accelerators, are observed in the molecular synchrotron. Transmission of molecules in the ring can be enhanced and the strength of the resonances can be reduced by implementing a correcter configuration before and after bunching in the synchrotron. Furthermore, it is shown that these motional resonances can be understood and predicted from a simple model, and that they can be avoided by appropriately changing the voltages. Being able to tune the velocity of the stored beam is crucial for future collision studies.

# Chapter 7

## Outlook

### 7.1 Introduction

It has been demonstrated in this thesis that packets of molecules can be confined in tight bunches for long storage times in a molecular synchrotron consisting of two pieces. Our main motivation for performing research into a molecular synchrotron is for studying cold collisions, as discussed in Chapter 1. The number of collisions that takes place in a synchrotron depends on how many (counter-propagating) packets circle the ring and on how long the packets are stored. If injection occurs (in both directions) at a repetition frequency of 10 Hz\*, then after 2 seconds the ring will be full with 40 packets. At this point, one packet is injected and one packet is detected (still) at a rate of 10 Hz, so that each packet will be stored for 2 seconds. Thus before detection, every packet is stored for a time equivalent to the number of packets times 100 ms; the number of collisions scales as the number of packets squared. Furthermore, since the number of packets that can be stored in both directions is determined by the number of segments divided by two<sup>†</sup>, clearly it is advantageous to divide the synchrotron into more segments. In this chapter I discuss the design of the next-generation synchrotron consisting of 40 segments.

### 7.2 Design questions

The synchrotron used in the previous chapters was composed out of two curved (semi-circle) hexapoles. These hexapoles were made by bending straight elec-

---

\*Of course, one could consider running the experiment at a lower repetition rate to increase the time that the packets are stored. Whether or not this will be beneficial, however, depends on the experimental conditions.

<sup>†</sup>In Chapter 5, I used so-called 'fake' gaps to store more packets. Introducing fake gaps, however, significantly decreases the acceptance of the ring and this will not be considered as a viable option here.

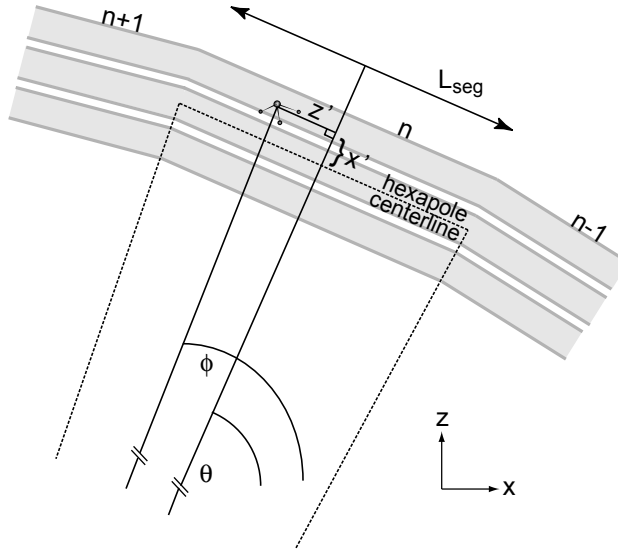


Figure 7.1: In the sketch, the  $n - 1$ ,  $n$ , and  $n + 1$  hexapoles of a ring consisting of  $n_{\text{seg}}$  straight hexapoles are shown. The coordinates with a prime are with respect to the hexapole centerline. The coordinates without a prime are with respect to the laboratory frame.

trodes into an arc on a rolling mill. The rolling process introduces a number of problems: (i) the remaining stress in the material will deform the electrodes, hence the alignment of the ring is rather poor, and (ii) the surface of the electrodes becomes damaged, thus raising the probability of electrical discharges (sparks) at defect sites when the electrodes are placed on high voltage differences. Straight hexapoles, on the other hand, are much easier to machine. Increasing the number of segments correspondingly decreases the angle of curvature of each hexapole segment. Hence one might wonder if it would be possible to approximate a ring with many, many straight segments.

### How many straight segments are necessary to form a circle?

We will use numerical simulations to answer this question. Let us consider a ring composed out of  $n_{\text{seg}}$  straight hexapoles, with length  $L_{\text{seg}}$ , that are positioned in the  $x$ - $z$  plane, as sketched in Figure 7.1. Note that there are no gaps between the sections in the simulations; however, gaps will be built into the synchrotron for bunching the molecules in the same manner as demonstrated in this thesis. The radius of the ring,  $R_{\text{ring}}$ , is taken to be 250 mm – exactly double that of the current two-piece set-up. The angle at which the hexapole is located with respect to the  $x$ -axis,  $\theta$ , can be written as  $2\pi \cdot (n/n_{\text{seg}})$ , where

$n$  is a running integer from  $n = 1, \dots, n_{\text{seg}}$ . For the purpose of the simulations, the position of a molecule is determined with respect to the hexapole centerline in which it is located, i.e., the program must translate laboratory coordinates  $(x, z)$  into the framework of the hexapole  $(x', z')$ . The hexapole in which a molecule is found can be determined simply by considering its tangential position,  $\phi$ , as defined by  $\sin \phi = z/\sqrt{(x^2 + z^2)}$ . A molecule is located in the  $n$ -th hexapole when  $\phi$  lies within

$$2\pi \left( \frac{n - \frac{1}{2}}{n_{\text{seg}}} \right) < \phi < 2\pi \left( \frac{n + \frac{1}{2}}{n_{\text{seg}}} \right). \quad (7.1)$$

In this way, the number of segments can be easily varied in the simulations. The electric force in the hexapole is assumed to be perfectly linear with a force constant of

$$k_{\text{hex}} = m\omega^2, \quad (7.2)$$

where  $m$  is the mass of the molecule and  $\omega/2\pi$  is the betatron frequency, taken here to be 1000 Hz. Note that for a linear force, the acceptance along the vertical direction,  $y$ , is independent of the number of segments; this allows the calculations to be performed in two dimensions.

In the simulation, we start with typically a 1000 molecules whose initial position,  $x$ , and initial velocity,  $v_x$ , are randomly chosen within a certain range that is larger than the acceptance of the ring. The initial  $z$  position is initially set to zero, while  $v_z$  is set to a value between 0 and 200 m/s. The program solves the equations of motion by using a second order Runge-Kutta method [84]. At every step, it is checked whether or not the distance of the molecule with respect to the centerline of the hexapole in which it is located (at that instance) exceeds the aperture,  $R_{\text{hex}}$ , of the hexapole;  $R_{\text{hex}} = 3.54$  mm in our simulations. The two dimensional acceptance for a given longitudinal velocity and number of ring-segments is found by the fraction of molecules that remains in the ring after 100 ms times the initial phase-space area.

A number of trajectories were calculated for molecules with a longitudinal velocity of 100 m/s moving through a ring consisting of 40 straight hexapoles, as plotted in Figure 7.2. Figure 7.2(a) shows the position of the molecules with respect to an (imaginary) circle with a radius of  $R_{\text{ring}}$ . Figure 7.2(b) shows the same trajectories but the position is now plotted with respect to the centerline of the hexapole in which the molecules are found. It is seen that the molecules – as expected – are on average closer to the centerline at the edges of the hexapoles than in the middle. Note that the molecules are located further away from the hexapole centerline than as they would be in an ideal ring. This causes a reduction in the acceptance size of the ring. The modulation to the trajectories will smaller for a ring composed of more segments. The force on the molecule is given by  $-k_{\text{hex}}$  times its displacement from the centerline; consequently, the force is also strongly modulated. This periodic force will lead

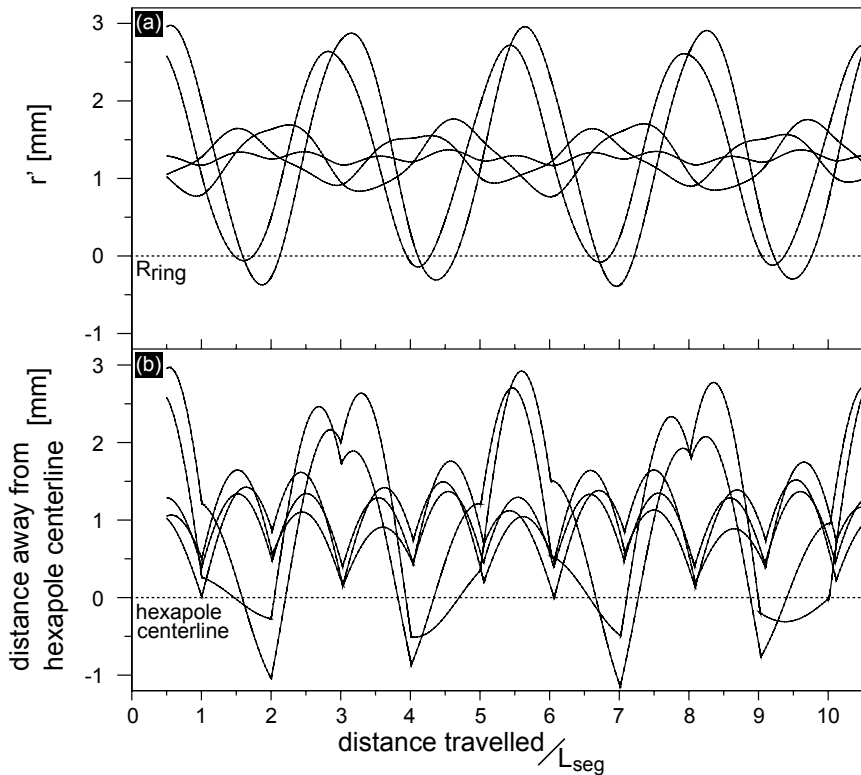


Figure 7.2: Various trajectories calculated for molecules ( $v_z=100$  m/s) moving through a ring consisting of 40 hexapoles (segments); the x-axis is plotted as the distance travelled divided by the length of a single segment,  $L_{\text{seg}}$ . The same trajectories are plotted in both graphs, but the position of the molecule is shown in (a) with respect to an (imaginary) circle with a radius of  $R_{\text{ring}}$ , and in (b) with respect to the hexapole centerline in which the molecules are located.

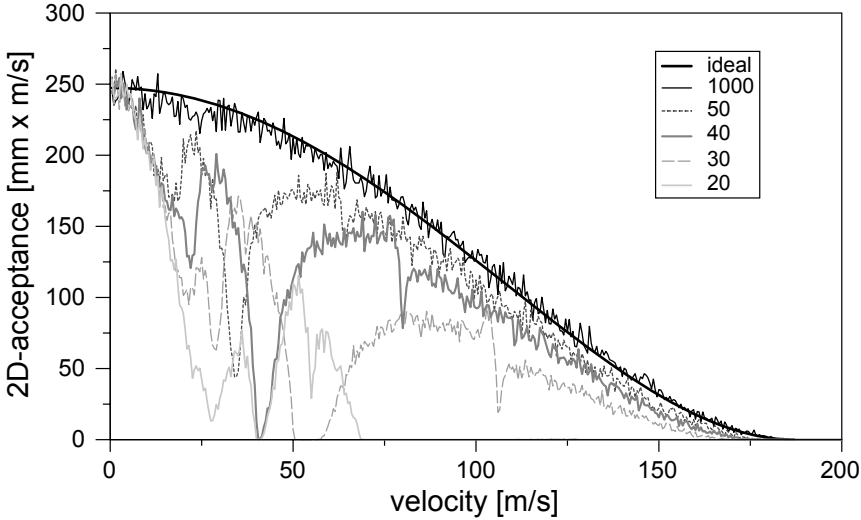


Figure 7.3: The acceptance in the horizontal plane of a ring composed of 20, 30, 40, 50 and 1000 segments is plotted as a function of forward velocity. A ring consisting out of 1000 straight hexapoles is essentially identical to the ideal case, following from Equation 7.3 (bold black line). Reducing the number of segments reduces the acceptance of the ring and additionally introduces stopbands.

to motional resonances arising at certain velocities, as discussed in Chapter 6\*.

Figure 7.3 shows the two dimensional acceptance as a function of longitudinal velocity for a ring composed out of 20, 30, 40, 50 and 1000 segments. The bold curve shows the acceptance one expects for an ideal ring given by:

$$\text{Acceptance} = \pi\omega (R_{\text{hex}} - r_{\text{equi}})^2 = \pi\omega \left( R_{\text{hex}} - \frac{v_{\phi}^2}{R_{\text{ring}}\omega^2} \right)^2 \quad (7.3)$$

where the equilibrium radius,  $r_{\text{equi}}$ , varies depending on the longitudinal velocity (see Chapter 4). Not surprisingly, the acceptance of a ring composed out of 1000 straight hexapoles is virtually the same as that of an ideal ring. When the number of segments is decreased it is seen that the acceptance at high velocities decreases, and that at certain velocities motional resonances occur (see Chapter 6). For instance, it is seen that for a ring composed of 40 segments, resonances emerge around  $v_{\phi} = 78.4$ ,  $39.2$  and  $19.6$  m/s, where the molecules

\*Note that in Chapter 6 the motional resonances arose since the confinement forces temporarily disappeared in the gaps. More generally, however, resonances are introduced whenever the confinement force is periodic – as is the case here.

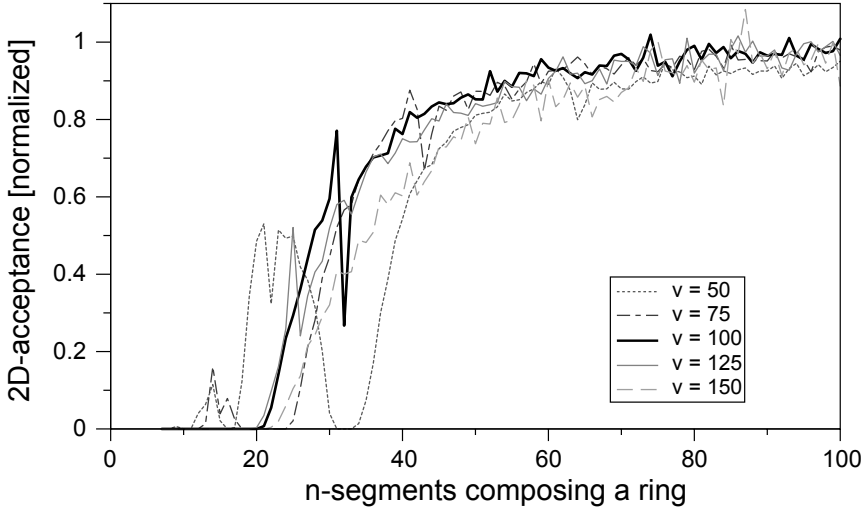


Figure 7.4: *The acceptance in the horizontal plane of a ring composed of  $n$ -segments for molecules moving with a forward velocity of 50, 75, 100, 125 and 150 m/s. The acceptance is normalized to that of an ideal ring ( $n_{seg} \rightarrow \infty$ ). Constructing a ring out of at least 40 straight hexapoles yields an acceptance  $> 0.6$  for velocities above 75 m/s.*

make  $\frac{1}{2}$ , 1 and  $1\frac{1}{2}$  oscillations in a single segment, respectively\*. With even fewer segments, the acceptance decreases dramatically; in fact for a ring composed of only 20 segments no molecules are retained for velocities higher than 70 m/s.

Figure 7.4 is a complementary graph to Figure 7.3 depicting the two dimensional acceptance for molecules moving with a longitudinal velocity of 50, 75, 100, 125 and 150 m/s as a function of  $n$ -segments comprising a ring. The acceptance has been normalized to the acceptance of an ideal ring ( $n_{seg} \rightarrow \infty$ ) at each corresponding velocity. Clearly more segments yields a better acceptance.

As a compromise between construction demands and the expected performance, we have decided to build a ring out of 40 straight hexapoles, each separated by 2 mm. Each segment will have a length of  $2\pi \times R_{ring}/40 = 39.2$  mm, which is large compared to the 8.5 mm required for bunching (see Chapter 5). For velocities above 80 m/s – the range of particular interest for future experiments – the molecules make less than half a betatron oscillation per segment, so no resonances are expected.

---

\*As mentioned earlier, no gaps are taken into account in these simulations. The effects of the gaps only serve to increase the strength of the stopbands that are already present, but will not alter their positions, nor introduce new stopbands.



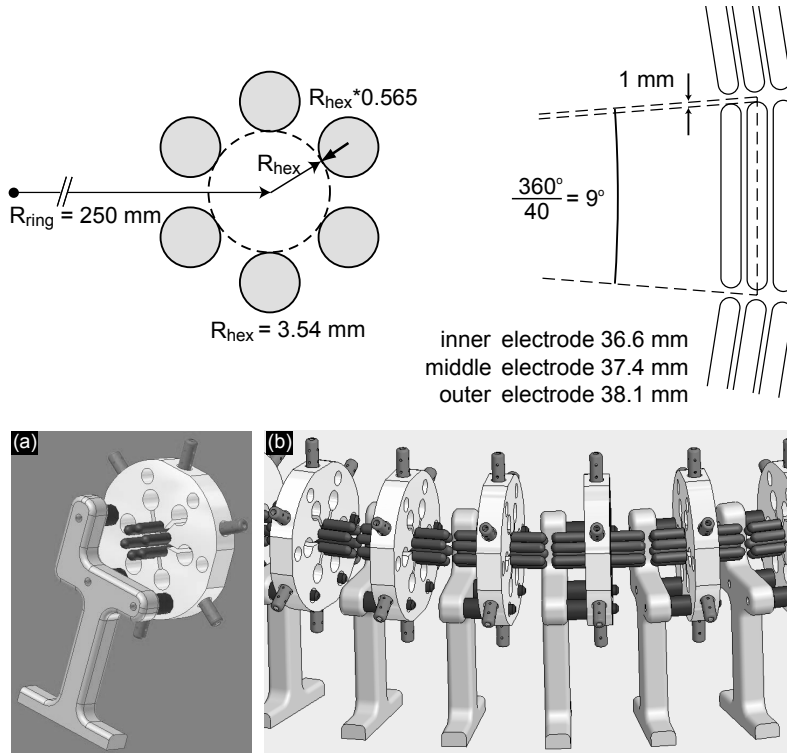


Figure 7.5: Dimensions of a new 40-hexapole synchrotron. Each hexapole is designed following the suggestions of Anderson [66] to approximate a more ideal field. The ring radius has been doubled, and there is a  $9^\circ$  angle between straight hexapoles. Electrodes are longer on the outside and shorter on the inside to assure a constant 2 mm gap between segments. Sketches of (a) a single hexapole unit and (b) a row of hexapoles is sketched below.

## 7.3 Current status

Some of the dimensions of the 40-hexapole synchrotron are summarized in Figure 7.5. The hexapoles are made by placing electrodes with a radius of 2 mm around a circle with a radius of 3.54 mm, following the suggestion of Anderson [66]. The ring radius is 250 mm. Each hexapole spans an angle of  $9^\circ$  of the ring. A difference of 1.5 mm between the lengths of the inner and outer electrodes is implemented to maintain a constant gap distance of 2 mm.

The 40 hexapoles are aligned in a two-step process. First, the highly-polished stainless steel electrodes are fitted into ceramic insulators carved with a hexapole geometry, similar to those used in the current two-piece set-up. The ceramic insulators are shaped such as to provide long pathways between

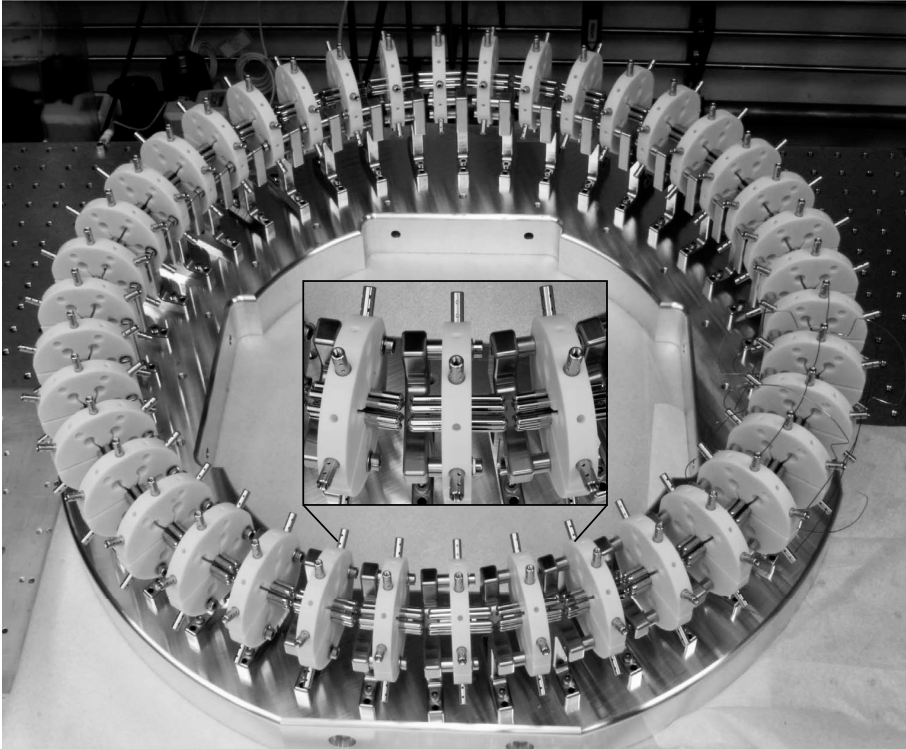


Figure 7.6: *Photograph of the assembled 40-hexapole synchrotron. The zoom-in shows three of the hexapoles.*

the electrodes to decrease the probability of electrical discharges happening along the surface of the ceramics. The electrodes are held in place by specially designed screws that also serve as voltage feedthroughs. The ceramic disk is clamped onto a stainless steel foot via three screws, as illustrated in the sketch in Figure 7.5(a). With the aid of a home-built alignment tool, each ceramic disk is adjusted such that the hexapole centerline has a pre-defined height and horizontal position with respect to the base of the foot. Thus regardless of the precision errors of individual ceramics, which can be large, each hexapole unit will be symmetrical. In a second step, the hexapole units are mounted onto the aluminium base plate. Using set pins to guide the feet into the drilled holes of the base plate results in a precision  $< 0.05$  mm [85]. A photograph of the newly assembled ring\* is shown in Figure 7.6 along with a zoom-in of three of the hexapoles.

---

\*This ring was designed and constructed by André van Roij with help from Henrik Haak, Hendrick L. Bethlem and myself, and is currently being tested by Peter Zieger.

## 7.4 Conclusion

In this Chapter, a design for a synchrotron consisting out of 40 straight hexapoles was presented. The synchrotron was constructed out of straight hexapoles to avoid many technical difficulties. Although this does decrease the acceptance, it is only by  $< 40\%$  for velocities above 80 m/s ( $E_{\text{kin}} \simeq 5 \text{ cm}^{-1}$ ). At these velocities, the molecules make less than half a betatron oscillation per segment, thus avoiding any resonances. Each hexapole is 39 mm long such that the ring has a circumference of 1.57 m. The longitudinal acceptance scales inversely with the square root of the length of a single segment, and hence will be 3 times larger than the two-piece synchrotron discussed in the previous chapters. The maximum velocity that can be stored is 170 m/s ( $E_{\text{kin}} \simeq 24 \text{ cm}^{-1}$ ). In this way, collisions with energies between  $10 \text{ cm}^{-1}$  and  $48 \text{ cm}^{-1}$  can be investigated; this would allow transitions from the  $|J, K\rangle = |1, 1\rangle$  to the  $|2, 1\rangle$  and the  $|2, 2\rangle$  states to be studied.

The synchrotron has been designed to be able to simultaneously store 20 packets of molecules going clockwise and counter-clockwise. As mentioned in the introduction, injecting packets at a repetition frequency of 10 Hz will fill the ring with 20 packets moving clockwise and 20 packets moving counter-clockwise after 2 seconds. From this point on, every packet will be stored from injection to detection for 2 seconds. This means that for a packet moving at, for instance, a longitudinal velocity of 100 m/s, it will make 127 round trips in this time. Since the number of collisions scales as the number of packets squared, this packet will have had over 5000 encounters with counter-propagating packets.



# Bibliography

- [1] K.-J. Kügler, W. Paul, and U. Trinks, "A magnetic storage ring for neutrons," *Phys. Lett. B*, vol. 72, p. 422, 1978.
- [2] J. A. Sauer, M. D. Barrett, and M. S. Chapman, "Storage ring for neutral atoms," *Phys. Rev. Lett.*, vol. 87, p. 270401, 2001.
- [3] F. M. H. Cromptoets, H. L. Bethlem, R. T. Jongma, and G. Meijer, "A prototype storage ring for neutral molecules," *Nature*, vol. 411, p. 174, 2001.
- [4] H. Nishimura, G. Lambertson, J. G. Kalnins, and H. Gould, "Feasibility of a synchrotron storage ring for neutral polar molecules," *Rev. Sci. Instrum.*, vol. 74, p. 3271, 2003.
- [5] F. M. H. Cromptoets, H. L. Bethlem, and G. Meijer, "A storage ring for neutral molecules," *Adv. At. Mol. Opt. Phys.*, vol. 52, p. 209, 2005.
- [6] G. Scoles, *Atomic and molecular beam methods, vol. 1*. New York: Oxford University Press, 1988.
- [7] S. R. Gandhi and R. B. Bernstein, "Focusing and state selection of  $\text{NH}_3$  and  $\text{OCS}$  by the electrostatic hexapole via first- and second-order Stark effects," *J. Chem. Phys.*, vol. 87, p. 6457, 1987.
- [8] S. Stolte, "Aiming the molecular arrow," *Nature*, vol. 353, p. 391, 1991.
- [9] K. Schreel and J. J. ter Meulen, "State-to-state scattering of oriented  $\text{OH}$ ," *J. Phys. Chem. A*, vol. 101, p. 7639, 1997.
- [10] G. Hall, K. Liu, M. J. McAuliffe, C. F. Giese, and W. R. Gentry, "State-to-state vibrational excitation of  $\text{I}_2$  in collisions with  $\text{He}$ ," *J. Chem. Phys.*, vol. 81, p. 5577, 1984.
- [11] R. G. Macdonald and K. Liu, "State-to-state integral cross sections for the inelastic scattering of  $\text{CH}(X^2\Pi)+\text{He}$ : Rotational rainbow and orbital alignment," *J. Chem. Phys.*, vol. 91, p. 821, 1989.

- [12] D. M. Sonnenfroh, R. G. Macdonald, and K. Liu, "A crossed-beam study of the state-resolved integral cross sections for the inelastic scattering of OH( $X^2\Pi$ ) with CO and N<sub>2</sub>," *J. Chem. Phys.*, vol. 94, p. 6508, 1991.
- [13] D. Skouteris, D. E. Manolopoulos, W. Bian, H.-J. Werner, L.-H. Lai, and K. Liu, "van der Waals interactions in the Cl+HD reaction," *Science*, vol. 286, p. 1713, 1999.
- [14] R. T. Skodje, D. Skouteris, D. E. Manolopoulos, S.-H. Lee, F. Dong, and K. Liu, "Resonance-mediated chemical reaction: F+HD  $\rightarrow$  HF+D," *Phys. Rev. Lett.*, vol. 85, p. 1206, 2000.
- [15] N. Balakrishnan, A. Dalgarno, and R. C. Forrey, "Vibrational relaxation of CO by collisions with <sup>4</sup>He at ultracold temperatures," *J. Chem. Phys.*, vol. 113, p. 621, 2000.
- [16] J. M. Hutson and P. Soldán, "Molecular collisions in ultracold atomic gases," *Int. Rev. Phys. Chem.*, vol. 26, p. 1, 2007.
- [17] E. Bodo and F. A. Gianturco, "Collisional quenching of molecular ro-vibrational energy by He buffer loading at ultralow energies," *Int. Rev. Phys. Chem.*, vol. 25, p. 313, 2006.
- [18] R. V. Krems, "Cold controlled chemistry," *Phys. Chem. Chem. Phys.*, vol. 10, p. 4079, 2008.
- [19] M. D. Di Rosa, "Concept, candidates, and supporting hyperfine-resolved measurements of rotational lines in the A-X(0,0) band of CaH," *Eur. Phys. J. D.*, vol. 31, p. 395, 2004.
- [20] J. M. Doyle, B. Friedrich, J. Kim, and D. Patterson, "Buffer-gas loading of atoms and molecules into a magnetic trap," *Phys. Rev. A*, vol. 52, p. R2515, 1995.
- [21] J. D. Weinstein, R. deCarvalho, T. Guillet, B. Friedrich, and J. M. Doyle, "Magnetic trapping of calcium monohydride molecules at millikelvin temperatures," *Nature*, vol. 395, p. 148, 1998.
- [22] S. Y. T. van de Meerakker, H. L. Bethlem, and G. Meijer, "Taming molecular beams," *Nature Phys.*, vol. 4, p. 595, 2008.
- [23] J. J. Gilijamse, S. Hoekstra, S. Y. T. van de Meerakker, G. C. Groenenboom, and G. Meijer, "Near-threshold inelastic collisions using molecular beams with a tunable velocity," *Science*, vol. 313, p. 1617, 2006.
- [24] E. Rutherford, "The scattering of  $\alpha$  and  $\beta$  particles by matter and the structure of the atom," *Philos. Mag.*, vol. 6, p. 1, 1911.

- 
- [25] E. Rutherford, "Atomic projectiles and their collisions with light atoms," *Science*, vol. 50, p. 467, 1919.
- [26] E. Rutherford, "Address of the president, Sir Ernest Rutherford, O.M., at the anniversary meeting, November 30, 1927," *Proc. Roy. Soc. A*, vol. 117, p. 300, 1928.
- [27] E. O. Lawrence and M. S. Livingston, "The production of high speed light ions without the use of high voltages," *Phys. Rev.*, vol. 40, p. 19, 1932.
- [28] J. D. Cockcroft and E. T. S. Walton, "Experiments with high velocity positive ions," *Proc. Roy. Soc. A*, vol. 129, p. 477, 1930.
- [29] J. D. Cockcroft and E. T. S. Walton, "Artificial production of fast protons," *Nature*, vol. 129, p. 242, 1932.
- [30] J. D. Cockcroft and E. T. S. Walton, "Disintegration of lithium by swift protons," *Nature*, vol. 129, p. 649, 1932.
- [31] J. D. Cockcroft and E. T. S. Walton, "Experiments with high velocity positive ions II. The disintegration of elements by high velocity protons," *Proc. Roy. Soc. A*, vol. 137, p. 229, 1932.
- [32] G. Ising, "Prinzip einer Methode zur Herstellung von Kanalstrahlen hoher Voltzahl," *Arkiv. Mat. Astron. Fysik*, vol. 18, p. 45, 1925.
- [33] R. Wideröe, "Über ein neues Prinzip zur Herstellung hoher Spannungen," *Arch. f. Elektrot.*, vol. 21, p. 387, 1928.
- [34] E. O. Lawrence, *Nobel Lectures, Physics 1922-1941*, ch. The evolution of the cyclotron, p. 430. Amsterdam: Elsevier Publishing Company, 1965.
- [35] Thomas Jefferson National Accelerator Facility – Office of Science Education, "Glossary Item: Cyclotron." 23 September 2008, <http://education.jlab.org/glossary/cyclotron.html>.
- [36] M. S. Livingston, "The cyclotron I.," *J. Appli. Phys.*, vol. 15, p. 2, 1944.
- [37] E. O. Lawrence and M. S. Livingston, "The production of high speed protons without the use of high voltages," *Phys. Rev.*, vol. 38, p. 834, 1931.
- [38] M. S. Livingston, "High-speed hydrogen ions," *Phys. Rev.*, vol. 42, p. 441, 1932.
- [39] S. Kullander, "Accelerators and Nobel Laureates." 28 August 2001, [http://nobelprize.org/nobel\\_prizes/physics/articles/kullander/](http://nobelprize.org/nobel_prizes/physics/articles/kullander/).

- [40] E. O. Lawrence, "The medical cyclotron of the William H. Crocker Radiation Laboratory," *Science*, vol. 90, p. 407, 1939.
- [41] S. Y. Lee, *Accelerator Physics*. Singapore: World Scientific, second ed., 2004.
- [42] E. M. McMillan, "The synchrotron – a proposed high energy particle accelerator," *Phys. Rev.*, vol. 68, p. 143, 1945.
- [43] V. I. Veksler, "A new method of acceleration of relativistic particles," *J. Phys. (USSR)*, vol. 9, p. 153, 1945.
- [44] J. R. Richardson, K. R. MacKenzie, E. J. Lofaren, and B. T. Wright, "Frequency modulated cyclotron," *Phys. Rev.*, vol. 69, p. 669, 1946.
- [45] W. M. Brobeck, E. O. Lawrence, K. R. MacKenzie, E. M. McMillan, R. Serber, D. C. Sewell, K. M. Simpson, and R. L. Thornton, "Initial performance of the 184-inch cyclotron of the University of California," *Phys. Rev.*, vol. 71, p. 449, 1947.
- [46] V. Z. Peterson, "Mesons produced in proton-proton collisions," *Phys. Rev.*, vol. 79, p. 407, 1950.
- [47] M. L. Oliphant, "The cyclosynchrotron," *Nature*, vol. 165, p. 466, 1950.
- [48] D. Bohm and L. Foldy, "The theory of the synchrotron," *Phys. Rev.*, vol. 70, p. 249, 1946.
- [49] F. K. Goward and D. E. Barnes, "Experimental 8 MeV synchrotron for electron acceleration," *Nature*, vol. 158, p. 413, 1946.
- [50] L. J. Haworth, "Foreward of The Review of Scientific Instruments," *Rev. Sci. Instrum.*, vol. 24, p. 723, 1953.
- [51] E. D. Courant, M. S. Livingston, and H. S. Snyder, "The strong-focusing synchrotron – a new high energy accelerator," *Phys. Rev.*, vol. 88, p. 1190, 1952.
- [52] D. W. Kerst, F. T. Cole, H. R. Crane, L. W. Jones, L. J. Laslett, T. Ohkawa, A. M. Sessler, K. R. Symon, K. M. Terwilliger, and N. V. Nilsen, "Attainment of very high energy by means of intersecting beams of particles," *Phys. Rev.*, vol. 102, p. 590, 1956.
- [53] C. Rubbia, *Nobel Lectures, Physics 1981-1990*, ch. Experimental observation of the intermediate vector bosons  $W^+$ ,  $W^-$ , and  $Z^0$ , p. 240. Singapore: World Scientific Publishing Company, 1993. Editors: T. Frängsmyr and G. Ekspång.



- 
- [54] European Organization for Nuclear Research (CERN), “The Large Hadron Collider.” 23 September 2008, <http://public.web.cern.ch/public/en/LHC/LHC-en.html>.
- [55] H. L. Bethlem, M. R. Tarbutt, J. Küpper, D. Carty, K. Wohlfart, E. A. Hinds, and G. Meijer, “Alternating gradient focusing and deceleration of polar molecules,” *J. Phys. B*, vol. 39, p. R263, 2006.
- [56] A. P. Banford, *The transport of charged particle beams*. London: E. & F. N. Spon Limited, 1966.
- [57] A. J. Lichtenberg, *Phase-space dynamics of particles*. New York: Jon Wiley & Sons, 1969.
- [58] H. L. Bethlem and G. Meijer, “Production and application of translationally cold molecules,” *Int. Rev. Phys. Chem.*, vol. 22, p. 73, 2003.
- [59] W. H. Wing, “Electrostatic trapping of neutral atomic particles,” *Phys. Rev. Lett.*, vol. 45, p. 631, 1980.
- [60] S. Y. T. van de Meerakker, H. L. Bethlem, and G. Meijer, *Low Temperatures and cold molecules*, ch. Manipulation of molecules with electric fields. London: Imperial College Press, 2008. Editor: I. W. M. Smith.
- [61] P. R. Bunker and P. Jensen, *Fundamentals of molecular symmetry*. London: Institute of Physics Publishing, 2005.
- [62] L. Fusina and S. N. Murzin, “Inversion spectrum and ground state spectroscopic parameters of  $^{14}\text{ND}_3$ ,” *J. Mol. Spec.*, vol. 167, p. 464, 1994.
- [63] S. G. Kukolich, “Measurement of ammonia hyperfine structure with a two-cavity Maser,” *Phys. Rev.*, vol. 156, p. 83, 1967.
- [64] J. van Veldhoven, R. T. Jongma, B. Sartakov, W. A. Bongers, and G. Meijer, “Hyperfine structure of  $\text{ND}_3$ ,” *Phys. Rev. A*, vol. 66, p. 032501, 2002.
- [65] J. Reuss, *Atomic and molecular beam methods, vol. 1*, ch. State selection by nonoptical methods. New York: Oxford University Press, 1988. Editor: G. Scoles.
- [66] R. W. Anderson, “Tracks of symmetric top molecules in hexapole electric fields,” *J. Phys. Chem. A*, vol. 101, p. 7664, 1997.
- [67] D. A. Dahl, “Simion 3D version 6.0,” tech. rep., Idaho National Engineering Laboratory, Idaho Falls (USA), 1995.
- [68] R. T. Jongma, T. Rasing, and G. Meijer, “Two-dimensional imaging of metastable CO molecules,” *J. Chem. Phys.*, vol. 102, p. 1925, 1995.

- [69] J. B. Fenn, *Atomic and molecular beam methods, vol. 1*, ch. Forward. New York: Oxford University Press, 1988. Editor: G. Scoles.
- [70] D. H. Levy, "The spectroscopy of very cold gases," *Science*, vol. 214, p. 263, 1981.
- [71] H. Haberland, U. Buck, and M. Tolle, "Velocity distribution of supersonic nozzle beams," *Rev. Sci. Instrum.*, vol. 56, p. 1712, 1985.
- [72] E. A. Cornell and C. E. Wieman, "Nobel Lecture: Bose-Einstein condensation in a dilute gas, the first 70 years and some recent experiments," *Rev. Mod. Phys.*, vol. 74, p. 875, 2002.
- [73] W. Ketterle, "Nobel Lecture: When atoms behave as waves: Bose-Einstein condensation and the atom laser," *Rev. Mod. Phys.*, vol. 74, p. 1131, 2002.
- [74] H. L. Bethlem, G. Berden, and G. Meijer, "Decelerating neutral dipolar molecules," *Phys. Rev. Lett.*, vol. 83, p. 1558, 1999.
- [75] H. L. Bethlem, F. M. H. Crompvoets, R. T. Jongma, S. Y. T. van de Meerakker, and G. Meijer, "Deceleration and trapping of ammonia using time-varying electric fields," *Phys. Rev. A*, vol. 65, p. 053416, 2002.
- [76] H. L. Bethlem, G. Berden, A. J. A. van Roij, F. M. H. Crompvoets, and G. Meijer, "Trapping neutral molecules in a traveling potential well," *Phys. Rev. Lett.*, vol. 84, p. 5744, 2000.
- [77] F. M. H. Crompvoets, R. T. Jongma, H. L. Bethlem, A. J. A. van Roij, and G. Meijer, "Longitudinal focusing and cooling of a molecular beam," *Phys. Rev. Lett.*, vol. 89, p. 093004, 2002.
- [78] M. N. R. Ashfold, R. N. Dixon, N. Little, R. J. Stickland, and C. M. Western, "The  $\tilde{B}^1E$  state of ammonia: Sub-Doppler spectroscopy at vacuum ultraviolet energies," *J. Chem. Phys.*, vol. 89, p. 1754, 1988.
- [79] W. C. Wiley and I. H. McLaren, "Time-of-flight mass spectrometer with improved resolution," *Sci. Rev. Instrum.*, vol. 26, p. 1150, 1955.
- [80] J. Küpper, U. Hoppe, H. Junkes, C. Tschentscher, C. Kuhlisch, and A. Stanik, "Cold molecules data acquisition - KouDA." 2003 - 2007, <http://kouda.cold-molecules.info>.
- [81] M. Gupta and D. Herschbach, "A mechanical means to produce intense beams of slow molecules," *J. Phys. Chem. A*, vol. 103, p. 10670, 1999.
- [82] S. Y. T. van de Meerakker, N. Vanhaecke, and G. Meijer, "Stark deceleration and trapping of OH radicals," *Annu. Rev. Phys. Chem.*, vol. 57, p. 159, 2006.

- [83] R. L. Bhattacharjee, L. H. Johnston, G. R. Sudhakaran, and J. C. Sarker, "Submillimeter laser Stark spectroscopy of  $^{14}\text{ND}_3$ ," *J. Mol. Spec.*, vol. 138, p. 38, 1989.
- [84] W. H. Press, B. P. Flannery, S. A. Teukolsky, and W. T. Vetterling, *Numerical recipes: the art of scientific computing*. Cambridge: Cambridge University Press, 1986.
- [85] H. Haak. private communications.
- [86] T. H. Maiman, "Stimulated optical radiation in ruby," *Nature*, vol. 187, p. 493, 1960.
- [87] C. H. Townes, *A century of Nature: Twenty-one discoveries that changed science and the world*, ch. "The first laser", p. 107. Chicago: University of Chicago Press, 2003. Editors: L. Garwin and T. Lincoln.
- [88] Nobel Web (of the Nobel Foundation), "Laser challenge: Everyday use of laser." 23 September 2008, [http://nobelprize.org/educational\\_games/physics/laser/facts/use.html](http://nobelprize.org/educational_games/physics/laser/facts/use.html).
- [89] W. C. Röntgen, "On a new kind of rays," *Nature*, vol. 53, p. 274, 1896.
- [90] J. Pietzsch, "A helping hand from the media." 23 September 2008, [http://nobelprize.org/nobel\\_prizes/physics/laureates/1901/perspectives.html](http://nobelprize.org/nobel_prizes/physics/laureates/1901/perspectives.html).
- [91] T. Berners-Lee, "Information management: A proposal." 1989, <http://www.w3.org/History/1989/proposal.html>.
- [92] European Organization for Nuclear Research (CERN), "The website of the world's first-ever web server." 23 September 2008, <http://info.cern.ch/>.
- [93] G. Ekspong, "The dual nature of light as reflected in the Nobel archives." 02 December 1999, [http://nobelprize.org/nobel\\_prizes/physics/articles/ekspong/index.html](http://nobelprize.org/nobel_prizes/physics/articles/ekspong/index.html).



## Hoofdstuk 8

# Samenvatting

In dit proefschrift zijn experimenten beschreven aan de eerste synchrotron voor neutrale moleculen. Deze synchrotron wordt gevormd door twee in een halve cirkel gebogen hexapolen die op 2 mm afstand van elkaar zijn geplaatst. De kromtestraal van de hexapolen is 125 mm. Door op de zes elektroden van de hexapolen om en om positieve en negatieve spanningen te zetten ontstaat een elektrisch veld dat in het midden van de hexapool nul is en dat toeneemt naar de elektroden toe. Een polair molecuul waarvan het elektrische dipoolmoment anti-parallel aan het elektrische veld staat ondervindt een kracht naar het minimum van het elektrische veld toe. Wanneer dit molecuul met een niet al te hoge snelheid tangentieel geïnjecteerd wordt in de ring, dan zal het de kromming van de hexapool volgen en een cirkelbaan afleggen. De straal van deze cirkel hangt af van de snelheid van het molecuul; hoe hoger de snelheid, hoe groter de straal. Moleculen met een te hoge snelheid kunnen niet ingevangen worden. Wanneer een constante spanning wordt aangelegd, ondervinden de moleculen weliswaar in de radieële en in de verticale richting een kracht die hen bij elkaar houdt, maar in de voorwaartse richting is dit niet het geval. Dit zorgt ervoor dat een geïnjecteerd compact wolkje moleculen na een korte tijd de hele ring zal vullen. Om dit tegen te gaan worden de spanningen omgeschakeld op het moment dat de moleculen zich in de 2 mm spleet tussen de twee halve ringen bevinden. Dit wordt op een dusdanige manier gedaan, dat de moleculen eerst afgeremd en dan versneld worden. Een molecuul dat zich precies in het midden tussen de twee halve ringen bevindt als de spanningen worden geschakeld wordt evenveel afgeremd als versneld, en zal zijn oorspronkelijke snelheid behouden. Een molecuul dat een beetje vooruit is zal echter meer worden afgeremd dan versneld, terwijl een molecuul dat een beetje achter is meer zal worden versneld dan afgeremd. Op deze manier wordt het wolkje moleculen bij elkaar gehouden. Omdat de spanningen *synchroon* met de beweging van de moleculen worden geschakeld noemen we deze opslagring een *synchrotron*.

Een synchrotron biedt unieke mogelijkheden voor een aantal toekomstige

experimenten. Door meerdere pakketjes moleculen in beide richtingen in de ring te laten rondvliegen, bijvoorbeeld, kunnen botsingen tussen moleculen als functie van hun snelheid worden bestudeerd. Deze en andere mogelijke toepassingen van de synchrotron worden beschreven in Hoofdstuk 1. In Hoofdstuk 2 wordt de ontstaansgeschiedenis van synchrotrons voor geladen deeltjes belicht en wordt ingegaan op de verschillen en overeenkomsten tussen synchrotrons voor geladen en ongeladen deeltjes. In Hoofdstuk 3 wordt de bundelmachine die gebruikt wordt om de moleculen in de synchrotron te injecteren beschreven. In Hoofdstuk 4 wordt de transversale en in Hoofdstuk 5 de voorwaartse beweging van de moleculen in de synchrotron bestudeerd en worden metingen gepresenteerd waarin één of meerdere pakketjes moleculen tot honderd keer rondgaan in de ring. In Hoofdstuk 6 worden metingen gepresenteerd waarbij de snelheid van de geïnjecteerde moleculen tussen 60 en 90 m/s wordt gevarieerd. Er wordt getoond dat resonante versterking van de amplitude van de transversale beweging - een ongewenst proces waardoor moleculen verloren kunnen gaan uit de synchrotron - kan worden voorkomen indien de spanning op een bepaalde manier wordt aangepast met de snelheid van de moleculen. Tot slot wordt in Hoofdstuk 7 een eenvoudig ontwerp gepresenteerd voor een nieuwe synchrotron waarin veertig verschillende pakketjes moleculen kunnen worden opgesloten.

# Chapter 9

## Summary

Here it is, my chance to summarize to everyone what exactly I have been doing with my time for the last four years. I have worked on a novel synchrotron to help answer fundamental physics questions. When I tell people this, I usually get (in addition to a blank stare) three questions in return: (i) what is a synchrotron, (ii) why is your synchrotron so novel, and (iii) why bother? Allow me to answer the last question first.

### **Why bother?**

The third question I am invariably asked is by far the hardest to approach: Why should one care about fundamental research, and how could some tiny, minute detail affect the life of an average person? Well, the answer could be 'in many ways', and at the same time the answer could be 'not at all'. I cannot directly answer that question. How can I be so vague (and maybe so annoying)? It is because fundamental questions are rarely posed for the sole benefit of one person. Fundamental research is, as the name suggests, a study of the fundamental truths underlying every aspect of our world. All in all, society would undoubtedly suffer without the pursuit of basic research. Estimating the success of fundamental research, however, is difficult, as it cannot be quantified in the same way that, for instance, a balance sheet can quantify the financial success of a company. Hence it is sometimes difficult for the public to become enthusiastic about fundamental research. Let us take for an example the investigation into the emission spectra of ruby. To most, the money invested into such an experiment would seem like a loss, or as a whimsical, trivial question that some eccentric scientist is pursuing and can be, at best, simply tolerated. However, it was exactly this information that led to the creation of the first laser ('Light Amplification by Stimulated Emission of Radiation') reported by Theodore Maiman in 1960 [86]. The technique was initially greeted with skepticism, even from scientists, resulting in the rejection of Maiman's short report

from the esteemed journal of Physical Review Letters [87]. Today, of course, lasers are a common tool used in countless ways – not only in science and medicine, but also in construction and in everyday applications such as your CD and DVD players [88].

Both the resulting information and the various demanding techniques developed for physics experiments can benefit society in ways that could have never been foreseen. For example, X-rays were first observed by Wilhelm Conrad Röntgen in 1895, somewhat by accident as he was studying how cathode-ray tubes emit light. He noticed a glowing screen in his laboratory some distance away from (and not part of) his experiment. After a few intense weeks spent eating and sleeping in his laboratory, Röntgen finally identified the source of this glow: a new kind of invisible rays (generated by the impact of the cathode rays on the glass vacuum tube), which he called X-rays\*. He noted that the screen glowed even if cardboard, wood, copper, or aluminium was placed in between the (X-ray) source and the screen. Seeing that as the X-rays could pass through metal, his curiosity naturally led him to try imaging flesh. He took the first X-ray image of a human body part<sup>†</sup>, as we are familiar with today, of his wife's hand, which clearly showed her bones and wedding ring as well as a faint outline of the surrounding tissue [89]. Röntgen received the very first Nobel Prize in Physics in 1901 for this discovery. Today, X-ray machines are commonplace in medicine and dentistry, and can also be found at most airports to inspect luggage.

This list goes on and on; in fact, sometimes even the byproducts of physics research can make their way into mainstream usage. For instance, the idea by Tim Berners-Lee at CERN to connect personal computers with hypertext and computer networking to allow physicists to share all the computer-stored information, regardless of a person's actual (global) location gave birth to the World Wide Web (or just the Web) [91]. Although the Web's conception began as a tool for data exchange between scientists, today there are hundreds of millions of users exchanging all sorts of information on upwards of 80 million websites [92]. In fact, most households that now buy a computer are probably more interested in using it to log in to the Web than to use the computer for its processing capabilities.

So the answer to the question why bother is clearly: why not. But before you start thinking that scientists only make breakthrough discoveries by accident (or that they are just lucky), I want to make clear that we do have a few

---

\*Röntgen referred to the radiation as "X", to indicate that it was an unknown type of radiation. The name more or less stuck, however in some German speaking countries X-rays are still sometimes referred to as Röntgen rays.

<sup>†</sup>As circumstance would have it, this image – which Röntgen sent to a former student, who in turn, passed it along to a professor of physics in Prague, who in turn, passed it along to his father, the editor of Vienna's leading daily newspaper (Die Presse) – sparked a front-page story under the headline "A sensational discovery" appearing on Monday, January 6<sup>th</sup>, 1896. Within days, the news of X-rays, and ideas for their possible applications, had spread around the world [90].



---

ideas and set goals of what results should come out of our experiments. Allow me now to briefly explain my experiment and the goals of my research.

### **What is a synchrotron?**

Let us return to answering the first question(s) I regularly receive from friends and family about my work: What is a synchrotron? First I ask you to recall your high school science classes, in which you were surely introduced to the early model of an atom. In this model, a negatively charged electron revolves around a positively charged nucleus. This basic example illustrates how a positive charge can exert an invisible, attractive force on a negative charge – this is an electric force. Charged particles moving through an electric field will experience a force, and in this way electric fields can be tailored such as to steer (or speed up or slow down) charged particles along particular tracks. Unless the track is infinitely long, the particles will at some point leave the field region and will no longer be influenced by the electric fields. In order to keep the particles in an electric field, one can guide the particles in a circle, thus repetitively applying the electric forces on the particles indefinitely. A synchrotron is a device that does just that: electric and/or magnetic fields provide forces over every round trip for accelerating and steering charged particles in a (circular) track that can be miles-long. The electric fields must be switched on in synchronization with the position (and velocity) of the particles as they move around the ring – hence the name synchrotron.

### **What makes my synchrotron so novel?**

Admittedly, this question is a bit more subjective. I am not the first physicist to perform experiments in, or using, a synchrotron. In fact, scientists around the world have been performing experiments with accelerated charged particles in synchrotron facilities for over 60 years. Accelerated particles can have an incredibly large amount of energy. If particles are accelerated and then made to smash into other accelerated particles (moving in the opposite direction), all of this (high) energy is released in the collision event. In the re-arrangement of the energy entirely new particles can be observed, such as quarks. Such high-energy reactions occurred in the first few (micro)seconds after the big bang. Hence re-creating such conditions in a laboratory is essentially like building a time machine that allows us to look back to the beginning of the universe.

I didn't do this.

In this thesis, the other end of the energy limit is investigated: I use the same principles used in high-energy facilities to accelerate charged particles to instead decelerate neutral molecules. I also want to study collisions, but at low energies. I can benefit from the repetitive actions of a synchrotron, in order to allow molecules to encounter each other many times as they revolve

(in two opposite propagation directions) around the ring. In my experiment, the molecules move along a circular path with a circumference of a mere 80 cm in the molecular synchrotron – I use the word 'mere' in comparison to the 27 km circumference of the largest high-energy synchrotron collider located at CERN. Don't let the smaller size fool you though, manipulating neutral molecules is intrinsically more difficult to achieve than the manipulation of charged particles, which I will briefly explain in the next section.

Furthermore, pushing to lower energy limits in a synchrotron analogue will open a new territory for potential discoveries, and traditionally new energy frontiers lead to new and exciting breakthroughs in physics. For instance, unusual events can occur between colliding molecules with low energies that may result in a "new" molecular species or complex that would otherwise be impossible to form or observe. Studying collisions at such low energies yields precise information about when and how chemical reactions between molecules occur. Knowledge of the exact amount of energy needed to cause a chemical reaction could then lead to full control over said reaction. Moreover, the results of collisions between low-energy molecules can sometimes be better described in a model as diffracted waves than as classical billiard balls – much like the dual nature of a photon (light) [93]. The gray area between these two descriptions has led to many different theories being proposed as to what could result in low energy collisions. However, the experiments in low (enough) energy regimes required to provide corroborating proof of one theory over another remain largely elusive. Conducting such trials in a molecular synchrotron is the long-term goal behind my research.

## 9.1 How does one control neutral molecules?

Until recently, it was required that particles possessed a definite charge to interact with the fields, much like in my earlier example of how (negative) electrons "circle" around a (positive) nucleus in an atom. A molecule is any combination of two or more atoms chemically bonded together. If a molecule's shape is such that all the electrons in all its constituent atoms are unevenly distributed, the molecule will have what is known as a dipole moment; such molecules are often referred to as polar molecules. This leads to one end of the molecule having a slightly more positive charge, while the other end has a slightly more negative charge. Note that the molecule is still electrically neutral – we are only discussing the matter of where the charges in the molecule are concentrated. In my thesis, I worked with deuterated ammonia,  $\text{ND}_3$ , a polar molecule. The  $\text{ND}_3$  molecule has three N-D bonds and two lone electrons pointing away from the bonds (in an approximately tetrahedral configuration). This means that a part of the molecule is particularly electron rich (negatively charged) and part of the molecule is particularly electron poor (positively charged), resulting in a dipole moment across the ammonia molecule. This dipole moment can interact

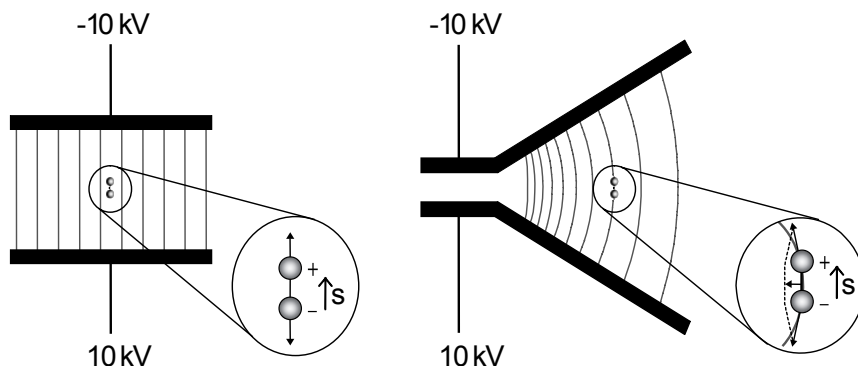


Figure 9.1: A polar molecule in a homogeneous and an inhomogeneous electric field. The net force on the left-hand molecule is zero, whereas the net force on the right-hand molecule is pointing towards higher field regions.

with an external electric field.

Let us look at a polar molecule that is located in a homogeneous electric field, as depicted on the left-hand side in Figure 9.1. Naturally the positive charge distribution is attracted towards the negative pole, and vice-versa, the negative charge distribution is attracted towards the positive pole. These forces have the same magnitude but are in opposite directions, thus the sum is zero, i.e., a polar molecule experiences no net force in an area of an homogeneous electric field.

Let us now look at a polar molecule that is located in an inhomogeneous electric field, as depicted on the right-hand side in Figure 9.1. Again the positive charge distribution is attracted towards the negative pole, and the negative charge distribution is attracted towards the positive pole. However, in this case the electric field lines are curved. This means that the attractive forces, which are tangent to the curved field lines, now have a horizontal component in addition to a vertical component. Thus the sum of these two forces does not cancel, but rather a small component of the force remains. For instance, the dipole of the molecule in the Figure is orientated (with respect to the electric field) such that the molecule experiences a force towards the high field region; in this case these molecules are referred to as *high-field-seeking* (hfs) molecules. If the molecule's orientation were turned around, then the molecule would experience a force towards the low field region; in this case these molecules are referred to as *low-field-seeking* (lfs) molecules. Admittedly these forces are some eight to ten orders of magnitude weaker than those experienced by charged particles in the same field, however they are sufficient to manipulate molecules, which is all that matters in our case.

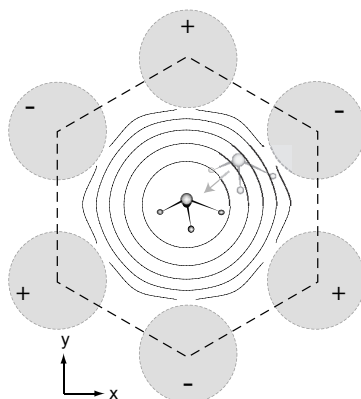


Figure 9.2: A sketch depicting a  $\text{ND}_3$  molecule inside a hexapole. The (alternating) voltages applied on adjacent hexapole electrodes create an electric field that results in a force towards lower electric field areas on a lfs  $\text{ND}_3$ ; the lowest field is located at the hexapole's center.

## 9.2 A synchrotron for neutral molecules

The idea behind the synchrotron is straight forward: to keep molecules confined in a ring by applying electric fields. In other words, the revolving molecules must be confined in three directions. Let us begin by examining the two in-plane directions,  $(x,y)$ , as illustrated in Figure 9.2. Imagine first just drawing a hexagon on a piece of paper. Now, in order to approximate this geometry to make an electrostatic hexapole, we place six rods over the six vertices of the hexagon, i.e., these rods are set equidistantly around a circle. Applying (alternating) positive and negative voltages to adjacent rods creates an electric field that is highest closest to the rods and zero at the middle of the hexapole (at the origin of the circle); contour lines of equal electric field strength are shown in Figure 9.2.

If a lfs molecule is placed into an electric field, it feels a force, as the name suggests, towards the lowest fields – in other words the molecule 'seeks' out the lowest electric field. Thus, a lfs molecule located anywhere within the hexapole will move towards the center. This is illustrated in Figure 9.2, where a  $\text{ND}_3$  molecule has moved from its initial position (marked in light gray) to the center of the hexapole. The molecule may not remain at the center, though, but rather oscillate around it, always trying to return to that low-electric field region. This illustration demonstrates how an electrostatic hexapole can constantly confine lfs molecules in two directions.

That's a pretty good starting point for an electrostatic ring for lfs molecules: simply bend a hexapole into a torus, to guarantee 2-D confinement of the

molecules along the entire ring. However, one must recall that an object set along a curved path experiences a centrifugal force pushing it outwards. We need to take this force into account for the molecules. The centrifugal force is an “effective force”, which is conveniently used to explain the behavior of objects from a frame of reference that is, itself, rotating. The centrifugal force can be ‘felt’ anytime you ride a simply merry-go-round in a child’s playground. The centrifugal force depends on the speed of rotation, the distance from the center, and the mass of the object: the greater the speed of the object, the greater the force; the greater the distance from the center, the greater the force; and the more massive the object, the greater the force. Hence, an adult has a harder time hanging on to the merry-go-round than a child does. To the person on the merry-go-round, the centrifugal force appears real – and it is, in the sense that if you do not hold on, or exert a counter force, you will fly off. The counter-active force that prevents you from flying off, i.e., the friction between your feet and the platform or your applied force to hold on, is known as the centripetal force. The centripetal force is directed towards the center of curvature of the path; in fact the term stems from the Latin for ‘center seeking’.

In our 2-piece\* hexapole ring, shown in Figure 9.3, the electric field provides the centripetal force on a lfs molecule, as shown in the inset (cross-section) of Figure 9.3. Hence, the molecule is located at the radial position where the sum of the electrostatic (centripetal) and centrifugal forces is zero. This position is known as the equilibrium radius,  $r'$  or  $r'_{\text{equi}}$ . If a molecule was moving at 0 m/s, it would be found directly at the center of the hexapole. However, the molecule orbits around the ring with some velocity, so its  $r'$  shifts outwards. If the velocity of the molecule is too high, i.e., if the centrifugal force is greater than the centripetal force, the molecule will not be able to follow the bend, but will instead fly straight (out of the ring) and be lost. The range of velocities for which my ring is suitable is between zero and 90 m/s. A  $\text{ND}_3$  molecule moving at roughly 87 m/s is depicted at its  $r'$  ( $\approx 2$  mm) in the inset of Figure 9.3.

Now that you understand the important details for confining molecules in two directions, let us now turn our attention to keeping a group of molecules confined in a tight packet along the third (in-flight) direction. As a group of molecules fly around the ring, the faster ones will begin to pull ahead of the group, while the slower ones will begin to lag behind the group. However, I want the group of molecules to stay in a tight packet. So as the molecules pass through the gaps, I change the electric fields such as to give a slight acceleration to the slow molecules and a slight deceleration to the fast molecules. This action causes the molecules to bunch together, or to be focused towards the one molecule moving at the perfect (pre-set) velocity. As the molecules continue to revolve, they will also continue to drift apart over the next half-ring – but as I will continue to re-bunch them every time they pass the gap, the molecules

---

\*Why two pieces? Well those gaps are purposely built into the ring to provide a place to confine the molecules along the (third) longitudinal direction, which I will discuss in a moment.

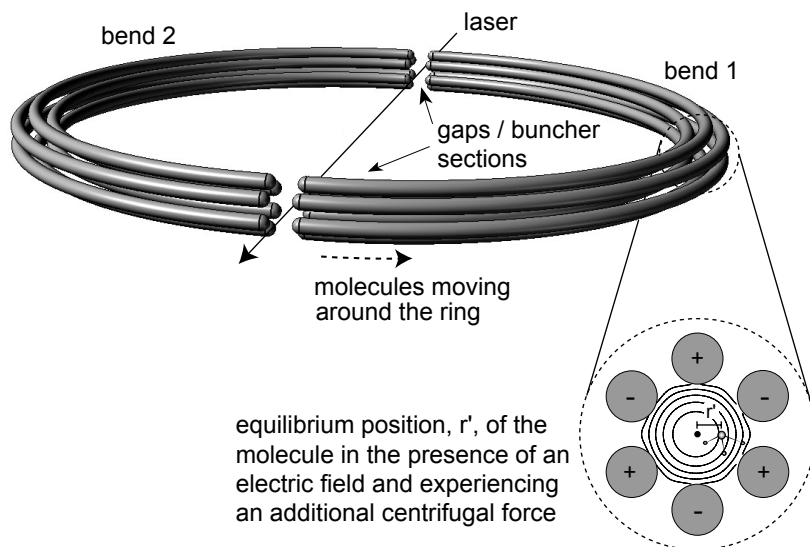


Figure 9.3: A sketch depicting the molecular synchrotron. Two hexapoles are bent into half-rings and are separated by a 2 mm gap. The molecules are bunched, and detected via laser ionization and ion counting (latter not shown), in the gaps. The inset shows a cross-section (cut-through) of the ring. As known from basic physics, any object moving in a circle will experience a centrifugal force (outwards). The electric field provides the centripetal force (inwards) to balance the centrifugal force; the position where these two forces cancel,  $r'$ , is the same position at which the molecules will orbit. The molecule in the inset is moving at about 87 m/s.

cannot spread out much. Thus the molecules are essentially confined in the longitudinal direction. It is the switching of the electric fields in these gap regions that is timed in sync with the (velocity-dependent) position of the molecules that gives us the accreditation to call this device a ‘molecular synchrotron’.

### 9.3 In my thesis

The goal of my doctoral work was to set up and demonstrate a synchrotron for neutral polar molecules. I have merged technologies from both accelerator physics and molecular beam methods to create the appropriate tools for decelerating, injecting, and storing a packet of  $\text{ND}_3$  molecules in a synchrotron (Chapter 2). The molecules are first decelerated using a Stark decelerator, which also utilizes electric fields to manipulate lfs molecules. For most of the experiments, a packet of molecules was decelerated to 87 m/s, and then focused (prepared)

for injection into the synchrotron (Chapter 3). Once the molecules are located inside the synchrotron, the voltages on the hexapole bends are applied in sync with the movement of the revolving molecules, to provide confinement forces in two directions over the course of the bend (Chapter 4), and buncher forces in the gaps (for focusing in the third direction). Molecules are stored for up to 100 round trips, or the equivalent flight distance of over 80 m, in a tight packet with a length of less than 3 mm (Chapter 5). Molecules with different velocities can also be stored in the ring, ranging from 60 to 90 m/s, however one must be careful to apply the appropriate voltages, which are velocity dependent (Chapter 6). I have studied the voltage-velocity relationship in detail, as well as the synchrotron's transversal and longitudinal trapping parameters – as the molecules are essentially confined in a trap that simply revolves along a circle at a certain speed. The research described in this thesis has paved the way for developing a 40-piece molecular synchrotron (Chapter 7), which has been constructed, and is currently being tested, at the Friz-Haber-Institut in Berlin, Germany.





# Acknowledgments

As I was riding the U-bahn on my way to the Fritz-Haber-Institut in March of 2004 for an informal visit, I was expecting to see an impressive lab and maybe meet a few nice people. What I was not expecting to find was a lab that I would come to think of as my home for the next four years. Not only was I fortunate enough to have been given the great opportunity to work on a novel project in an experimental group on the very cutting edge of physics research, but I was also given the chance to work with a team of extraordinary people. I have had a wonderful time working on my PhD, and there are many people that I would like to thank for that experience.

First, I would like to thank my promoter Gerard Meijer for taking me on as a PhD student ‘mit Auflagen’. You provided me with support not only through your famous mantra of “we’re going to get this going”, but also by rolling up your sleeves and joining in. You often came into the lab and helped, whether it be by crawling under the floorboards to stop a water leak or by reminding me to check if the bias voltages were switched on when I was struggling to recover the same signal intensities from the previous day. I really looked forward to hanging up new results on your door, and even more to the ensuing discussions about them the next day; these talks were always motivating and insightful. I have fond memories of us sitting behind your computer typing the introduction to the PCCP paper together – even if I did have to sit on my hands to resist taking over the keyboard to type faster. You always found time for me, even as the group grew in size, and I really appreciate that.

I would next like to thank my co-promoter, Rick Bethlem. Even though you were not always in Berlin, I never felt alone ... and probably neither did you with all my phone calls and emails. Thank you for your patience; you answered all my questions even if you had answered them (n-)times before. I will never forget the night of April 11<sup>th</sup>, 2006 when we were sitting in the lab, watching a TOF scan on the monitor, and were singing and swaying to the tune of ‘We are the Champions’ as we saw the first signal of molecules being successfully bunched in the ring. Thank you for helping to make the ring work, and for this memory. I am also deeply indebted to you for sharing with me your extensive knowledge on physics, phase-space dynamics, programming in Fortran, and Primus lyrics. I also thank you for playing guitar for the live

rendition of the ‘Ring of Molecules’. Unfortunately, due to length restrictions, I am forced to summarize four-years-worth of gratitude into only these few sentences here – but trust me this is only the tip of the iceberg. Rick, your guidance, your support, and your friendship have meant a lot to me over these past years.

Specifically pertaining to this thesis, I would like to thank Gerard and Rick for reading my manuscript – more than once – ‘with a fine-toothed-comb’, and thereby improving the quality of this thesis. Rick: thank you for the Dutch translations. I also would like to thank the members of the manuscript committee, David Parker, Tim Softley, and Bas van de Meerakker, for their careful reading and helpful suggestions.

For the first six months of my PhD, I had the good fortune to work with David Carty. David, you taught me most of what I know about lasers, and together we built up and aligned the decelerator beamline. You helped me find my way around the beamline machine. We measured the first beam signal together, and you shared with me the secret of how to make a good “cuppa”. I wish we could have worked together longer, but at least you visited and joined for the crazy Deutsch-American Volksfest.

I am indebted to André van Roij and Henrik Haak for their technical expertise and their tremendous help in the construction and assembly of the synchrotron. André, not only did you show me how to create a ‘mooi’ two-piece synchrotron, but you returned to FHI to construct an impressive 40-piece ring – and shared the details with me as you progressed. I learned so much from your visits to the Institute, and I enjoyed hearing about Dr. Dre’s adventures at the track, and losing to you in darts. Henrik, du hast mir geholfen als ich allein im Labor stand. Deine innovativen Ideen haben entscheidend geholfen den geteilten Ring zum Laufen zu bekommen. Wir waren ein gutes Team, auch wenn wir leidenschaftliche Gegner beim Kicker waren. Es hat mich sehr gefreut, mit dir zu arbeiten und von dir zu lernen.

Über die Jahre haben mir Manfred Erdmann, Jürgen Maier, Rolf Meilicke und Georg Hammer mit großer technischer Unterstützung beigestanden. Manfred: vielen Dank auch für die Süßigkeiten-Unterstützung. Danke auch an Sandy Gewinner, der sich fürsorglich um mein Laser gekümmert hat und immer wieder die allerhöchste Leistung herauskitzelte. Für das Messprogramm KouDa möchte ich Jochen Küpper und Uwe Hoppe danken.

Ich möchte weiter allen Kollegen im Elektroniklabor herzlich danken. Insbesondere bedanke ich mich bei Georg Heyne und Viktor Platschkowski, die immer ‘schnell mal rüberkamen’ bei großen und kleinen Problemen. Ihr hatten immer die besten Ideen für die verschiedenen Schalter, ohne welche mein Experiment nicht geklappt hätte. Auch ohne das Maus-Klavier wäre ich nicht weitergekommen – danke an Torsten Vetter. Für die Fertigung des Rings bin ich der gesamten Feinwerkstatt sehr dankbar.

I am eternally grateful to the entire Molecular Physics department. The first colleague that I would like to mention is the person that keeps the entire

department running: Inga von Dölln. Inga, danke für dein offenes Ohr, die besten Tipps und Ratschläge für alle meine Probleme. Du hast immer Alles im Griff. Bea Wiczorek und Christa Hermanni, auch Ihr wart immer da - hilfsbereit und freundlich - wenn ich Hilfe brauchte.

Thanks to all my office-mates who put up with my loud laugh and unending chatter. Kirstin: Thank you for having a laugh as big as mine, and for taking me out of the office to go climbing in Mauer Park. Irena: Thanks for all the good gossip and hosting poker night. Amudha: Thanks for the real Indian chai tea. Werner: We make a damn good kicker team.

To Jacqueline and Sophie, it is always my great pleasure to have you by my side, which is why you were the obvious choices for my paranimfen. Jac: The combined strength of our laughs is something I will never forget ... and probably neither will Bas or anyone else who worked within earshot. One moment that stands out is the night of October 21<sup>st</sup>, 2005, as we celebrated my first decelerated signal and your first trapped signal over take-out pizza. Formally, I thank you for our discussions about deceleration, your help trouble-shooting in the lab, teaching me Dutch, and singing along to 'Ring of Molecules'. But as a great friend, I thank you for so much more. Dank je wel. Sophie(chen): I loved sharing an office with you for over four years. It was always helpful to hear your opinion, whether it be about science (how to plot the clearest graph and practicing talks), decoration (Rex Gildo photo), fashion (particularly at the flea market), and/or social events (Zitty reports things two days after you know them). We just click together, which makes our friendship very special.

I also want to thank my lab-neighbors, Melanie and Moritz, who were not only helpful, e.g., by turning off the nozzle at night or by helping me to align the laser through the lab, but were also reliable for discussing results or just having a nice chat and a good laugh. Moritz, I'm really glad I was able to share with you some late-night measuring shifts – complete with bad take-out pizza and sushi – at the end of my PhD.

I would also like to particularly thank Adela for double-checking my English, for finding time to help me with various science questions, for teaching me about polenta, and for fond memories of our Sunday brunches (which includes you too, Mike). Sam: You proved me wrong in judging an Oklahoma boy by his cowboy hat. Thank you for teaching me that, and for the loads of help you gave me with my computer, my bibtex, and for preventing me from throwing my computer out the window. For distracting me from work through squash, beer, and humor, I thank Steven and Frank. Frank, you still owe me a case of beer. Joop: I have fond memories of our conference travels together, meeting up in Amsterdam, and you cheering me up after I (kind of) caught the soccer ball at the tournament in Golm. Katrin: Thanks for representing the women at FHI, and talking with me about life, science, and future careers. Andreas: Thanks for reading my thesis and providing me with feedback that made me re-think some phrases. Good luck with your inherited ring.

I would also like to thank the previous ringmeister, Floris, for his interest

in the project and laying an excellent foundation from which I benefited immensely. And to the successive ringmeister, Peter Z., I wish you all the luck in the future and I hope that I was able to answer some of your questions with this book.

All in all, the Molecular Physics Department at Fritz is a wonderful place, and that is largely due to the people. I want to thank Stolli (also for some memorable conversations), Joost (also for some memorable dance moves), Undine (also for the memorable marathons), Nico (also for that memorable phrase), Bas (also for some memorable gossip), Bum Suk (also for sharing lunch), Dagmar and Philipp and Frauke and Peter K. (also for some fun times), Boris and Phil (also for the Oktoberfest), Marko, André, Ludwig, Benny, Fabian, Simon, Stephan, Torsten, Horst, Knut, Jonathan, Christian, Rissu, Wieland, Wolfgang, Evelyn, Gert, Bretislav, Mikhail, Koos, and everyone else for the beers on the terrace, the Wandertage, the End-of-the-Year parties, the Kaffee und Kuchen, and the whole great atmosphere.

I also want to take this opportunity to acknowledge my former teachers and advisers who have helped inspire me to pursue physics: Dawn Meredith, Olof Echt, Eberhard Möbius, Bill Hersman, James Ryan, Bruce Bernero, Louis Brus, Royal Albridge, and Richard Haglund. Your enthusiasm for physics was contagious, and you have taught me the power of a good teacher.

And last, but certainly not least, I want to thank my close friends and family, who have provided me with unwavering support. To my friends in America: Despite the distance, you have cheered me up and made me smile through countless emails and facebook chats. Hier in Berlin, an meine Jungs und Mädels: Es ist immer ein Späßchen mit euch. Anna: Danke, dass es dich gibt. Danke auch für die schöne Zeit in Brasilien – that was the best way to celebrate the end of my thesis-writing! To the Cappettas, the Jungwirths, the Memmerts, and the Dittmanns, you have all been there for me over the last few years to take me out, to cook me a meal, or just in general to have fun; thanks! To my older and wiser sister, thanks for your steady support, and late-night calls to the lab to check up on me. Also to Paul, thanks for the ‘captivating’ suggestion, and welcome to the family. Mom and Dad, I owe you – literally – everything. Words cannot begin to express my gratitude or my love for you both. Und Bernd, du hast das Leben schön gemacht.

Cyn Heiner  
Berlin, Dec. 2008

# Curriculum Vitae

Cynthia E. Heiner

Born May 26, 1980 in New York, USA

- 1998 High School Diploma (Regents), New Rochelle High School, New Rochelle, NY, USA.
- 1998 - 2002 Physics studies (B.S. – Honors), University of New Hampshire, Durham, NH, USA.
- 2000 NSF Summer Undergraduate Research Fellow, under the supervision of Prof. R. F. Haglund, Jr., Vanderbilt University, Nashville, TN, USA. Topic of research: “Fabricating two-dimensional metal nanocrystal arrays using pulsed-laser deposition and focused ion-beam technologies”.
- 2001 NSF Summer Undergraduate Research Fellow, under the supervision of Prof. L. E. Brus, Columbia University, New York, NY, USA. Topic of research: “Rayleigh scattering and correlated atomic force microscopy of J-aggregates”.
- 2002 - 2004 Physics studies at the Freie Universität Berlin, Germany.
- 2002 - 2004 Research for the diploma thesis under the supervision of Prof. I. V. Hertel at the Max-Born-Institut für Nichtlineare Optik und Kurzzeitspektroskopie, Berlin, Germany. Experiments were conducted at the Berlin Electron Synchrotron Facility (BESSY), Berlin, Germany. Topic of the diploma thesis: “Order and symmetries in sexithiophene within thin films studied by angle-resolved photoemission”.
- 2004 - 2008 PhD student in the group of Prof. dr. G. J. M. Meijer. Experiments conducted at the Fritz-Haber-Institut der Max-Planck-Gesellschaft, Berlin, Germany.

# Publications

*Molecular beams with a tunable velocity*

Cynthia E. Heiner, Hendrick L. Bethlem, and Gerard Meijer  
Physical Chemistry Chemical Physics **8**, 2666 (2006).

*A molecular synchrotron*

Cynthia E. Heiner, David Carty, Gerard Meijer, and Hendrick L. Bethlem  
Nature Physics **3**, 115 (2007).

*Motional resonances in a molecular synchrotron*

Cynthia E. Heiner, Gerard Meijer, and Hendrick L. Bethlem  
Physical Review A: Rapid Communications **78**, 030702(R) (2008).

*A synchrotron for neutral molecules*

Cynthia E. Heiner, Hendrick L. Bethlem, and Gerard Meijer  
in preparation.